

Computational modeling of nanomaterials for biomedical applications

Dissertation
zur Erlangung des Doktorgrades
der Naturwissenschaften

vorgelegt beim Fachbereich Physik
der Johann Wolfgang Goethe-Universität
in Frankfurt am Main

von
Alexey Verkhovtsev
aus Sankt Petersburg, Russland

Frankfurt am Main 2016

(D30)

vom Fachbereich Physik der
Johann Wolfgang Goethe-Universität als Dissertation angenommen.

Dekan: Prof. Dr. Rene Reifarth

Gutachter: Prof. Dr. Andrey V. Solov'yov
Prof. Dr. Stefan Schramm
Prof. Dr. Marcus Bleicher

Datum der Disputation: 12.07.2016

Abstract

Nanomaterials, i.e., materials that are manufactured at a very small spatial scale, can possess unique physical and chemical properties and exhibit novel characteristics as compared to the same material without nanoscale features. The reduction of size down to the nanometer scale leads to the abundance of potential applications in different fields of technology. For instance, tailoring the physicochemical properties of nanomaterials for modification of their interaction with a biological environment has been reflected in a number of biomedical applications.

Strategies to choose the size and the composition of nanoscale systems are often hindered by a limited understanding of interactions that are difficult to study experimentally. However, this goal can be achieved by means of advanced computer simulations. This thesis explores, from a theoretical and a computational viewpoints, stability, electronic and thermo-mechanical properties of nanoscale systems and materials which are related to biomedical applications.

We examine the ability of existing classical interatomic potentials to reproduce stability and thermo-mechanical properties of metal systems, assuming that these potentials have been fitted to describe ground-state properties of the perfect bulk materials. It is found that existing classical interatomic potentials poorly describe highly-excited vibrational states when the system is far from the potential energy minimum. On the other hand, construction of a reliable computational model is essential for further development of nanomaterials for applications. A new interatomic potential that is able to correctly reproduce both the melting temperature and the ground-state properties of different metals, such as gold, platinum, titanium, and magnesium, by means of classical molecular dynamics simulations is proposed in this work. The suggested modification of a many-body potential has a general nature and can be utilized for similar numerical exploration of thermo-mechanical properties of a broad range of molecular and solid state systems experiencing phase transitions.

The applicability of the classical interatomic potentials to the description of nanoscale systems, consisting of several tens-hundreds of atoms, is also explored in this study. This issue is important, for instance, in the case of nanostructured materials, where grains or nanocrystals have a typical size of about a few nanometers. We validate classical

potentials through the comparison with density-functional theory calculations of small atomic clusters made of titanium and nickel. By this analysis, we demonstrate that the classical potentials fitted to describe ground-state properties of a bulk material can describe the energetics of nanoscale systems with a reasonable accuracy.

In this work, we also analyze electronic properties of nanometer-size nanoparticles made of gold, platinum, silver, and gadolinium; nanoparticles composed of these materials are of current interest for radiation therapy applications. We focus on the production of low-energy electrons, having the kinetic energy from a few electronvolts to several tens of electronvolts. It is currently established that the low-energy secondary electrons of such energies play an important role in the nanoscale mechanisms of biological damage resulting from ionizing radiation. We provide a methodology for analyzing the dynamic response of nanoparticles of the experimentally relevant sizes, namely of about several nanometers, exposed to ionizing radiation. Because of a large number of constituent atoms (about $10^3 - 10^4$ atoms) and consequently high computational costs, the electronic properties of such systems can hardly be described by means of *ab initio* methods based on a quantum-mechanical treatment of electrons, and this analysis should rely on model approaches. By comparing the response of smaller systems (of about 1 nm size) calculated within the *ab initio*- and the model framework, we validate this methodology and make predictions for the electron production in larger systems.

We have revealed that a significant increase in the number of the low-energy electrons emitted from nanometer-size noble metal nanoparticles arises from collective electron excitations formed in the systems. It is demonstrated that the dominating mechanisms of electron yield enhancement are related to the formation of plasmons excited in a whole system and of atomic giant resonances formed due to excitation of valence *d* electrons in individual atoms of a nanoparticle. Being embedded in a biological medium, the noble metal nanoparticles thus represent an important source of low-energy electrons, able to produce a significant irreparable damage in biological systems.

A general methodology for studying electronic properties of nanosystems is used to make quantitative predictions for electron production by non-metal nanoparticles. The analysis illustrates that due to a prominent collective response to an external electric field, carbon nanoparticles embedded in a biological medium also enhance the production of low-energy electrons. The number of low-energy electrons emitted from carbon nanoparticles is demonstrated to be several times higher as compared to the case of liquid water.

Zusammenfassung

In den letzten Jahrzehnten haben sich Nanowissenschaft und Nanotechnologie zu einem reichen und vielversprechenden Forschungsfeld, das auf die zukünftige wissenschaftliche und technologische Entfaltung richtet, entwickelt [1, 2]. Dies ist vor allem durch die Entwicklung von anspruchsvollen theoretischen und experimentellen Methoden für das Verständnis, die Charakterisierung und Manipulation nanoskaliger Strukturen und Phänomene möglich geworden [3].

Fundamentale Forschungsobjekte sind Nanomaterialien, die die isolierten einzelnen Nanostrukturen und deren Bauteile umfassen. Im Allgemeinen sind Nanomaterialien chemische Substanzen oder Materialien, die in einem sehr kleinen räumlichen Maßstab hergestellt und verwendet werden. Es ist allgemein anerkannt, dass solche Systeme mindestens in einer Dimension Abmessungen haben müssen, die weniger als etwa 100 Nanometer betragen. Im Jahr 2011 hat die Europäische Kommission die Empfehlung zur Definition von Nanomaterialien veröffentlicht [4]. Gemäß dieser Empfehlung ist ein "Nanomaterial": *a natural, incidental or manufactured material containing particles, in an unbound state or as an aggregate or as an agglomerate and where, for 50% or more of the particles in the number size distribution, one or more external dimensions is in the size range 1 nm – 100 nm.*¹ Atomare und molekulare Cluster (auch als Nanopartikel oder Nanokristalle bezeichnet), die die wesentlichen Bausteine für die Nanotechnologie sind, sind Objekte mit allen drei Außenabmessungen im Nanometerbereich. Die obige Empfehlung schlägt auch vor, dass *"... Fullerenes, graphene flakes and single wall carbon nanotubes with one or more external dimensions below 1 nm should be considered as nanomaterials."*²

Materialien, die in einem sehr kleinen räumlichen Maßstab hergestellt werden, können einzigartige optische, elektrische und magnetische Eigenschaften besitzen und völlig neue Eigenschaften aufweisen im Vergleich zu denselben Materialien ohne nanoskalige Abmessungen. Die Schaffung der neuen Nanomaterialien ist ein wichtiges Thema für

¹ein natürliches, zufälliges oder hergestelltes partikelhaltiges Material, dessen Partikel in einem ungebundenen Zustand oder ein Aggregat oder ein Agglomerat sind, und wobei für mindestens 50% der Partikeln eine oder mehrere Außenabmessungen in der Größenordnung von 1 nm auf 100 nm liegen.

²"... Fullerene, Graphenflocken und einwandige Kohlenstoffnanoröhren mit einer oder mehreren Außenabmessungen unter 1 nm sollte als Nanomaterialien berücksichtigt werden."

die Nanowissenschaften. Die Reduzierung der Größe führt zu einer Reihe von neuen physikalischen und chemischen Eigenschaften und einer Fülle von Anwendungsmöglichkeiten in verschiedenen Technikbereichen. Insbesondere werden Nanomaterialien verwendet oder in der Zukunft zur Verwendung vorgeschlagen in therapeutischen und diagnostischen biomedizinischen Anwendungen [5], weil ihre physikalisch-chemischen Eigenschaften angepasst werden können, um Wechselwirkungen mit der biologischen Umgebung zu modifizieren [6, 7].

Strategien zur Wahl der Größe und Zusammensetzung von nanoskaligen Systemen sind oft behindert durch ein begrenztes Verständnis der Wechselwirkungen, die schwer experimentell untersuchbar sind. Allerdings kann dieses Ziel mit Hilfe modernster Computer-Simulationen erreicht werden. Unter der Annahme, dass die Simulationen unterschiedliche Systemeigenschaften korrekt beschreiben, können sie einen Einblick in nanoskalige Charakteristiken des Systems geben und eine preiswerte Alternative zu experimentellen Untersuchungen werden.

Diese Arbeit widmet sich einer theoretischen und computergestützten Untersuchung der Stabilität, sowie der elektronischen und thermomechanischen Eigenschaften von nanoskaligen Systemen und Materialien, die mit biomedizinischen Anwendungen verbunden sind. Die durchgeführte Studie liegt auf dem Grenzgebiet von verschiedenen Wissenschaftsbereichen, wie der Quantenchemie, der Atom- und Molekülphysik, Clusterphysik und der Physik von Strahlenschäden.

In dieser Arbeit untersuchen wir die Fähigkeit von bestehenden klassischen interatomaren Potenzialen, thermomechanische Eigenschaften und die Stabilität von Metallsystemen zu reproduzieren, unter der Annahme, dass diese Potenziale zur Beschreibung der Grundzustandseigenschaften makroskopischer Materialien entwickelt wurden. Es wird festgestellt, dass bestehende klassische interatomare Potenziale angeregte Schwingungszustände schlecht beschreiben, dann nämlich, wenn das System sich weit von dem Minimum der potenziellen Energie befindet. Jedoch ist die Schaffung von zuverlässigen numerischen Modellen für die weitere Entwicklung von Nanomaterialien und ihrer Anwendungen notwendig. In der Arbeit wird ein neues interatomares Potential vorgeschlagen, das in der Lage ist in klassischen Moleküldynamiksimulationen sowohl die Schmelztemperatur als auch die Grundzustandseigenschaften von verschiedenen Metallen korrekt zu reproduzieren. Das neue Potential stellt eine Modifikation des weitverbreiteten Embedded-Atom-Method-Potentials vor. Die Anwendbarkeit des neuen Potentials auf Metalle mit unterschiedlichen Merkmalen der elektronischen Struktur, wie Gold, Platin, Titan und Magnesium, wird demonstriert. Die vorgeschlagene Modifikation eines Vielteilchen-Potenzials ist allgemeiner Natur und kann für weitere ähnliche numerische Studien der thermomechanischen Eigenschaften von einer Reihe von Molekül- und Festkörpersystemen, die Phasenübergänge durchlaufen, verwendet

werden.

Ein Verfahren zum Benchmarking der klassischen Kraftfelder, das auf den *ab-initio*-Berechnungen von kleinen atomaren Cluster basiert, wird vorgeschlagen. Als Beispiel untersuchen wir die Kraftfelder, die Wechselwirkungen zwischen Nickel- und Titan-Atomen beschreiben. Durch die Erforschung der Stabilität der reinen und Ni-dotierten Titancluster im Rahmen des klassischen und *ab-initio*-Ansatzes wird die Genauigkeit der vorhandenen klassischen Potentiale für die Beschreibung von Systemen auf atomarer Skala, wo Quanteneffekte eine entscheidende Rolle spielen, ausgewertet. Dieses Problem ist wichtig beispielsweise im Fall von nanostrukturierten Materialien, deren Körner oder Nanokristalle eine typische Größe von einigen Nanometern haben. Für solche Systeme ist es wichtig, sowohl ganz präzise makroskopische Eigenschaften des Systems, als auch die Eigenschaften von nanoskaligen Systemen, die aus mehreren Dutzenden bis Hunderten von Atomen bestehen, zu beschreiben. Mit dieser Analyse zeigen wir, dass die klassischen Potentiale, die auf die Grundzustandseigenschaften von makroskopischen Materialien abgestimmt sind, oft auch die Eigenschaften von viel kleineren Systemen wie atomaren Clustern mit einer angemessenen Genauigkeit beschreiben können. Daher kann man einen einzigen Satz dieser Kraftfelder verwenden, um die makroskopische Eigenschaften des Materials sowie einige Punktdefekte und lokale Unregelmäßigkeiten von einer perfekten Kristallstruktur, die im atomistischen Maßstab auftreten, zu beschreiben.

In dieser Arbeit analysieren wir auch die elektronischen Eigenschaften von Nanopartikeln aus Gold, Platin, Silber und Gadolinium. Nanopartikel aus diesen Materialien sind aktuell interessant für Anwendungen in der Strahlentherapie [8–12]. Wir konzentrieren uns auf die Freisetzung von niederenergetischen Elektronen mit einer kinetischen Energie von wenigen Elektronenvolt bis zu einigen Dutzenden Elektronenvolt. Es ist bekannt, dass niederenergetische Sekundärelektronen solcher Energien eine wichtige Rolle spielen bei den nanoskaligen biologischen Schädigungsmechanismen, die durch ionisierende Strahlung entstehen [13–15]. Wir schlagen eine Methode vor für die Analyse der dynamischen Antwort von Nanopartikeln experimentell relevanter Größen, nämlich einige Nanometer, die ionisierender Strahlung ausgesetzt gewesen sind. Aufgrund der großen Anzahl von konstituierenden Atomen ($10^3 - 10^4$ Atome) und dem damit verbundenen hohen Rechenaufwand können die elektronischen Eigenschaften solcher Systeme kaum mittels *ab-initio*-Methoden, die sich auf eine quantenmechanische Betrachtung von Elektronen gründen, beschrieben werden. Deshalb sollte sich diese Analyse auf Modellansätze stützen. Durch den Vergleich der Antwort mit kleineren Systemen (von etwa 1 nm), die *ab initio* und im Rahmen des Modells berechnet wurden, bestätigen wir diese Methodik und machen Vorhersagen für die Freisetzung von Elektronen in größeren Systemen.

Die durchgeführte Analyse hat gezeigt, dass ein substanzieller Anstieg der Anzahl der niederenergetischen Elektronen, die von nanoskaligen Edelmetall-Nanopartikeln emittiert wurden, durch kollektive Elektronenanregungen in den Systemen entsteht. Es wird gezeigt, dass die dominierenden Mechanismen der ansteigenden Elektronenausbeute mit (i) der Bildung von Plasmonen und (ii) den durch Anregung der d -Valenzelektronen in einzelnen Atomen eines Nanopartikels entstandenen Riesenresonanzen, verbunden sind. Plasmonen, das heißt kollektive Anregungen von delokalisierten Valenzelektronen, zeigen sich in den Elektronenemissionspektren der Edelmetall-Nanopartikel im Energiebereich von etwa 1–10 eV. Der dominante Mechanismus der erhöhten Elektronenfreisetzung ist mit dem Oberflächenplasmon verbunden, dessen Beitrag zur Elektronenausbeute deutlich mehr als der des Volumenplasmons ist. Bei höheren Elektronenenergien (von einigen Dutzenden eV) leistet die kollektive Anregung von $5d$ -Elektronen in Gold und Platin und $4d$ -Elektronen in Silber, die auf einzelne Atome lokalisiert wird, den Hauptbeitrag zur Elektronenausbeute.

Diese Analyse hat gezeigt, dass die Anzahl der niederenergetischen Elektronen, die durch den Gold- und Platin-Nanopartikel mit einer bestimmten Größe erzeugt werden, mehr als eine Größenordnung die, die in einem äquivalenten Volumen von Wasser erzeugt werden, übersteigt. Also sind die in einem biologischen Medium eingebetteten Edelmetall-Nanopartikeln eine wichtige Quelle für niederenergetische Elektronen. Die vorgestellten Ergebnisse stützen die Ergebnisse der neulich durchgeführten experimentellen Studien [16, 17], die die Bedeutung von Gold-Nanopartikeln in der erhöhten Freisetzung der niederenergetischen Elektronen entdeckten. Solche Elektronen sind für signifikante irreparable Schäden in biologischen Systemen verantwortlich.

Die Analyse des Beitrags der Plasmonen wurde im Rahmen des Modell-Ansatzes, der auf die Plasmon-Resonanz-Approximation [18–20] basiert, durchgeführt. Zur Begründung von Parametern des Modells wurden Photoabsorptionsspektren von verschiedenen atomaren Gold-Clustern berechnet und mit den Spektren, die mittels zeitabhängiger Dichtefunktionaltheorie ermittelt wurden, verglichen. Die Genauigkeit der Ergebnisse ist durch den Vergleich von *ab-initio*-Spektren mit allgemeingültigen experimentellen Daten für das Gold-Atom und mit den Ergebnissen früherer *ab-initio*-Berechnungen erwiesen. Zusätzliche Belege für die Gültigkeit des Modells wird durch einen umfangreichen Vergleich mit aktuellen experimentellen Daten der Photoionisation und Elektronenstreuung von Kohlenstoff-Fullerenen angeführt.

Eine allgemeine Methode für die Untersuchung der elektronischen Eigenschaften von Nanosystemen wird verwendet, um quantitative Vorhersagen für die Elektronenfreisetzung von nicht-metallischen Nanopartikeln zu machen. Es wird gezeigt, dass auch die in einem biologischen Medium eingebetteten Kohlenstoff-Nanopartikel aufgrund einer bedeutenden kollektiven Antwort auf ein externes elektrisches Feld die Freisetzung von

niederenergetischen Elektronen verstärken. Die Anzahl der emittierten Elektronen mit der Energie von 10 eV ist mehrfach höher als im Vergleich zu flüssigem Wasser.

Die Struktur dieser Arbeit ist folgende.

Kapitel 1 enthält eine kurze Einführung in das Problem der Computermodellierung von Nanomaterialien für biomedizinische Anwendungen. Die Hauptfragestellungen der Dissertation werden aufgezählt.

Kapitel 2 gibt einen Überblick über theoretische Methoden zur Beschreibung der Struktur und Dynamik von Nanosystemen. Das Kapitel beginnt mit einer kurzen Einführung in die Born-Oppenheimer-Näherung, die die Grundlage sowohl der *ab-initio*-Methoden für eine quantenmechanische Behandlung der Elektronen als auch der klassischen interatomaren Potentiale ist. Dann folgt die Beschreibung des Konzepts der klassischen Molekulardynamik und werden mehrere Haupttypen von interatomaren Potentialen aufgezählt. Als nächstes werden die Hartree-Fock-Näherung und Dichtefunktionaltheorie, die es erlauben die elektronische Struktur von Vielelektronensystemen zu erforschen, beschrieben. Dynamik der Elektronendichte kann durch zeitabhängige Dichtefunktionaltheorie beschrieben werden, die am Ende des Kapitels dargestellt wird.

Kapitel 3 widmet sich einer Untersuchung der Stabilität und thermomechanischen Eigenschaften von Nanomaterialien durch den *ab-initio*-Ansatz und die klassische Molekulardynamik. Klassische Kraftfelder zur Beschreibung von reinen und Bimetall-Systeme, die aus Titan und Nickel bestehen, werden durch die Dichtefunktionaltheorie-Berechnungen von kleinen atomaren Clustern validiert. Dann wird eine Vorgehensweise für die Schaffung eines neuen interatomaren Potentials formuliert, das in der Lage ist in klassischen Moleküldynamiksimulationen sowohl die Schmelztemperatur als auch die Grundzustandseigenschaften von verschiedenen Metallen korrekt zu reproduzieren.

Kapitel 4 beschäftigt sich mit der theoretischen und numerischen Untersuchung der Elektronenemission von Metallnanopartikeln aus Gold, Platin, Silber und Gadolinium. Ein neuer Mechanismus der erhöhten Freisetzung von niederenergetischer Elektronen von solchen Nanopartikeln durch den Zerfall der kollektiven Elektronenanregungen wird vorgeschlagen und untersucht. Das Kapitel stellt Elektronenemissionspektren von solcher Nanopartikel, die mittels der Plasmonresonanz-Approximation berechnet wurden, dar. Dieser analytische Ansatz stellt ein Mittel für die Untersuchung der Dynamik von kollektiven Elektronenanregungen vor, die in Vielteilchensystemen wie atomaren Clustern und Nanopartikeln entstehen. Die Verwendbarkeit des Modellsatzes wird durch den Vergleich der modellbasierten Spektren mit denen, die durch eine avancierterer Methode, und zwar zeitabhängige Dichtefunktionaltheorie, erhalten wurden, begründet.

Die Analyse der gesteigerten Elektronenausbeute von Kohlenstoff-Nanopartikeln wird im Kapitel 5 präsentiert. Es wird gezeigt, dass die Elektronenausbeute aus einem

Kohlenstoff-Nanopartikel, der aus Fullerit besteht, welches eine kristalline Form von C_{60} -Fullerenen ist, um ein Vielfaches höher ist als die Elektronenausbeute von flüssigem Wasser. Zusätzliche Bestätigung der Plasmon-Resonanz-Approximation, die benutzt wurde, um diese Vorhersagen zu machen, wurde durch einen umfangreichen Vergleich mit aktuellen experimentellen Daten der Photoionisation und Elektronenstreuung von C_{60} -Fulleren erbracht.

Kapitel 6 präsentiert die Zusammenfassung der Ergebnisse, bringt diese Arbeit in Verbindung mit den neuesten biomedizinischen und strahlenbiologischen Studien und gibt einen Ausblick auf die Richtungen zukünftiger Forschung.

Die Dissertation basiert auf Originalergebnissen [21–29], die in internationalen Fachzeitschriften veröffentlicht wurden und auf internationalen Konferenzen vorgestellt wurden.

Table of Contents

Abstract	i
Zusammenfassung	iii
1 Introduction	3
1.1 Problems addressed in this thesis	5
1.2 Thesis overview	7
2 Theoretical methods for the description of structure and dynamics of nanoscale systems	9
2.1 Born-Oppenheimer approximation	10
2.2 Molecular dynamics approach	15
2.2.1 Classical many-body potentials for metal systems	17
2.3 Quantum-mechanical description of many-electron systems	18
2.3.1 Hartree-Fock approximation	19
2.3.2 Density-functional theory	21
2.4 Time-dependent density-functional theory	24
3 Investigation of stability and thermo-mechanical properties of nano-materials and validation of classical interatomic potentials	29
3.1 Benchmark of classical force fields by ab initio calculations of clusters . .	30
3.2 Reconciling simulated melting and ground-state properties of metals . .	37
4 Low-energy electron production by metal nanoparticles	47
4.1 Collective electron excitations in gold clusters under photon impact . .	48
4.1.1 Plasmon nature of the low-energy peak	58
4.2 Impact ionization of gold nanoparticles irradiated by fast ions	60
4.2.1 Theoretical description of inelastic scattering on atomic clusters	60
4.2.2 Inelastic scattering cross section within the plasmon resonance approximation	63
4.2.3 Electron production via the plasmon excitation mechanism . . .	65

4.2.4	Contribution of individual atomic excitations	72
4.2.5	Different kinematic conditions for charged-particle impact	74
4.3	Comparative analysis of electron production by different metal nanoparticles	76
5	Emission of low-energy electrons from carbon nanoparticles	83
5.1	Plasmon excitations in an isolated C ₆₀ molecule	83
5.2	Electron production by an isolated C ₆₀ molecule	87
5.3	Electron production by a large fullerite nanoparticle	89
6	Conclusion and outlook	93
	Acknowledgements	99
	Appendix A: Plasmon resonance approximation	101
	Appendix B: Basis sets in quantum-chemical calculations	109
	Appendix C: Electron production from individual atomic excitations	115
	Bibliography	117
	Biography (Lebenslauf)	137
	List of publications	139

Chapter 1

Introduction

Over the last few decades, nanoscience and nanotechnology have developed into a rich and promising field of research allowing for extensive future scientific and technological development [1, 2]. This has become possible largely due to the development of sophisticated theoretical and experimental techniques for understanding, characterizing, and manipulating nanoscale structures and phenomena [3].

The fundamental entities of interest are nanomaterials that comprise the isolated individual nanostructures and their assemblies. Generally speaking, nanomaterials are chemical substances or materials that are manufactured and used at a very small spatial scale. It is commonly accepted that such systems must have at least one dimension that is less than approximately 100 nanometers. In 2011, the European Commission adopted the recommendation on the definition of a nanomaterial [4]. According to this recommendation, a “nanomaterial” means: *a natural, incidental or manufactured material containing particles, in an unbound state or as an aggregate or as an agglomerate and where, for 50% or more of the particles in the number size distribution, one or more external dimensions is in the size range 1 nm – 100 nm.* This recommendation also suggests that *“... Fullerenes, graphene flakes and single wall carbon nanotubes with one or more external dimensions below 1 nm should be considered as nanomaterials.”*

Materials engineered to such a small scale can possess unique optical, electrical, and magnetic properties and exhibit novel characteristics as compared to the same material without nanoscale features. Construction of new nanomaterials is an important issue in the developing field of nanoscience. The reduction of size leads to a whole range of new physical and chemical properties and to the abundance of potential applications in different fields of technology. In particular, nanomaterials are utilized or proposed to be utilized in the future in therapeutic and diagnostic biomedical applications [5] because their physicochemical properties can be tailored to modify interactions with the biological environment [6, 7].

Atomic and molecular clusters (also referred to as nanoparticles or nanocrystals),

which are one of the most essential building blocks for nanotechnology, are objects with all three external dimensions at the nanoscale. During the last 30 years, the capability of producing free atomic clusters [30], the discovery of a C_{60} fullerene – a nanoscale hollow allotrope of carbon [31], and the first systematic investigations of metal clusters [32–34] have triggered the emergence of cluster science on a systematic basis [35]. Hence, cluster science has grown into an important interdisciplinary field combining different branches of physics and chemistry, and ranging from fundamental research to nanotechnology applications [36–38].

At present, there is a vivid scientific interest in studying the interaction of nanoparticles with biological media because of the large number of possible applications in nanomedicine [39, 40]. One of the promising ideas is to use metal-based nanoparticles in cancer treatments with ionizing radiation [8, 11, 41–43]. Radiation therapy (or shortly, radiotherapy) is one of the frequently used technologies to treat tumors, which are a major health concern. However, this technique has a limitation which comes from the sensitivity of healthy tissues, surrounding the tumor, to radiation. To make the treatment more efficient, one needs to minimize the dose delivered to the healthy tissue, thus preventing harmful effects of radiation exposure. This problem can be handled by using radiosensitizers which can locally enhance the radiation damage of the tumor cells and thus increase the efficiency of radiotherapy. Thereby, approaches that could enhance radiosensitivity within tumors relative to normal tissues have the potential to become advantageous radiotherapies [44].

Nanostructured materials, where grains or nanocrystals have a typical size of about several nanometers, represent another illustrative example of systems which have been explored for biomedical applications. Of particular interest is the fabrication of devices composed of nanostructured metal materials which are designed for being implanted in living tissues. Nanostructuring of such devices can provide them with superior mechanical properties and enhanced biocompatibility as compared to the properties of the corresponding bulk materials [45]. Materials such as nanostructured titanium and its alloys attract much attention in view of their medical application in surgery, orthopaedic, and dental medicine [46, 47]. A nickel-titanium alloy with almost equal concentration of both types of atoms manifests the so-called superelastic behavior [48], which is quite similar to that of living tissues. Thereby, this compound is an excellent candidate for implant material capable of mimicking the mechanical behavior of bones [49].

Strategies to select nanomaterial components as well as to choose the size and the shape of nanosystems are often hindered by a limited physical understanding of interactions that are difficult to study experimentally. However, this goal can be achieved by means of advanced computer simulations. Provided that the simulations correctly describe different system properties, they may give insights into nanoscale features of the

system and become a low-cost alternative to experimental studies. Thus, construction of reliable computational models for the numerical study of nanomaterials is essential for their further developments for technological applications.

1.1 Problems addressed in this thesis

The aim of this work is to advance the understanding of stability, electronic, and thermo-mechanical properties of nanomaterials which are of current interest for biomedical applications and to analyze the physical processes that occur in such nanoscale systems by means of advanced computer simulations. In order to achieve this goal, the following main problems were addressed:

1. The ability of existing classical interatomic potentials to reproduce the stability and thermo-mechanical properties of metal systems, assuming that these potentials have been fitted to describe ground-state properties of the perfect bulk materials, was examined. It was found that the existing classical interatomic potentials poorly describe highly-excited vibrational states when the system is far from the potential energy minimum. A new interatomic potential that is able to correctly reproduce both the melting temperature and the ground-state properties of different metals by means of classical molecular dynamics simulations was proposed. This study was motivated by the fact that the proper quantitative description of phase transitions in general and the melting process in particular by means of classical molecular dynamics simulations is a major scientific challenge. The new potential represents a modification of the widely used embedded-atom method-type potential. The applicability of the new potential to metals with different characteristics of the electronic structure, such as gold, platinum, titanium, and magnesium, was demonstrated. The results of these studies are presented in Chapter 3 and in Ref. [21].
2. A method for benchmarking classical force fields, which is based on the *ab initio* calculations of small atomic clusters, was proposed. As a case study, the force fields which describe interactions between nickel and titanium atoms were investigated. By studying the stability of pure and Ni-doped titanium clusters within the classical and *ab initio* frameworks, we evaluated the accuracy of the existing classical interatomic potentials for the description of systems on the atomistic scale, where quantum effects play a crucial role. This issue is important, for instance, in the case of nanostructured materials, where grains or nanocrystals have a typical size of about a few nanometers. For such systems, it is important to describe rather accurately both bulk properties of the system and also the properties of

nanoscale systems consisting of several tens-hundreds of atoms. As a result of this analysis, it was demonstrated that the classical interatomic potentials fitted to describe ground-state properties of a bulk material can also describe, with a reasonable accuracy, the properties of much smaller systems that are driven by classical interatomic interactions. Therefore, one can use a single set of the force fields to describe the bulk properties of the material as well as some point defects and local irregularities of a perfect crystalline structure, which occur on the atomistic scale. The results of this analysis are presented in Chapter 3 and in Refs. [22, 23].

3. A theoretical and numerical analysis of electronic properties of nanometer-size metal nanoparticles was performed by means of *ab initio* and model approaches. In particular, we focused on the study of electron production by gold nanoparticles irradiated with photons and fast ions. For that, the photoabsorption spectra of several gold clusters were calculated in a broad photon energy range by means of time-dependent density-functional theory. It was revealed that a significant increase in the number of emitted electrons arises from collective electron excitations in the clusters. The dominating enhancement mechanisms are related to the formation of (i) plasmons excited in a whole system, and (ii) atomic giant resonances due to excitation of *d* electrons in individual atoms. By performing this analysis, we provided a methodology for analyzing the dynamic response of nanoparticles of the experimentally relevant sizes, namely of about several nanometers, exposed to ionizing radiation. Because of a large number of constituent atoms (about $10^3 - 10^4$ atoms) and consequently high computational costs, the electronic properties of such systems can hardly be described by means of *ab initio* methods based on a quantum-mechanical treatment of electrons, and this analysis should rely on model approaches. The results of this analysis are presented in Chapter 4 and in Ref. [24].
4. The yield of low-energy electrons generated by gold nanoparticles of different size due to irradiation by fast charged projectiles was estimated. The results of calculations were compared to those obtained for liquid water representing a biological medium. It was demonstrated that due to a prominent collective response to an external field, gold nanoparticles significantly enhance the yield of secondary electrons as compared to water. Thus, decay of the collective electron excitations in a nanoparticle embedded in a biological medium represents an important mechanism of the low-energy electron production. The results of this analysis are presented in Chapter 4 and in Refs. [24, 25].
5. A theoretical and numerical analysis of electron production by platinum, silver,

and gadolinium nanoparticles irradiated by fast ions was performed; along with gold nanoparticles, the nanoparticles composed of these materials are of current interest for cancer treatments with ionizing radiation. The study revealed that the noble metal nanoparticles irradiated with fast ions significantly enhance the production of low-energy electrons, which play an important role in the biological damage on the nanoscale. A physical explanation for this effect was provided. The results of this analysis are presented in Chapter 4 and in Ref. [25].

6. A general methodology developed for studying electronic properties of nanosystems was used to make quantitative predictions for electron production by non-metal nanoparticles. We made quantitative predictions for electron production by carbon nanoparticles exposed to ionizing radiation. It was demonstrated that due to a prominent collective response to an external electric field, carbon-based fullerite nanoparticles embedded in the medium also enhance the yield of low-energy electrons. The validity of the model approach, which was used to make these predictions, was thoroughly justified by an extensive comparison with recent experimental data on photoionization and electron scattering from a C₆₀ fullerene. The results of these studies are presented in Chapter 5 and in Refs. [26–29].

1.2 Thesis overview

The thesis is structured as follows.

Chapter 2 gives an overview of theoretical methods for the description of structure and dynamics of nanoscale systems. The chapter starts with a brief introduction to the Born-Oppenheimer approximation that is the cornerstone for both *ab initio* methods for a quantum-mechanical treatment of electrons and classical interatomic potentials. Then follows the description of the concept of classical molecular dynamics and several major types of interatomic potentials are outlined. Next, the Hartree-Fock approximation and density-functional theory, which allow the study of electronic structure of many-electron systems, are described. Dynamics of electron density can be described by means of time-dependent density-functional theory, which is also outlined in the end of the chapter.

Chapter 3 is devoted to the investigation of stability and thermo-mechanical properties of nanomaterials by means of *ab initio* and classical molecular dynamics approaches. Classical force fields for the description of monatomic and bimetallic systems composed of titanium and nickel are validated through the density-functional theory calculations of small atomic clusters. Then, a recipe for constructing a new interatomic potential, which is able to correctly reproduce both the melting temperature and the ground-state

properties of metal systems by means of molecular dynamics simulations, is formulated. The applicability of the new force field to different metal systems, such as gold, platinum, titanium, and magnesium, is demonstrated.

Chapter 4 is devoted to the theoretical and numerical investigation of electron emission from metal nanoparticles composed of gold, platinum, silver, and gadolinium. A new mechanism of low-energy electron yield enhancement from such nanoparticles due to the decay of collective electron excitations is proposed and explored. The chapter presents spectra of electron emission from nanometer-size nanoparticles calculated by means of the plasmon resonance approximation [18–20]. This analytical approach represents a tool for investigating the dynamics of collective electron excitations arising in many-particle systems, such as atomic clusters and nanoparticles. Validity of the utilized model approach is justified by comparing model-based spectra with those obtained by means of a more advanced method, namely by time-dependent density-functional theory. The performed analysis reveals that the number of the low-energy electrons generated by small noble metal nanoparticles exceeds by more than an order of magnitude that produced by an equivalent volume of liquid water representing a biological medium.

The similar effects of electron yield enhancement have been observed for carbon nanoparticles; this analysis is presented in Chapter 5. Electron yield from a solid carbon nanoparticle composed of fullerite, a crystalline form of C_{60} fullerene, is demonstrated to be several times higher than that from liquid water. Additional validation of the plasmon resonance approximation, which was used to make these predictions, has been made by an extensive comparison with experimental results on photoionization and electron scattering from C_{60} .

Chapter 6 presents the summary of the results, draws a connection between this work and recent biomedical and radiobiological studies, and gives an outlook for the directions of further investigations.

The thesis is based on the original results, published in international journals [21–29] and presented at international conferences. Papers not included in this thesis are mentioned in the complete list of author’s scientific publications on pp. 139–142.

Chapter 2

Theoretical methods for the description of structure and dynamics of nanoscale systems

Computer simulations based on atomistic models have become nowadays a powerful tool for gaining fundamental knowledge about structural and dynamical properties of materials, and processes involving these systems. The capabilities and areas of application of such simulations continue to grow, being reinforced by the progress in modern computer technology and by the development of new simulation methods and numerical algorithms [50]. This chapter aims at providing a brief overview of theoretical approaches which have been utilized in this study for exploring the structure and dynamics of many-particle systems.

The two main approaches are currently used to describe interatomic interactions, namely (i) *ab initio* methods based on a quantum-mechanical treatment of electrons and (ii) classical interatomic potentials. Most *ab initio* electronic structure calculations, which are based on the Hartree-Fock method [51] or density-functional theory [52, 53], assume the electronic configuration to be in an instantaneous ground state for each nuclear configuration. Besides, *ab initio* methods can be utilized for investigating electron dynamics induced, for instance, by the interaction of radiation with matter. In this case, one can employ time-dependent density-functional theory [54]. It is also possible to investigate the influence of excited electronic states on the dynamics of nuclei. This problem requires an exploration of a potential energy surface for the nuclear motion that defines the total energy of electrons as a function of nuclear coordinates. Since the mass of a nucleus far exceeds that of an electron, the Born-Oppenheimer approximation [55] implies the separation of the motion of slow (nuclei) and fast (electrons) degrees of freedom of a molecular system. In consideration of the large masses and slow motion

of the nuclei, their motion is often treated using classical mechanics. In this case, the potential energy surface, which is mapped out for different nuclear configurations, is used in classical computations for the motion of the nuclei.

If the potential energy surface is computed on-the-fly to drive Newtonian dynamics for the nuclei, this approach is usually referred to as *ab initio* molecular dynamics (MD) [56,57]. Based on solution of the Schrödinger equation for the description of interactions within the system, this method represents one of the most accurate and advanced MD techniques. However, this approach demands significant computational resources and is applied typically for the description of dynamics of small systems (of about $10^1 - 10^2$ atoms) at the picosecond (10^{-12} s) time scale. Dynamic processes involving large ensembles of particles, such as diffusion or phase transitions, can hardly be accessed by means of this approach [50].

An alternative to the *ab initio* methods are the classical MD simulations. Within this framework, the description of the time evolution of a system is achieved by integrating classical equations of motion using the defined interactions between the constituent atoms. Given the initial coordinates and velocities of the atoms in a system, the subsequent motion of individual atoms is described either by deterministic Newtonian dynamics or by Langevin-type stochastic dynamics. Classical MD allows for an ultimate description of dynamics of million-atom systems [58,59] at substantially larger (up to $10 - 100$ nanoseconds, i.e. $10^{-8} - 10^{-7}$ s) time scales [60]. Thus, classical MD simulations represent a powerful tool which have an eminent research potential. They can provide insights into nanoscale structural features and thermo-mechanical properties of a system by means of advanced computer simulations [61]. The interatomic interactions are parameterized in this approach using various empirical potentials of the force fields, whose parameters are usually derived from *ab initio* studies of systems containing a much smaller number of atoms or fitted to experimental data. Provided that interatomic potentials correctly describe different system properties, classical MD simulations may thus represent a low-cost alternative to experimental studies, reaching the system sizes and time scales that are inaccessible by other methods [58,62–64].

2.1 Born-Oppenheimer approximation

Let us consider an arbitrary molecular system comprising N atoms. In the non-relativistic case, the Hamiltonian \hat{H} of the system includes the operators for kinetic energy and electrostatic interaction, while weaker interactions, such as spin-orbit and

spin-spin coupling, are neglected. Hence, the Hamiltonian is given by

$$\begin{aligned}
 \hat{H} &= \sum_{\alpha=1}^N \left(-\frac{\hbar^2}{2M_{\alpha}} \nabla_{\alpha}^2 \right) + \sum_{i=1}^{N_e} \left(-\frac{\hbar^2}{2m_e} \nabla_i^2 \right) \\
 &+ \sum_{\alpha < \beta} \frac{Z_{\alpha} Z_{\beta} e^2}{|\mathbf{R}_{\alpha} - \mathbf{R}_{\beta}|} + \sum_{i < j} \frac{e^2}{|\mathbf{r}_i - \mathbf{r}_j|} - \sum_{\alpha=1}^N \sum_{i=1}^{N_e} \frac{Z_{\alpha} e^2}{|\mathbf{r}_i - \mathbf{R}_{\alpha}|} \\
 &\equiv \hat{T}_N + \hat{T}_e + \hat{V}_{NN}(\mathbf{R}) + \hat{V}_{ee}(\mathbf{r}) + \hat{V}_{eN}(\mathbf{r}, \mathbf{R}) ,
 \end{aligned} \tag{2.1}$$

where $\{\mathbf{R}\}$ is the set of nuclear coordinates, $\{\mathbf{r}\}$ is the set of electronic coordinates, m_e and e are the mass and the charge of an electron, and M_{α} and $Z_{\alpha}e$ denote those of the α^{th} nucleus. Here \hat{T}_N and \hat{T}_e represent the nuclear and electron kinetic energy operators, and $\hat{V}_{NN}(\mathbf{R})$, $\hat{V}_{ee}(\mathbf{r})$, and $\hat{V}_{eN}(\mathbf{r}, \mathbf{R})$ describe the nucleus-nucleus, electron-electron, and electron-nucleus interaction, respectively. Eigenfunctions and eigenvalues of this Hamiltonian are determined from the solution of the Schrödinger equation:

$$\hat{H}(\mathbf{r}, \mathbf{R}) \Psi(\mathbf{r}, \mathbf{R}) = E \Psi(\mathbf{r}, \mathbf{R}) , \tag{2.2}$$

where $\Psi(\mathbf{r}, \mathbf{R})$ is the ground-state wave function of the system and E is its total energy.

The $\hat{V}_{eN}(\mathbf{r}, \mathbf{R})$ term prevents us from separating the Hamiltonian (2.1) into nuclear and electronic parts, which would allow one to write the total wave function as a product of nuclear and electronic terms, $\Psi(\mathbf{r}, \mathbf{R}) = \Psi_e(\mathbf{r}) \Psi_N(\mathbf{R})$. Within the Born-Oppenheimer approximation [55], it is assumed that this separation is nevertheless approximately correct. The physical basis for the Born-Oppenheimer approximation is the fact that the mass of an atomic nucleus in a molecular system is much larger than the mass of an electron, $M_{\alpha} \gg m_e$. Because of the significant difference in masses, the electrons move much faster than the nuclei. Thus, they "see" an instantaneous position of the nuclei, while the latter feel only an average potential of electron cloud, that is, the electrostatic field caused by spatially distributed negative charge [65]. In a dynamical sense, the electrons can thus be regarded as particles that follow the nuclear motion adiabatically, meaning that they are "dragged" along with the nuclei without requiring a finite relaxation time. One should note that there could be non-adiabatic effects that do not allow the electrons to follow in this "instantaneous" manner; however, in many systems, the adiabatic separation between electrons and nuclei is a good approximation [66].

Since the nuclei are much more massive than the electrons, the distribution of the latter in the molecular system can be studied when the nuclei are at rest in a space-fixed frame. In mathematical terms, the Born-Oppenheimer approximation implies that the

total wave function $\Psi(\mathbf{r}, \mathbf{R})$ of the system can be written as follows:

$$\Psi(\mathbf{r}, \mathbf{R}) = \Psi_e(\mathbf{r}; \mathbf{R}) \Psi_N(\mathbf{R}) , \quad (2.3)$$

where $\Psi_e(\mathbf{r}; \mathbf{R})$ is the electronic wave function calculated in the field of fixed-in-space nuclei ($\{\mathbf{R}\} = \text{const}$), and $\Psi_N(\mathbf{R})$ is the nuclear wave function. The Born-Oppenheimer approximation allows one to reduce the solution of the general equation (2.2) to the solution of two separate Schrödinger equations, for an electronic and a nuclear subsystems, respectively.

Consider again the original Hamiltonian (2.1). Using a wave function of the form (2.3) in the Schrödinger equation (2.2), one obtains

$$\left[\hat{T}_N(\mathbf{R}) + \hat{T}_e(\mathbf{r}) + \hat{V}_{NN}(\mathbf{R}) + \hat{V}_{ee}(\mathbf{r}) + \hat{V}_{eN}(\mathbf{r}, \mathbf{R}) \right] \Psi_e(\mathbf{r}; \mathbf{R}) \Psi_N(\mathbf{R}) = E \Psi_e(\mathbf{r}; \mathbf{R}) \Psi_N(\mathbf{R}) . \quad (2.4)$$

Since \hat{T}_e does not depend on \mathbf{R} , one can perform the following transformation:

$$\hat{T}_e \Psi_e(\mathbf{r}; \mathbf{R}) \Psi_N(\mathbf{R}) = \Psi_N(\mathbf{R}) \hat{T}_e \Psi_e(\mathbf{r}; \mathbf{R}) . \quad (2.5)$$

The $\hat{T}_N \Psi_e(\mathbf{r}; \mathbf{R}) \Psi_N(\mathbf{R})$ term can be expressed as:

$$\begin{aligned} \hat{T}_N \Psi_e(\mathbf{r}; \mathbf{R}) \Psi_N(\mathbf{R}) &= -\frac{\hbar^2}{2} \sum_{\alpha=1}^N \frac{1}{M_\alpha} \nabla_\alpha^2 \Psi_e(\mathbf{r}; \mathbf{R}) \Psi_N(\mathbf{R}) \\ &= -\frac{\hbar^2}{2} \sum_{\alpha=1}^N \frac{1}{M_\alpha} \left[\Psi_e(\mathbf{r}; \mathbf{R}) \nabla_\alpha^2 \Psi_N(\mathbf{R}) \right. \\ &\quad \left. + 2 \nabla_\alpha \Psi_e(\mathbf{r}; \mathbf{R}) \nabla_\alpha \Psi_N(\mathbf{R}) + \Psi_N(\mathbf{R}) \nabla_\alpha^2 \Psi_e(\mathbf{r}; \mathbf{R}) \right] . \quad (2.6) \end{aligned}$$

Another consequence of the large mass difference between electrons and nuclei is that the nuclear components of the total wave function are spatially more localized than the electronic components of the wave function. Thus, the nuclear wave function varies more steeply than the electronic wave function, which means that $\nabla_\alpha \Psi_N(\mathbf{R}) \gg \nabla_\alpha \Psi_e(\mathbf{r}; \mathbf{R})$. Assuming this, one may neglect the latter two terms on the r.h.s. of Eq. (2.6) and approximate it as

$$\hat{T}_N \Psi_e(\mathbf{r}; \mathbf{R}) \Psi_N(\mathbf{R}) \approx \sum_{\alpha=1}^N \frac{-\hbar^2}{2M_\alpha} \Psi_e(\mathbf{r}; \mathbf{R}) \nabla_\alpha^2 \Psi_N(\mathbf{R}) = \Psi_e(\mathbf{r}; \mathbf{R}) \hat{T}_N \Psi_N(\mathbf{R}) . \quad (2.7)$$

Then, the Schrödinger equation (2.4) transforms into the following one:

$$\begin{aligned}
 & \Psi_e(\mathbf{r}; \mathbf{R}) \hat{T}_N \Psi_N(\mathbf{R}) + \Psi_e(\mathbf{r}; \mathbf{R}) \hat{V}_{NN}(\mathbf{R}) \Psi_N(\mathbf{R}) \\
 & + \Psi_N(\mathbf{R}) \hat{T}_e \Psi_e(\mathbf{r}; \mathbf{R}) + \Psi_N(\mathbf{R}) \hat{V}_{ee}(\mathbf{r}) \Psi_e(\mathbf{r}; \mathbf{R}) + \Psi_N(\mathbf{R}) \hat{V}_{eN}(\mathbf{r}, \mathbf{R}) \Psi_e(\mathbf{r}; \mathbf{R}) \\
 & = E \Psi_e(\mathbf{r}; \mathbf{R}) \Psi_N(\mathbf{R}) .
 \end{aligned} \tag{2.8}$$

This yields

$$\begin{aligned}
 & \Psi_N(\mathbf{R}) \left[\hat{T}_e + \hat{V}_{ee}(\mathbf{r}) + \hat{V}_{eN}(\mathbf{r}, \mathbf{R}) \right] \Psi_e(\mathbf{r}; \mathbf{R}) \\
 & = E \Psi_e(\mathbf{r}; \mathbf{R}) \Psi_N(\mathbf{R}) - \Psi_e(\mathbf{r}; \mathbf{R}) \left[\hat{T}_N + \hat{V}_{NN}(\mathbf{R}) \right] \Psi_N(\mathbf{R}) ,
 \end{aligned} \tag{2.9}$$

or

$$\frac{\left[\hat{T}_e + \hat{V}_{ee}(\mathbf{r}) + \hat{V}_{eN}(\mathbf{r}, \mathbf{R}) \right] \Psi_e(\mathbf{r}; \mathbf{R})}{\Psi_e(\mathbf{r}; \mathbf{R})} = E - \frac{\left[\hat{T}_N + \hat{V}_{NN}(\mathbf{R}) \right] \Psi_N(\mathbf{R})}{\Psi_N(\mathbf{R})} . \tag{2.10}$$

From this expression, it follows that the left-hand side can be represented as a function of \mathbf{R} only. Let this function be denoted as $E_e(\mathbf{R})$. Then,

$$\left[\hat{T}_e + \hat{V}_{ee}(\mathbf{r}) + \hat{V}_{eN}(\mathbf{r}, \mathbf{R}) \right] \Psi_e(\mathbf{r}; \mathbf{R}) \equiv \hat{H}_e \Psi_e(\mathbf{r}; \mathbf{R}) = E_e(\mathbf{R}) \Psi_e(\mathbf{r}; \mathbf{R}) . \tag{2.11}$$

In this equation, the terms in square brackets describe the electronic Hamiltonian \hat{H}_e of the molecular system for a fixed nuclear configuration. The electronic wave function $\Psi_e(\mathbf{r}; \mathbf{R})$ depends explicitly on the coordinates \mathbf{r} of the electrons and parametrically on the position vectors \mathbf{R} of all nuclei. The function $E_e(\mathbf{R})$ is the energy of the electronic subsystem due to the motion of N_e electrons in the field of N nuclei.

For each solution of Eq. (2.11), there will be a corresponding Schrödinger equation for a nuclear subsystem:

$$\left[\hat{T}_N + \hat{V}_{NN}(\mathbf{R}) + E_e(\mathbf{R}) \right] \Psi_N(\mathbf{R}) \equiv \hat{H}_N \Psi_N(\mathbf{R}) = E \Psi_N(\mathbf{R}) , \tag{2.12}$$

where \hat{H}_N is the nuclear Hamiltonian.

To summarize, based on the large difference in the relative masses of the electrons and nuclei, the Born-Oppenheimer approximation allows one to approximately separate the total molecular wave function as a product of nuclear and electronic terms. The electronic wave function $\Psi_e(\mathbf{r}; \mathbf{R})$ is solved for a given set of nuclear coordinates,

$$\begin{aligned}
 \hat{H}_e \Psi_e(\mathbf{r}; \mathbf{R}) & = \left[-\frac{\hbar^2}{2m_e} \sum_i \nabla_i^2 - \sum_\alpha \sum_i \frac{Z_\alpha e^2}{|\mathbf{r}_i - \mathbf{R}_\alpha|} + \sum_{i < j} \frac{e^2}{|\mathbf{r}_i - \mathbf{r}_j|} \right] \Psi_e(\mathbf{r}; \mathbf{R}) \\
 & = E_e(\mathbf{R}) \Psi_e(\mathbf{r}; \mathbf{R})
 \end{aligned} \tag{2.13}$$

and the electronic energy obtained contributes a potential term to the motion of the nuclei, described by the nuclear wave function $\Psi_{\mathbf{N}}(\mathbf{R})$:

$$\hat{H}_{\mathbf{N}}\Psi_{\mathbf{N}}(\mathbf{R}) = \left[-\sum_{\alpha} \frac{\hbar^2}{2M_{\alpha}} \nabla_{\alpha}^2 + E_e(\mathbf{R}) + \sum_{\alpha < \beta} \frac{Z_{\alpha} Z_{\beta} e^2}{|\mathbf{R}_{\alpha} - \mathbf{R}_{\beta}|} \right] \Psi_{\mathbf{N}}(\mathbf{R}) = E \Psi_{\mathbf{N}}(\mathbf{R}) . \quad (2.14)$$

Each electronic eigenvalue $E_e(\mathbf{R})$ gives rise to an electronic surface. The full internuclear potential for each electronic surface is given by $E_e(\mathbf{R}) + \hat{V}_{\mathbf{N}\mathbf{N}}(\mathbf{R})$. On every single surface, the nuclear eigenvalue problem can be solved, which yields a set of levels corresponding to vibrational and rotational motion of the nuclei. Varying the positions of the nuclei in small steps and repeatedly solving the electronic Schrödinger equation, one obtains the electronic energy calculated for different \mathbf{R} . Together with the energy of the mutual repulsion of the nuclei, this electronic energy determines a potential energy surface (PES) along which the nuclei move [66].

In principle, different potential energy surfaces can become coupled by so called non-adiabatic effects, contained in the terms that have been neglected in the above derivation. An important assumption of the Born-Oppenheimer approximation is that there are no excitations of the electrons among the various surfaces. Such excitations constitute non-adiabatic effects which are, therefore, neglected. As an example of a condition in which this approximation is valid, consider a system at temperature T . If the electrons are in their ground state $E_{e,0}(\mathbf{R})$, then, if $E_{e,1}(\mathbf{R})$ denotes the first excited state, there will be no excitations to this state if

$$|E_{e,1}(\mathbf{R}) - E_{e,0}(\mathbf{R})| \gg kT \quad (2.15)$$

for all nuclear configurations. If the system visits such nuclear configurations where the surfaces approach each other with an energy spacing close to kT , then the Born-Oppenheimer approximation breaks down [67]. In many cases, non-adiabatic effects can be neglected, and one may consider motion only on the ground electronic surface. Such motion is described by a time-dependent Schrödinger equation for the time-dependent nuclear wave function $\tilde{\Psi}_{\mathbf{N}}(\mathbf{R}, t)$:

$$\left[\hat{T}_{\mathbf{N}} + \hat{V}_{\mathbf{N}\mathbf{N}}(\mathbf{R}) + E_{e,0}(\mathbf{R}) \right] \tilde{\Psi}_{\mathbf{N}}(\mathbf{R}, t) = i\hbar \frac{\partial}{\partial t} \tilde{\Psi}_{\mathbf{N}}(\mathbf{R}, t) , \quad (2.16)$$

where $E_{e,0}(\mathbf{R})$ is defined from

$$\left[\hat{T}_e + \hat{V}_{ee}(\mathbf{r}) + \hat{V}_{e\mathbf{N}}(\mathbf{r}, \mathbf{R}) \right] \Psi_{e,0}(\mathbf{r}; \mathbf{R}) = E_{e,0}(\mathbf{R}) \Psi_{e,0}(\mathbf{r}; \mathbf{R}) . \quad (2.17)$$

2.2 Molecular dynamics approach

The Born-Oppenheimer approximation not only laid down a practical way of solving the Schrödinger equation for molecular systems, but also gave birth to the concepts constituting the significant share of the modern physical and chemical terminology. One of such concepts is the molecular dynamics technique. Being developed in the 1950s [68, 69], this method has gained popularity in chemical physics, materials science and later also in biophysics and atomic cluster physics.

Molecular dynamics (MD) is a computer simulation technique where the time evolution of a molecular system (that is a set of interacting nuclei and a set of electrons) is followed by integrating their equations of motion. As follows from the Born-Oppenheimer approximation, the slow motion of massive nuclei can be separated from the fast motion of electrons. If nuclear quantum effects can be neglected, the dynamics of nuclei can be treated using classical mechanics. The derivative of the electronic energy $E_e(\mathbf{R})$ with respect to the nuclear degrees of freedom, $\partial E_e(\mathbf{R})/\partial \mathbf{R}$, represents the classical definition of the force acting on the nuclei. Thus, the dynamics of the nuclei can be described by means of Newton's classical equations of motion:

$$M \frac{d^2 \mathbf{R}}{dt^2} = \mathbf{F} = -\nabla_{\mathbf{R}} E_e(\mathbf{R}) . \quad (2.18)$$

There are two main approaches, namely *ab initio* MD (AIMD) and classical MD, that are widely used to describe interatomic interactions in many-particle systems. Within the AIMD approach [56, 57], the forces acting on the nuclei are computed on-the-fly by accurate electronic structure calculations. This approach, which unifies Newton's and Schrödinger's equations, allows for complex simulations without relying on any adjustable parameter and depending only on $\{\mathbf{R}\}$. However, the high accuracy and predictive power of AIMD simulations come at significant computational cost [70]. Thus, this approach is very computationally demanding and currently applied only for the description of dynamics of small systems (typically of less than a few hundreds atoms) at the picosecond time scale.

An alternative to the *ab initio* methods are the classical MD simulations. Within this framework, the description of the time evolution of a system is achieved by integrating classical Newtonian or Langevin equations of motion using the defined interactions between the constituent atoms. The forces \mathbf{F} acting on all particles in the system are determined by a potential function U (also widely referred to as an interatomic potential or a force field) by means of which the particles interact. The potential functions are constructed as a sum over interactions between the particles in the system. The simplest potential function is a pairwise (two-body) potential in which the total potential energy

of the system, U_{tot} , is calculated from the sum of energy contributions between pairs of atoms. Thus, the total energy of the system consisting of N particles interacting via a pairwise potential is calculated as

$$U_{\text{tot}} = \sum_{i=1}^N \sum_{j<i} U(r_{ij}) , \quad (2.19)$$

where $U(r_{ij})$ is the interaction energy between atoms i and j , and $r_{ij} = |\mathbf{r}_i - \mathbf{r}_j|$ is the distance between these atoms. The force acting on the atom i is equal to the negative gradient of the potential taken with respect to the atomic coordinates:

$$\mathbf{F}_i = -\frac{\partial}{\partial \mathbf{r}_i} U_{\text{tot}} = -\frac{\partial}{\partial \mathbf{r}_i} \sum_{\substack{j=1 \\ j \neq i}}^N U(r_{ij}) . \quad (2.20)$$

In many-body potentials, the potential energy includes the effects of three and more particles interacting with one another. In this case, the total energy of a system is

$$U_{\text{tot}} = \sum_{i=1}^N U_i(\{\mathbf{r}_i\}) , \quad (2.21)$$

where $U_i(\{\mathbf{r}_i\})$ describes the interaction of atom i with all other particles in the system.

One should briefly mention another type of the potential function, which is widely used to model biomacromolecules like DNA, proteins, or polypeptides [71, 72]. The basic functional form of this force field is quite different from pairwise and many-body potentials. It includes bonded terms for interactions of atoms, that are linked by covalent bonds, and non-bonded terms that describe the action of the long-range electrostatic and van der Waals forces. A widely used force field, called CHARMM [71], employs harmonic approximation for describing the interatomic interactions, thereby limiting its applicability to small deformations of the molecular system. Thus, this class of potentials is capable of reproducing structural and conformational changes in the system but is usually not suited for modeling chemical reactions. In order to study processes where rupture of chemical bonds plays an essential role, e.g., in irradiation- or collision-induced damage of biomolecular systems, it is essential to go beyond the harmonic approximation, thus describing the physics of molecular dissociation more accurately [73].

2.2.1 Classical many-body potentials for metal systems

Since the main goal of this work is related to the modeling of metal-based nanostructures and nanomaterials, a special attention should be paid to an overview of many-body potentials which are commonly used to describe metal systems in classical molecular dynamics.

Metal systems are characterized by metallic bonding which describes the electrostatic attractive force occurring between conduction electrons and positively charged ions. Metallic radius, that is, one-half of the distance between the two adjacent ions in the lattice, depends on the atom's type and its environment, i.e. on the coordination number. Hence, a proper description of metal systems and their properties requires the consideration of many-body effects. Pairwise potentials are not able to describe metallic bonding; thus, an approach for incorporating many-body effects in the classical interatomic potentials was proposed [74–76].

The main idea of this approach is to add a term, which is a function of the local electronic density of a given atom, to the pairwise term. Hence, the general structure of many-body potentials contains an attractive density-dependent many-body term and a repulsive part for small distances that results from the repulsion between neighboring ions. This method has led to the development of several alternative potentials that mimic the many-body effects.

A well-established potential format for metallic systems is given by the so-called embedded-atom method (EAM) [74, 75] and the Finnis-Sinclair (FS) method [76]. Although initially derived from different physical approaches, the two potential forms are quite similar [50]. In the EAM approach, the total energy of a metal system is expressed via (i) the energy of the short-range electrostatic interaction between atoms i and j separated by r_{ij} , and (ii) the energy F_i , obtained by embedding an atom i into the local electron density ρ_i created by the remaining atoms of the system:

$$U_{\text{tot}}^{\text{EAM}} = \sum_{i=1}^N (U_i^{\text{rep}} + U_i^{\text{attr}}) = \sum_{i=1}^N \left[\frac{1}{2} \sum_{j \neq i} V(r_{ij}) + F_i(\rho_i) \right]. \quad (2.22)$$

The second term in the above expression represents the many-body interactions responsible for bonding in metals. The form of the embedding function is arbitrary in EAM but is postulated to be the negative of the square root of ρ_i in the FS method [50]:

$$U_{\text{tot}}^{\text{FS}} = \sum_{i=1}^N (U_i^{\text{rep}} + U_i^{\text{attr}}) = \frac{1}{2} \sum_{i=1}^N \sum_{j \neq i} V(r_{ij}) - c \sum_i \sqrt{\rho_i}. \quad (2.23)$$

The square root form of the many-body term is chosen in the FS approach to mimic the

results of tight-binding theory, in which the radicand is interpreted as a sum of squares of overlap integrals [76].

A commonly used empirical form of the many-body term, proposed by Gupta [77], reads

$$U_i^{\text{attr}} = - \sqrt{\sum_{j \neq i} \xi^2 \exp \left[-2q \left(\frac{r_{ij}}{d} - 1 \right) \right]}, \quad (2.24)$$

where r_{ij} denotes the interatomic distance. The parameter ξ is an effective overlap integral, d is the nearest-neighbor distance, and the parameter q controls the decay of the exponential function. A similar exponential form is also used for the repulsive term,

$$U_i^{\text{rep}} = \sum_{j \neq i} A \exp \left[-p \left(\frac{r_{ij}}{d} - 1 \right) \right], \quad (2.25)$$

which is commonly known as Born-Mayer ion-ion repulsion [78]. Here the parameter p controls the decay of the function and is related to bulk elastic constants [79], and A sets the energy scale.

2.3 Quantum-mechanical description of many-electron systems

As described above, the Born-Oppenheimer approximation postulates the separation of the total molecular wave function (2.2) of a many-atom system into the electronic and the nuclear parts. When focusing on the electronic subsystem, the problem is reduced to the calculation of a many-electron wave function $\Psi_e(\mathbf{r})$. However, it is not possible to find an exact solution to equation (2.11) for a many-electron system. Thus, one needs to search for approximate methods of solution of a many-electron problem.

This can be done within the framework of the single-particle approximation. It is assumed in this method that each electron moves independently in a so-called self-consistent field, that is the mean field created by the remaining electrons and nuclei. Then, the many-electron Hamiltonian of the system is split into the the Hamiltonian of independent particles and the so-called residual interaction:

$$\hat{H}_e = \hat{H}_0 + \hat{V}_{\text{res}} = \sum_{i=1}^{N_e} \hat{h}_0(\mathbf{r}_i) + \hat{V}_{\text{res}}, \quad (2.26)$$

where

$$\hat{h}_0(\mathbf{r}) = -\frac{\hbar^2}{2m_e} \nabla^2 - \sum_{\alpha=1}^N \frac{Z_\alpha e^2}{|\mathbf{r} - \mathbf{R}_\alpha|} + U(\mathbf{r}) \quad (2.27)$$

and $U(\mathbf{r})$ represents a part of the self-consistent potential created by all electrons in the

system. The electron-electron interaction cannot be fully accounted for by the choice of the self-consistent field. The remaining part, which does not contribute to the field, represents the residual interaction. It defines to what extent the electronic motion in the system differs from the independent motion in the self-consistent field, or, in other words, it accounts for the correlation between electrons. An exact account for the residual interaction is not possible because it would be equivalent to the solution of a many-body problem. However, electron correlation can be taken into account in the single-electron approximation by introducing an additional, the so-called correlation potential.

Among the single-particle approximations, the most commonly utilized approaches are the Hartree-Fock method and density-functional theory (DFT). Within these methods, a many-electron system is described by solving a system of differential or integro-differential equations. The basic principles of these methods are briefly described below.

2.3.1 Hartree-Fock approximation

Within the Hartree-Fock approximation, instead of solving the Schrödinger equation (2.11), one considers the following one:

$$\hat{H}^{\text{HF}} \Psi_e(\mathbf{r}_1, \dots, \mathbf{r}_{N_e}) = E^{\text{HF}} \Psi_e(\mathbf{r}_1, \dots, \mathbf{r}_{N_e}), \quad (2.28)$$

where

$$\hat{H}^{\text{HF}} = \sum_{i=1}^{N_e} \left[-\frac{\hbar^2}{2m_e} \nabla_i^2 - \sum_{\alpha=1}^N \frac{Z_\alpha e^2}{|\mathbf{r}_i - \mathbf{R}_\alpha|} + \hat{U}_{\text{HF}}(\mathbf{r}_i) \right] \quad (2.29)$$

and $U_{\text{HF}}(\mathbf{r}_i)$ is the so-called self-consistent Hartree-Fock potential. The corresponding operator is defined by the wave functions of all electrons in the system.

Strictly speaking, the Hartree-Fock operator \hat{U}_{HF} and the total wave function Ψ_e depend not only on the coordinate of electrons but also on their spin state, which has been neglected so far. Thus, these functions should rather be defined as $\hat{U}_{\text{HF}}(x_i)$ and $\Psi_e(x_1, \dots, x_{N_e})$ where the variable $x_i = (\mathbf{r}_i, \sigma_i)$ defines the coordinate \mathbf{r}_i of the i^{th} electron and its spin projection σ_i .

The solution of equation (2.28) defines the ground state of a many-electron system. The ground-state electronic wave function is approximated by the Slater determinant constructed of single-electron wave functions $\phi_i(x)$:

$$\Psi_e(x_1, \dots, x_{N_e}) = \frac{1}{\sqrt{N_e!}} \begin{vmatrix} \phi_1(x_1) & \phi_2(x_1) & \dots & \phi_{N_e}(x_1) \\ \phi_1(x_2) & \phi_2(x_2) & \dots & \phi_{N_e}(x_2) \\ \dots & \dots & \dots & \dots \\ \phi_1(x_{N_e}) & \phi_2(x_{N_e}) & \dots & \phi_{N_e}(x_{N_e}) \end{vmatrix}. \quad (2.30)$$

If the single-electron wave functions entering (2.30) are orthonormalized, i.e.,

$$\int \phi_i^*(x) \phi_j(x) dx = \delta_{ij} , \quad (2.31)$$

where δ_{ij} is the Dirac delta function, then the total wave function of the system is normalized too,

$$\int |\Psi_e(x_1, \dots, x_{N_e})|^2 dx_1 \dots dx_{N_e} = 1 . \quad (2.32)$$

The self-consistent Hartree-Fock potential, $U_{\text{HF}}(x)$, consists of a direct (local) and an exchange (non-local) terms:

$$\begin{aligned} U_{\text{HF}}(x) \phi_i(x) &= \sum_{j \leq F} \int dx' \phi_j^*(x') \frac{e^2}{|\mathbf{r} - \mathbf{r}'|} \phi_j(x') \phi_i(x) \\ &- \sum_{j \leq F} \int dx' \phi_j^*(x') \frac{e^2}{|\mathbf{r} - \mathbf{r}'|} \phi_i(x') \phi_j(x) , \end{aligned} \quad (2.33)$$

where the summation is carried out over all occupied states j below the Fermi level. One should note that the Hartree-Fock method exactly accounts for the exchange interaction between electrons, which has a non-local character.

Equations for single-electron wave functions are obtained by minimizing the total energy of the system with respect to small variations of $\phi_i(x)$. These equations are introduced as follows:

$$\begin{aligned} &\left[-\frac{\hbar^2}{2m_e} \nabla_i^2 - \sum_{\alpha=1}^N \frac{Z_\alpha e^2}{|\mathbf{r}_i - \mathbf{R}_\alpha|} \right] \phi_i(x) \\ &+ \sum_{j=1}^{N_e} \int \phi_j^*(x') \frac{e^2}{|\mathbf{r} - \mathbf{r}'|} [\phi_j(x') \phi_i(x) - \phi_i(x') \phi_j(x)] dx' = \varepsilon_i \phi_i(x) , \end{aligned} \quad (2.34)$$

where ε_i is the single-electron energy within the Hartree-Fock approximation. The total energy of the electronic system, E^{HF} , can be calculated using the single-electron wave functions from equation (2.34):

$$E^{\text{HF}} = \sum_i \varepsilon_i - \frac{1}{2} \sum_{i,j} \left[\left\langle ij \left| \frac{e^2}{|\mathbf{r} - \mathbf{r}'|} \right| ij \right\rangle - \left\langle ij \left| \frac{e^2}{|\mathbf{r} - \mathbf{r}'|} \right| ji \right\rangle \right] , \quad (2.35)$$

where $|i\rangle, |j\rangle \equiv \phi_i, \phi_j$.

2.3.2 Density-functional theory

Density-functional theory (DFT) [52,53] is another widely used approach for solving the many-electron problem within the single-particle approximation. This method accounts for many-electron correlation interaction by introducing the so-called correlation potential. Within this approach, one needs to solve the system of self-consistent Kohn-Sham equations [53] for the single-electron wave functions¹:

$$\left(-\frac{1}{2}\nabla_i^2 - \sum_{\alpha=1}^N \frac{Z_{\alpha}}{|\mathbf{r}_i - \mathbf{R}_{\alpha}|} + v_{\text{H}}(\mathbf{r}) + v_{\text{xc}}(\mathbf{r}) \right) \phi_i(\mathbf{r}) = \varepsilon_i \phi_i(\mathbf{r}) , \quad (2.36)$$

where the first term represents the kinetic energy of the i^{th} electron, the second term describes the Coulomb interaction between this electron and nuclei, and v_{H} is the Hartree (direct) part of electron-electron interaction:

$$v_{\text{H}}(\mathbf{r}) = \int \frac{\rho(\mathbf{r}')}{|\mathbf{r} - \mathbf{r}'|} d\mathbf{r}' , \quad (2.37)$$

with

$$\rho(\mathbf{r}) = \sum_{i=1}^{N_e} |\phi_i(\mathbf{r})|^2 \quad (2.38)$$

being the total electron density of the system. The term v_{xc} is the exchange-correlation potential which accounts for all many-body interactions in the system. It is defined as a functional derivative of the exchange-correlation energy functional:

$$v_{\text{xc}}(\mathbf{r}) = \frac{\delta E_{\text{xc}}[\rho(\mathbf{r})]}{\delta \rho(\mathbf{r})} . \quad (2.39)$$

A general limitation of the DFT approach is that one needs to define $v_{\text{xc}}(\mathbf{r})$ to solve single-electron Kohn-Sham equations, although the form of this potential in the general case is unknown [80]. Nevertheless, a large number of different approximations have been introduced so far (see, e.g., Refs. [81–87]), which allow one to solve a many-electron problem and to describe physical properties of a many-electron system with good accuracy. In the simplest case of a uniform electron gas, the potential $v_{\text{xc}}(\mathbf{r})$, which is calculated at a certain point in space, depends only on the value of electron density $\rho(\mathbf{r})$ at the same point. For a system with a non-uniform density distribution, $v_{\text{xc}}(\mathbf{r})$ depends not only on the value of electron density at the point r but also on its spatial variation in the vicinity of that point. In a more general case, the exchange-correlation

¹Further on in this chapter the atomic system of units, $m_e = |e| = \hbar = 1$, is utilized unless otherwise is indicated.

potential can be defined as:

$$v_{\text{xc}}[\rho] = v_{\text{xc}}[\rho(\mathbf{r}), \nabla\rho(\mathbf{r}), \nabla(\nabla\rho(\mathbf{r})), \dots] . \quad (2.40)$$

The two major classes of exchange-correlation functionals, which are most commonly utilized in DFT-based calculations, are the local functionals, $v_{\text{xc}}[\rho(\mathbf{r})]$, and the so-called gradient-corrected functionals, $v_{\text{xc}}[\rho(\mathbf{r}), \nabla\rho(\mathbf{r})]$.

As the exact form of the exchange-correlation potential is unknown, one has to use some approximations, which would allow one to get either an analytic expression for a particular case or some numerical approximations for $v_{\text{xc}}(\mathbf{r})$. The simplest and one of the most commonly used approaches is the so-called local density approximation (LDA), which assumes that the potential $v_{\text{xc}}(\mathbf{r})$ is local:

$$v_{\text{xc}}^{\text{LDA}}(\mathbf{r}) = \frac{\delta E_{\text{xc}}[\rho]}{\delta\rho(\mathbf{r})} = \frac{\partial}{\partial\rho(\mathbf{r})} [\rho \epsilon_{\text{xc}}(\rho)] , \quad (2.41)$$

where $E_{\text{xc}}[\rho(\mathbf{r})] = \int \rho(\mathbf{r})\epsilon_{\text{xc}}(\rho)\text{d}\mathbf{r}$ and $\epsilon_{\text{xc}}(\rho)$ defines the exchange-correlation energy per particle. Based on the concept of the homogeneous electron gas (HEG), the LDA was introduced initially for the solution of a many-electron problem in the case of systems with slowly varying electron density [81,82]. It approximates the local energy ϵ_{xc} as the value for the HEG at the local density, $\epsilon_{\text{xc}}^{\text{LDA}}(\rho(\mathbf{r})) \approx \epsilon_{\text{xc}}^{\text{HEG}}(\rho)|_{\rho=\rho(\mathbf{r})}$.

The energy $\epsilon_{\text{xc}}^{\text{LDA}}(\mathbf{r})$ is decomposed into the so-called Slater exchange potential, which describes exchange interaction in the HEG, and a correlation potential [88]:

$$\epsilon_{\text{xc}}^{\text{LDA}}(\mathbf{r}) = \epsilon_{\text{x}}^{\text{LDA}}(\mathbf{r}) + \epsilon_{\text{c}}^{\text{LDA}}(\mathbf{r}) = -\frac{3}{4} \left(\frac{3}{\pi} \right)^{1/3} \rho^{1/3}(\mathbf{r}) + \epsilon_{\text{c}}^{\text{LDA}}(\mathbf{r}) . \quad (2.42)$$

Analytic expressions for the correlation energy $\epsilon_{\text{c}}^{\text{LDA}}(\mathbf{r})$ of the HEG are not known except for the low- and high-density limits that correspond to the case of infinitely-strong and infinitely-weak correlation [88]. However, in Ref. [89], numerical values of $\epsilon_{\text{c}}^{\text{LDA}}(\mathbf{r})$ were derived for several intermediate values of density. Based on these results, several different interpolation formulas for $\epsilon_{\text{c}}(\mathbf{r})$ were introduced to connect the high- and low-density limits [81,82]. These parameterizations are widely used nowadays in various codes for quantum-chemical calculations. One should note that, although the LDA is exact in the limit of slowly varying densities, the application of this approach to the systems with much less uniform density distribution, such as small molecules or atomic clusters, was justified during the past decades by producing reasonable results for physical properties of these systems [88].

In this study, most calculations within the DFT framework were performed using the so-called PBE functional, developed by Perdew, Burke, and Ernzerhof [85].

This functional belongs to the class of generalized gradient approximations (GGA) for the exchange-correlation energy, $E_{xc} = E_{xc}[\rho(\mathbf{r}), \nabla\rho(\mathbf{r})]$. PBE is a non-empirical, parameter-free functional, which was constructed to include the gradient correction without introducing experimentally fitted parameters. Since its development in 1996, it has been known for its general applicability and provided rather accurate results for a wide range of systems.

The exact expressions for the PBE functional are quite complicated; the detailed explanation of all parameters entering these expressions can be found in the original paper [85] and a number of subsequent works [90, 91]. The main ideas of this approach are briefly outlined below.

Similar to the LDA, GGA functionals are also split into the exchange and correlation terms:

$$E_{xc}^{\text{GGA}} = E_x^{\text{GGA}} + E_c^{\text{GGA}} . \quad (2.43)$$

The exchange functional is expressed as [92]:

$$E_x^{\text{GGA}} = \int \rho(\mathbf{r}) \epsilon_x^{\text{HEG}}(\rho) F_x(s) \, \mathbf{dr} , \quad (2.44)$$

where $\epsilon_x^{\text{HEG}}(\rho)$ is the energy per particle in the HEG approximation (the first term on the r.h.s. of (2.42)) and $F_x(s)$ is the so-called GGA enhancement factor which depends on a reduced density gradient $s \propto |\nabla\rho|/\rho^{4/3}$.

The GGA correlation functional is expressed as [83]

$$E_c^{\text{GGA}} = \int \rho(\mathbf{r}) [\epsilon_c^{\text{HEG}}(r_s) + H(r_s, t)] \, \mathbf{dr} , \quad (2.45)$$

where $r_s = (4\pi\rho(\mathbf{r})/3)^{-1/3}$ is the so-called Wigner-Seitz radius which characterizes the density of the system [93], and $t \propto |\nabla\rho|/\rho^{7/6}$ is another scaled density gradient. Similar to (2.44), Eq. (2.45) can be expressed as [90]

$$E_c^{\text{GGA}} = \int \rho(\mathbf{r}) \epsilon_c^{\text{HEG}}(\rho) F_c(r_s, t) \, \mathbf{dr} , \quad (2.46)$$

where

$$F_c(r_s, t) \equiv 1 + \frac{H(r_s, t)}{\epsilon_c^{\text{HEG}}(r_s)} . \quad (2.47)$$

The gradient contribution to the PBE correlation,

$$H^{\text{PBE}} = \gamma \ln \left[1 + \frac{\beta}{\gamma} \frac{t^2 + At^4}{1 + At^2 + A^2t^4} \right] , \quad (2.48)$$

where $\beta \approx 6.67 \cdot 10^{-2}$, $\gamma \approx 3.11 \cdot 10^{-2}$, and $A = \beta/\gamma [\exp(-\epsilon_c^{\text{HEG}}/\gamma) - 1]^{-1}$, was derived

from several physical conditions in the slowly ($t \rightarrow 0$) and rapidly ($t \rightarrow \infty$) varying density limits. A detailed explanation of these conditions and physical meanings of the above-mentioned parameters is given in Ref. [85]. In the general case, the above-defined functionals depend also on the relative spin polarization $\zeta = (\rho_{\uparrow} - \rho_{\downarrow})/\rho$, so that $\epsilon_c^{\text{HEG}} = \epsilon_c^{\text{HEG}}(r_s, \zeta)$ and $H = H(r_s, \zeta, t)$.

2.4 Time-dependent density-functional theory

Time-dependent density-functional theory (TDDFT) [54] is an approximate method of solving the time-dependent Schrödinger equation, which allows one to study properties of many-electron systems as a function of time. In this approach, the Schrödinger equation is substituted with a set of time-dependent single-particle Kohn-Sham equations. On the analogy of the Kohn-Sham method [53] which is the basic principle of DFT, its generalization to a time-dependent case is based on a one-to-one correspondence between an external time-dependent potential $v_{\text{ext}}(\mathbf{r}, t)$, in which the motion of a system of non-interacting particles is considered, and the time-dependent electron density $\rho(\mathbf{r}, t)$ of a real many-electron system.

The calculation of photoabsorption spectra of many-electron systems by means of TDDFT can be performed either in the time domain or in the frequency domain. In the former case, the time evolution of an induced dipole moment is studied by integrating time-dependent Kohn-Sham equations, while in the latter case one performs the Fourier transform of time-dependent quantities. Depending on the utilized methodology for representing single-particle Kohn-Sham orbitals in TDDFT calculations, either a three-dimensional real-space grid or a plane-wave basis set is utilized, respectively. The main advantage of such an approach is that convergence of the numerical solution can be controlled in each case with a single parameter, namely with the grid spacing in real space or with the kinetic energy cutoff in a plane-wave approach [94].

The time-dependent single-particle Kohn-Sham equation can be written as follows:

$$i \frac{\partial \phi_i(\mathbf{r}, t)}{\partial t} = \hat{H}(t) \phi_i(\mathbf{r}, t) , \quad (2.49)$$

where

$$\hat{H}(t) = -\frac{1}{2} \nabla^2 + v_{\text{eff}}(\mathbf{r}, t) \quad (2.50)$$

is a time-dependent single-particle Kohn-Sham Hamiltonian, and the effective potential $v_{\text{eff}}(\mathbf{r}, t)$ is defined as

$$v_{\text{eff}}(\mathbf{r}, t) = v_{\text{ext}}(\mathbf{r}, t) + v_{\text{H}}(\mathbf{r}, t) + v_{\text{xc}}(\mathbf{r}, t) . \quad (2.51)$$

The function $v_{\text{ext}}(\mathbf{r}, t)$ defines the potential created by a time-dependent external electric field. Formally, the external potential also accounts for the contribution due to the Coulomb interaction of electrons with the nuclei. The electrostatic and exchange-correlation potentials are defined as:

$$v_{\text{H}}(\mathbf{r}, t) = \int \frac{\rho(\mathbf{r}', t)}{|\mathbf{r} - \mathbf{r}'|} d\mathbf{r}' , \quad v_{\text{xc}}(\mathbf{r}, t) = \frac{\delta E_{\text{xc}}[\rho(\mathbf{r}, t)]}{\delta \rho(\mathbf{r}, t)} . \quad (2.52)$$

Similar to DFT, $v_{\text{xc}}(\mathbf{r}, t)$ is a functional derivative of the exchange-correlation energy functional $E_{\text{xc}}[\rho(\mathbf{r}, t)]$ which accounts for all many-body interactions in the system.

Knowing single-electron orbitals $\phi_i(\mathbf{r}, t)$, one can define the electron density of the system:

$$\rho(\mathbf{r}, t) = \sum_{i=1}^{N_e} \phi_i(\mathbf{r}, t) \phi_i^*(\mathbf{r}, t) , \quad (2.53)$$

where the summation is performed over all occupied states.

The electrostatic and exchange-correlation potentials are functionally dependent on electron density, $v_{\text{H}}(\mathbf{r}, t) \equiv v_{\text{H}}[\rho(\mathbf{r}, t)]$, $v_{\text{xc}}(\mathbf{r}, t) \equiv v_{\text{xc}}[\rho(\mathbf{r}, t)]$, which, in turn, depends on the effective potential $v_{\text{eff}}(\mathbf{r}, t)$. Thus, the solution of self-consistent Kohn-Sham equations (2.49)–(2.53) should be sought iteratively. As a rule, the potential $v_{\text{eff}}(\mathbf{r}, t)$ is calculated first based on some initial guess for $\rho(\mathbf{r}, t)$. Then, the derived value of the potential is utilized to solve the Kohn-Sham equations. Solving them, one can define a set of single-electron orbitals $\{\phi_i(\mathbf{r}, t)\}$ which, in turn, allow one to get the next approximation for electron density.

At present, a significant part of TDDFT-based studies concerns the calculation of photoabsorption spectra of small molecules and solids in the linear regime using the dipole approximation. The linear response theory aims at studying the variation of a given physical observable due to the application of a weak external perturbation to a many-particle system. Within this framework [95], the external potential acting on the system can be represented as a sum of a time-independent part, $v_{\text{ext}}^0(\mathbf{r})$, and a time-dependent perturbation, $v'_{\text{ext}}(\mathbf{r}, t)$:

$$v_{\text{ext}}(\mathbf{r}, t) = v_{\text{ext}}^0(\mathbf{r}) + v'_{\text{ext}}(\mathbf{r}, t) . \quad (2.54)$$

Application of the external perturbation leads to variation of the electron density of the system. Therefore, the time evolution of the electron density can be represented as a sum of two terms,

$$\rho(\mathbf{r}, t) = \rho_0(\mathbf{r}) + \delta\rho(\mathbf{r}, t) , \quad (2.55)$$

where $\rho_0(\mathbf{r})$ is the unperturbed ground-state density and $\delta\rho(\mathbf{r}, t)$ describes variation of the electron density due to the perturbation $v'_{\text{ext}}(\mathbf{r}, t)$.

In this work, the response of a system to an external perturbation is considered in the frequency representation. Therefore, one needs to perform the Fourier transform of the time-dependent quantities. In the linear regime, the Fourier transform of $\delta\rho(\mathbf{r}, t)$ reads

$$\delta\rho(\mathbf{r}, \omega) = \int \chi(\mathbf{r}, \mathbf{r}', \omega) v'_{\text{ext}}(\mathbf{r}', \omega) d\mathbf{r}' , \quad (2.56)$$

where $v'_{\text{ext}}(\mathbf{r}, \omega)$ is the Fourier transform of the external perturbation $v'_{\text{ext}}(\mathbf{r}, t)$, and $\chi(\mathbf{r}, \mathbf{r}', \omega)$ is the generalized frequency-dependent susceptibility of the system.

In the case of a system of non-interacting particles, which is considered within the Kohn-Sham approach, variation of electron density, $\delta\rho(\mathbf{r}, \omega)$, can be written as:

$$\delta\rho(\mathbf{r}, \omega) = \int \chi_0(\mathbf{r}, \mathbf{r}', \omega) v'_{\text{eff}}(\mathbf{r}', \omega) d\mathbf{r}' , \quad (2.57)$$

where $\chi_0(\mathbf{r}, \mathbf{r}', \omega)$ is the susceptibility of the system of non-interacting particles that is defined through single-electron ground-state orbitals $\phi_i(\mathbf{r})$ and the corresponding energies ε_i :

$$\chi_0(\mathbf{r}, \mathbf{r}', \omega) = \sum_{ij} (n_i - n_j) \frac{\phi_j^*(\mathbf{r})\phi_i(\mathbf{r})\phi_i^*(\mathbf{r}')\phi_j(\mathbf{r}')}{\varepsilon_j - \varepsilon_i + \omega + i\eta} , \quad (2.58)$$

where n_i and n_j are the occupation numbers. In this expression, the ground-state wave functions, $\phi_i(\mathbf{r})$ and $\phi_j(\mathbf{r})$, describe both occupied and empty states. The function $v'_{\text{eff}}(\mathbf{r}, \omega)$ describes a Fourier transform of the linear variation of the Kohn-Sham effective potential $v_{\text{eff}}(\mathbf{r}, t)$ (2.51), which is caused, in turn, by the variation of electron density $\delta\rho(\mathbf{r}, t)$. The variation of the Kohn-Sham potential is defined in the frequency domain as:

$$v'_{\text{eff}}(\mathbf{r}, \omega) = v'_{\text{ext}}(\mathbf{r}, \omega) + v'_{\text{H}}(\mathbf{r}, \omega) + v'_{\text{xc}}(\mathbf{r}, \omega) . \quad (2.59)$$

The linear response of the electrostatic and exchange-correlation potentials induced by the application of v'_{ext} reads as

$$v'_{\text{H}}(\mathbf{r}, \omega) = \int \frac{\rho'(\mathbf{r}', \omega)}{|\mathbf{r} - \mathbf{r}'|} d\mathbf{r}' , \quad v'_{\text{xc}}(\mathbf{r}, \omega) = \int \frac{\delta v_{\text{xc}}(\mathbf{r}, \omega)}{\delta\rho(\mathbf{r}', \omega)} \rho'(\mathbf{r}', \omega) d\mathbf{r}' . \quad (2.60)$$

In order to avoid inconsistency, variation of the electron density, $\delta\rho(\mathbf{r}, \omega)$, is denoted in (2.60) as $\rho'(\mathbf{r}, \omega)$, while $\delta v_{\text{xc}}(\mathbf{r}, \omega)/\delta\rho(\mathbf{r}', \omega)$ stands for a functional derivative of the exchange-correlation potential.

Apart from the non-local spatial dependence of electron density, the exact exchange-correlation functional should also have a non-local dependence on time. The dependency on density at earlier times is usually referred to as "memory effects". However, most applications of the linear-response approach rely on the adiabatic approximation, where the exchange-correlation functional is assumed to be local in time; thus, the memory

dependence can be disregarded [96]. In other words, the functional derivative of a time-dependent (or frequency-dependent) exchange-correlation potential corresponds to that of the ground-state functional, calculated at the ground-state density $\rho_0(\mathbf{r})$:

$$\frac{\delta v_{\text{xc}}(\mathbf{r}, \omega)}{\delta \rho(\mathbf{r}', \omega)} = \left. \frac{\delta v_{\text{xc}}(\mathbf{r})}{\delta \rho(\mathbf{r}')} \right|_{\rho(\mathbf{r})=\rho_0(\mathbf{r})} . \quad (2.61)$$

Variation of the effective Kohn-Sham potential, $v'_{\text{eff}}(\mathbf{r}, \omega)$, and the external perturbation $v'_{\text{ext}}(\mathbf{r}, \omega)$ can be obtained by inverting equations (2.56) and (2.57):

$$v'_{\text{eff}}(\mathbf{r}, \omega) = \int \chi_0^{-1}(\mathbf{r}, \mathbf{r}', \omega) \delta \rho(\mathbf{r}, \omega) d\mathbf{r}' , \quad (2.62)$$

$$v'_{\text{ext}}(\mathbf{r}, \omega) = \int \chi^{-1}(\mathbf{r}, \mathbf{r}', \omega) \delta \rho(\mathbf{r}, \omega) d\mathbf{r}' . \quad (2.63)$$

By utilizing together expressions (2.62), (2.63), and (2.60), and using the definition for variation of the effective Kohn-Sham potential (2.59), one gets a Dyson-type equation for the inverse susceptibility:

$$\chi^{-1}(\mathbf{r}, \mathbf{r}', \omega) = \chi_0^{-1}(\mathbf{r}, \mathbf{r}', \omega) - \frac{1}{|\mathbf{r} - \mathbf{r}'|} - \frac{\delta v_{\text{xc}}(\mathbf{r}, \omega)}{\delta \rho(\mathbf{r}', \omega)} . \quad (2.64)$$

For the perturbation due to a uniform electric field, $v'_{\text{ext}}(\mathbf{r}, \omega) = -\mathbf{E}(\omega) \cdot \mathbf{r}$, the Fourier transform of the induced dipole moment reads

$$d_i(\omega) = \sum_j \alpha_{ij}(\omega) E_j(\omega) . \quad (2.65)$$

Here i, j denote the Cartesian components, and $\alpha_{ij}(\omega)$ is the dynamic polarizability tensor which describes the linear response of the system to the external electric field:

$$\alpha_{ij}(\omega) = - \int r_i \chi(\mathbf{r}, \mathbf{r}', \omega) r'_j d\mathbf{r} d\mathbf{r}' , \quad (2.66)$$

and r_i, r'_j are the components of the position vectors \mathbf{r} and \mathbf{r}' .

The photoabsorption cross section of a randomly oriented molecular system is expressed as

$$\sigma_\gamma(\omega) = \frac{4\pi\omega}{c} \text{Im} \bar{\alpha}(\omega) , \quad (2.67)$$

where $\bar{\alpha}(\omega)$ denotes the isotropic average polarizability calculated as a sum of the diagonal elements of the polarizability tensor $\alpha_{ij}(\omega)$,

$$\bar{\alpha}(\omega) = \frac{1}{3} \sum_{j=1}^3 \alpha_{jj}(\omega) , \quad (2.68)$$

and c is the speed of light.

Within the approach introduced in Refs. [94, 97, 98], the electron density variation, $\delta\rho(\mathbf{r}, \omega)$, is expressed via the so-called Liouvillian operator \mathcal{L} ,

$$(\omega - \mathcal{L}) \cdot \delta\rho(\mathbf{r}, \omega) = [v'_{\text{ext}}(\mathbf{r}, \omega), \rho_0] , \quad (2.69)$$

whose action onto $\delta\rho(\mathbf{r}, \omega)$ is defined as:

$$\mathcal{L} \cdot \delta\rho(\mathbf{r}, \omega) = [H_0, \delta\rho(\mathbf{r}, \omega)] + [v'_H(\mathbf{r}, \omega), \rho_0] + [v'_{\text{xc}}(\mathbf{r}, \omega), \rho_0] , \quad (2.70)$$

and H_0 is the ground-state Kohn-Sham Hamiltonian calculated within the DFT approach. The polarizability tensor $\alpha_{ij}(\omega)$ is defined then by the off-diagonal matrix element of the resolvent of the Liouvillian \mathcal{L} :

$$\alpha_{ij}(\omega) = -\langle r_i | (\omega - \mathcal{L})^{-1} \cdot [r_j, \rho_0] \rangle . \quad (2.71)$$

Based on the frequency representation of the response function, this method allows one to calculate the photoabsorption spectrum of a complex many-electron system in a broad photon energy range (see Refs. [94, 97, 98] for details). However, this approach does not allow one to get information on partial ionization cross sections which describe ionization of particular molecular orbitals. The reason of this drawback is that only the occupied states are required for performing the calculations, and there is no need to calculate any empty states [97, 98]. It makes this method substantially different from the Casida's approach [99], which is implemented in many codes for *ab initio* calculations. Within the latter one, it is possible to calculate each individual excitation and to assign it to a specific transition. In general, this operation is feasible only in a limited range of excitation energies, which is not typically larger than 10 eV and depends also on the density of the excitation energies [100]. Alternatively, the method, introduced in Refs. [94, 97, 98], allows one to compute the absorption spectrum in a broad range of energies but a systematic way to assign the transitions is missed.

Chapter 3

Investigation of stability and thermo-mechanical properties of nanomaterials and validation of classical interatomic potentials

A fundamental understanding of the physicochemical mechanisms occurring in nanomaterials is essential for further developments of these materials for technological applications. This step should be based on the study of the full atomistic dynamics in a system. Molecular dynamics (MD) simulations of dynamical processes involving large systems allow one to overcome the problem of computational demand by calling for a classical potential to enable the treatment of appropriate spatial and time scales. Thus, classical MD simulations can provide nanoscale insights into structural and dynamical features of various systems. However, it can only be done if interatomic potentials, which are used to model interactions in the system, correctly describe its properties.

The interatomic interactions are parameterized in classical MD simulations using various empirical potentials of the force fields (see Section 2.2). However, the accuracy of the force field approach for the description of interactions between the atoms is sometimes a bottleneck of the MD scheme. Most classical interatomic potentials for modeling metallic, organic, and biomolecular systems are derived to fit the results of *ab initio* calculations or experimental data in order to reproduce ground-state properties of a system. For instance, parameters of classical interatomic potentials for metal systems are often chosen to reproduce bulk properties of a perfect crystalline structure. In the meantime, it is not *a priori* clear whether the parametrization obtained for bulk systems could also describe adequately the system properties on the nanoscale. The applicability of the classical force fields to the description of nanoscale systems, consisting of several

tens-hundreds of atoms, with a reasonable accuracy is important, for instance, in the case of nanostructured materials, where grains or nanocrystals have a typical size of about a few nanometers.

Another important issue is that classical force fields usually poorly describe highly-excited vibrational states when the system under study is far from the potential energy minimum. This is the case, for instance, when a phase transition occurs in the system [101]. The proper quantitative description of phase transitions in general and the melting process in particular by means of MD simulations is a major scientific challenge that concerns metal materials, as well as inorganic and biomolecular systems, like proteins or water.

In this chapter, we explore the ability of existing classical interatomic potentials to reproduce the system properties on the nanoscale, assuming that these potentials are already fitted to reproduce features of the perfect bulk materials. It is demonstrated that it is possible to describe correctly, with the same set of parameters, the main properties of the systems consisting of several tens of atoms as well as those of an ideal system comprising several million atoms. We also propose a recipe for constructing an interatomic potential that is able to correctly reproduce both the melting temperature and the ground-state properties of metal systems by means of classical MD simulations.

3.1 Benchmark of classical force fields by *ab initio* calculations of atomic clusters

In this study, we evaluate the accuracy of the existing interatomic potentials for description of metal systems on the atomistic scale by analyzing stability of small atomic clusters. As a case study, monatomic and bimetallic clusters composed of titanium and nickel are considered.

The choice of the materials has been motivated by the fact that titanium and its alloys have been widely studied in view of their medical application [46, 47]. A nickel-titanium alloy with almost equal concentration of both types of atoms manifests the so-called superelastic behavior [48], which is quite similar to that of living tissues. This compound is thus an excellent candidate for implant material capable of mimicking the mechanical behavior of bones [49].

Investigation of properties of transition-metal clusters by means of *ab initio* methods is known to be a challenging task due to the presence of partially filled *d* orbitals and their hybridization with the valence *s* states [102]. Since an accurate description of the correlation effects is crucial in this case, the Hartree-Fock approach is considered as a not reliable one [103]. The DFT methods based on the local-density approxima-

tion (LDA) are also not sufficient to describe strong correlation between the localized d electrons of transition-metal clusters, as they are claimed to produce wrong values for the bond lengths and total energy of these systems [104]. A better choice for the *ab initio* investigation of atomic clusters of transition elements is thus to utilize the DFT methods based on the generalized gradient approximation (GGA) [105].

In this study, we have performed the *ab initio*-based calculations using the GGA-based PW91 exchange-correlation functional developed by Perdew and Wang [83,84] in combination with the DGDZVP2 basis set [106]. The utilized functional is a predecessor to the PBE functional described in Section 2.3.2. The ground-state geometries of atomic clusters were optimized using Gaussian 09 computer package [107]. In order to define the ground state of the systems, various cluster geometries and spin states were considered.

Classical geometry optimization of atomic clusters was performed using MBN Explorer [61] package. The cluster geometry optimization was carried out within the classical approach using the velocity quenching algorithm. Within this algorithm, translational contributions to the kinetic energy of all individual particles in the system are monitored during the simulation. When the translational kinetic energy of an arbitrary particle is maximal, the absolute value of its velocity is set equal to zero. The points in the configurational space, at which the translational parts of the kinetic energy are maximal, correspond to the minimum of a potential well, in which a particle moves [61].

In order to describe many-body interactions between titanium and nickel atoms, the following representation of the Finnis-Sinclair (FS)-type potential (see Eq. (2.23), (2.24) and (2.25)) was utilized:

$$U_{FS} = \sum_{i=1}^N \left(\sum_{\substack{j=1 \\ (i \neq j)}}^N A_{\alpha\beta} e^{-p_{\alpha\beta} \left(\frac{r_{ij}}{d_{\alpha\beta}} - 1 \right)} - \sqrt{\sum_{\substack{j=1 \\ (i \neq j)}}^N \xi_{\alpha\beta}^2 e^{-2q_{\alpha\beta} \left(\frac{r_{ij}}{d_{\alpha\beta}} - 1 \right)}} \right). \quad (3.1)$$

The parameters entering this expression were defined in Chapter 2, see (2.24) and (2.25). When simulating a bimetallic system, these parameters depend on the type of atoms ($\alpha, \beta = \text{Ti or Ni}$) chosen within the summation. When $\alpha = \beta$, i.e., Ti–Ti or Ni–Ni interaction is described, this exponential parametrization of the potential coincides with the form presented in Section 2.2. We have utilized the parameter set proposed in Ref. [108] that reproduces main properties, such as the cohesive energy, lattice parameters and elastic constants, of the face-centered cubic (Strukturbericht designation B2) phase of the Ni–Ti crystal at 0 K and those of the bulk nickel and titanium. Values of the parameters used in the present calculations are summarized in Table 3.1.

Since most of the many-body potentials go nearly to zero at large distances, a cutoff

Table 3.1: Parameters of the FS-type potential for the interactions between titanium and nickel atoms [108]

	d (Å)	A (eV)	p	ξ (eV)	q
Ti-Ti	2.950	0.153	9.253	1.879	2.513
Ni-Ti	2.607	0.300	7.900	2.480	3.002
Ni-Ni	2.490	0.104	11.198	1.591	2.413

radius, r_c , is frequently used to reduce the computation time. If such a cutoff radius is used, the interatomic potentials and, subsequently, the forces are neglected for atoms being at distances $r > r_c$ from each other. The parameter set given in Table 3.1 was obtained in Ref. [108] with the cutoff distance of 4.2 Å as another adjustable parameter. In this study, this value was utilized for all considered types of interaction.

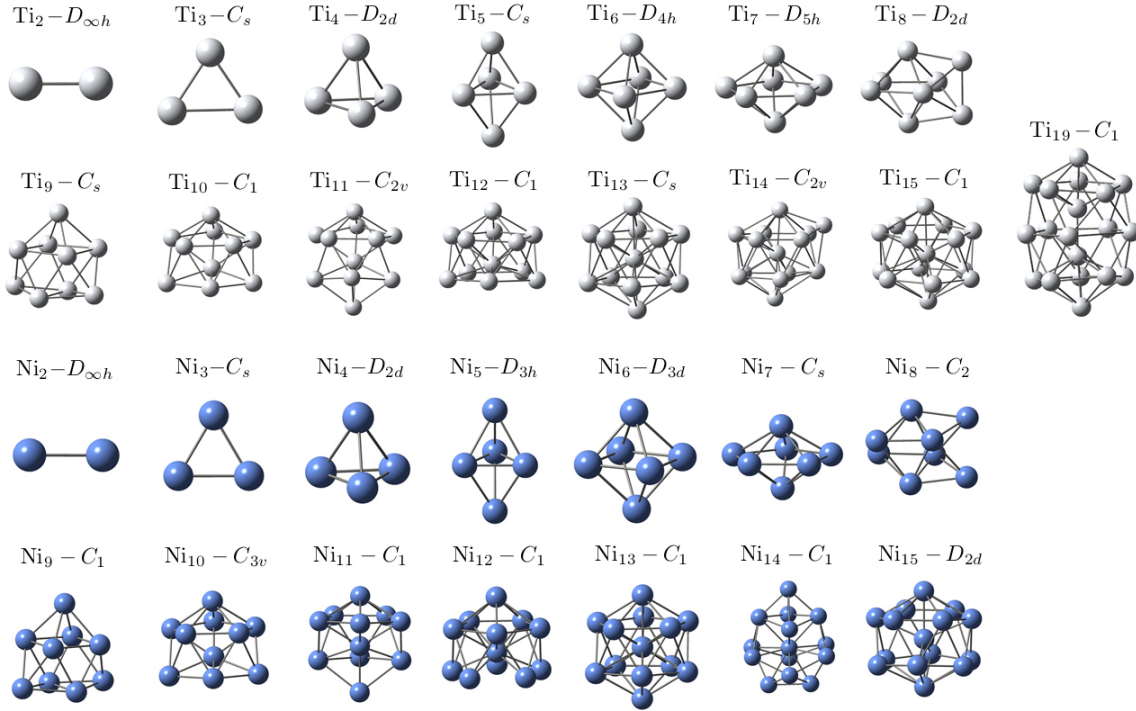


Figure 3.1: Optimized geometries of small Ti_N ($N = 2 - 15, 19$) and Ni_N ($N = 2 - 15$) clusters obtained by means of the *ab initio* approach. The label above each cluster image indicates its symmetry point group. The figure is adapted from Ref. [23].

Figure 3.1 shows the ground-state geometries of small titanium and nickel clusters consisting of up to 19 atoms that were found by means of the DFT approach. The results of calculations demonstrate that the small transition metal clusters form compact structures maximizing the coordination number. As illustrated in the figure, most studied clusters possess rather low symmetry. It can be explained by the Jahn-Teller effect, which appears in the geometrical distortion of the clusters leading to decrease of their ground-state energies [22].

The classical geometry optimization for pure titanium and nickel clusters results in the geometries similar to those obtained by the *ab initio* method, except for higher symmetry of the systems. Within the classical approach the clusters were optimized as almost regular structures. This difference can be explained in terms of the charge transfer between the atoms of a cluster as well as the Jahn-Teller and spin effects, which are not accounted for within the classical framework. The results of classical geometry optimization of Ti_N and Ni_N clusters correspond also to those, obtained previously using the embedded-atom method [109].

The ability of the classical force fields to adequately describe nanoscale systems was evaluated by the analysis of the binding energy of pure titanium and nickel clusters. The binding energy per atom is defined as

$$E_b/N = E_1 - E_N/N, \quad (3.2)$$

where E_N is the energy of a cluster consisting of N atoms, and E_1 is the energy of a single Ti or Ni atom.

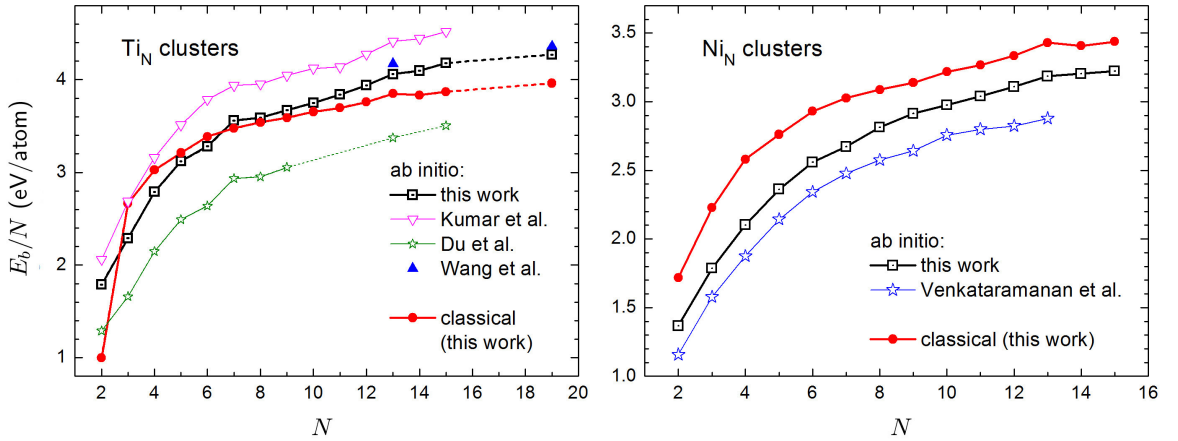


Figure 3.2: Binding energy per atom for the most stable titanium (left panel) and nickel (right panel) clusters as a function of number of atoms N . The black (open squares) and red (filled circles) curves illustrate the results of present DFT calculations and classical optimization, respectively. Other symbols represent results of previous DFT studies [110–113] performed at a similar level of theory. The figure is adapted from Ref. [23].

The dependence of the binding energy per atom for the most stable titanium clusters on cluster size is illustrated in the left panel of Figure 3.2. Results of the present *ab initio*-based calculations (labeled with black squares) are compared to those of other *ab initio* studies [110–112]. As shown in the figure, all presented curves have a similar behavior in spite of a broad range of the obtained values. For $N = 7$ and 13, a change of the slope of the E_b/N curve obtained within the *ab initio* framework is observed,

that illustrates the increased stability of Ti clusters with "magic" numbers [114]. The existence of the magic numbers for transition metal clusters (e.g., $N = 7, 13, 15, 19, 25$ for neutral Ti_N clusters) reflects the geometric effects but not the electronic effects [102]. Most properties of clusters of transition elements reflect the rather localized behavior of d electrons as opposed to the clusters and solids of alkali metals whose properties are dominated by the delocalized behavior of the external $s - p$ electrons [115, 116].

The red line (with filled circles) in the left panel of Figure 3.2 illustrates the results of classical optimization. They generally correspond to the results of the quantum-chemical calculations, although the classical framework underestimates significantly the binding energy of the Ti_2 dimer and slightly under- or overestimates it for larger clusters. The discrepancies between the DFT-based and classical calculations for the smallest clusters ($N = 2 - 4$) can arise due to quantum effects, occurring in finite-size systems. One should note, however, that the discrepancy between the results of classical optimization and DFT-based calculations of small atomic clusters is within the limits typical for the discrepancies arising from the utilization of different exchange-correlation functionals. It is hardly possible to reproduce the specific quantum phenomena, like electronic shell closure, with the classical force fields. However, the relative contribution of these effects is not so significant and it apparently does not influence much on the overall (average) evolution of the system properties with the system size.

As an additional benchmark of the utilized force fields, we used them for optimization of large titanium and nickel crystalline structures consisting of about one million atoms. In the case of the titanium crystal, we obtained the value of cohesive energy $E_{\text{coh}} = 4.80$ eV, which corresponds to the experimentally measured cohesive energy of the bulk titanium, $E_{\text{coh}}^{\text{exp}} = 4.85$ eV [117].

One should note also that the DFT-based calculations of titanium clusters result in another asymptotic behavior of the $E_b(N)$ function that leads to significantly higher values of the binding energy as compared to the results of classical optimization and the experimental data. It is known that pure DFT methods, such as LDA or GGA, provide, in general, a reliable description of the ground-state properties of solids but are far less successful being applied to materials, where the constituent atoms contain partly filled d or f shells, such as transition metals [118, 119]. The origin of the failure of DFT in transition metals is usually associated with an inadequate description of the strong Coulomb repulsion between d electrons [120]. With regard to the cohesive energy, the conventional DFT methods, such as LDA and GGA, overestimate it for most of transition-metal systems, and for titanium in particular, resulting in the values of 5.9 eV and 6.7 eV [121], respectively, which are as large as 20–40% higher than the experimental value of 4.85 eV [117].

The binding energy per atom for the most stable nickel clusters, optimized within the

DFT (black squares) and classical (red circles) frameworks, is demonstrated in the right panel of Figure 3.2. The results of the *ab initio* study by Venkataramanan et al. [113] are also given for the comparison. Calculating the cohesive energy for an ideal nickel crystal, we got the value $E_c = 4.47$ eV, which also corresponds to the experimentally measured cohesive energy of bulk nickel, $E_c^{\text{exp}} = 4.44$ eV [117].

Substituting one titanium atom by a nickel atom in the optimized Ti_N clusters, we studied bimetallic Ti_{N-1}Ni compounds. Various positions of the nickel atom in the clusters were considered. Geometrical structures of the most stable Ni-doped titanium clusters calculated within the PW91PW91/DGDZVP2 method are presented in Figure 3.3.

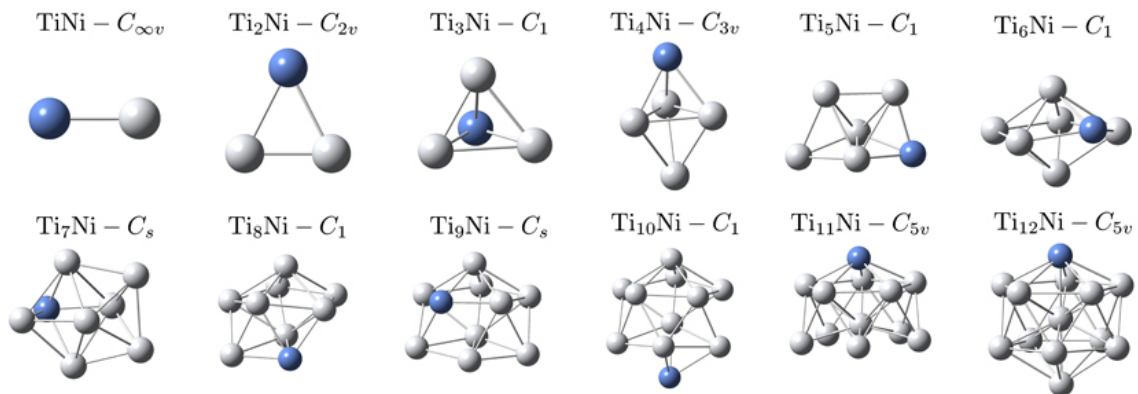


Figure 3.3: Optimized geometries of Ni-doped titanium clusters Ti_{N-1}Ni ($N \leq 13$) calculated within the PW91PW91/DGDZVP2 method. Label above each cluster image indicates the point symmetry group of the cluster. The figure is adapted from Ref. [22]

Similar to the analysis performed for pure titanium and nickel clusters, we carried out classical geometry optimization of the Ti_{N-1}Ni clusters and compared the obtained results to that of DFT calculations. The binding energy per atom as a function of cluster size for bimetallic Ti_{N-1}Ni clusters,

$$E_b/N = (N - 1)E_1[\text{Ti}] + E_1[\text{Ni}] - E_N[\text{Ti}_{N-1}\text{Ni}]/N, \quad (3.3)$$

calculated within the *ab initio* and classical approaches is presented in Figure 3.4. It is seen that the classical force field for a bimetallic system does not reproduce well the results of the more accurate DFT calculations for very small compounds. However, with increasing the number of atoms in a cluster, the relative difference between the results obtained within the two approaches becomes significantly smaller, and one can state that starting from Ti_7Ni the classical results correspond to those from the *ab initio* calculations. This behavior can be explained by a significant charge redistribution from the host titanium environment to the embedded nickel atom [22]. It can be explained

in terms of different values of electronegativity for the Ni and Ti atoms. Due to the larger electronegativity of Ni (1.91) comparing to that of Ti (1.54), the dopant atom gains an additional negative charge. With increasing cluster size and, respectively, the number of Ti atoms in a cluster, the gained negative charge of the Ni atom decreases. For $N = 11$ and 13 the Ni atom gains an additional positive charge equal to $0.1e$ and $0.07e$, respectively. It can be explained by the fact that the most stable configurations of Ti_{N-1}Ni ($N > 10$) clusters are obtained when the Ni atom is located on the surface of a cluster rather than in the center (see Figure 3.3). On the contrary, the central atom in the Ti_{12}Ni cluster gains an additional negative charge equal to $-2.0e$.

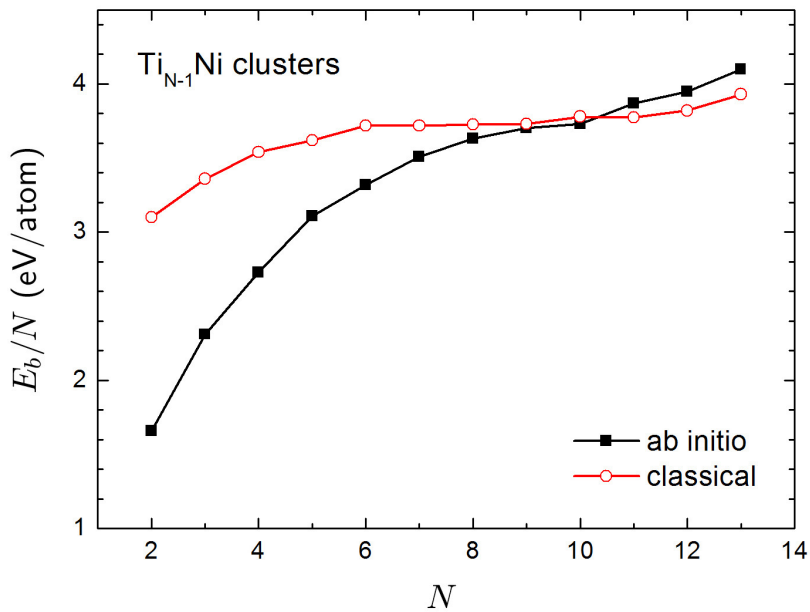


Figure 3.4: Binding energies per atom for the most stable Ni-doped titanium clusters as a function of cluster size. Black line (squares) represents the results of DFT calculation, while red line (open circles) represents the results of the classical simulations. To describe the Ni-Ti interaction in the simulations, the FS-type potential with the parametrization developed in Ref. [108] was used. The figure is adapted from Ref. [22].

Concluding the analysis of energetic properties of small transition metal clusters, carried out within the two different approaches, one can summarize that the force fields, which are parameterized to reproduce bulk properties of perfect Ti, Ni, and Ni-Ti crystals, are able to describe with a reasonable accuracy nanoscale systems consisting of several tens of atoms. A proper description of such nanoscale systems is important in the case of nanostructured or non-ideal materials. Contrary to ideal crystalline structures, real crystals also have point defects and local irregularities of the structure such as dislocations, grain boundaries, or stacking faults. The results obtained by the classical optimization of atomic clusters correlate with those, which were obtained on the basis of more accurate DFT calculations. For the very small clusters consisting of

a few atoms, the relative discrepancy between the obtained results is higher since the finite-size quantum effects, which are not accounted for within the classical approach, are crucial for these systems. Although having been applied in this study only to Ti-Ni interatomic potentials, this methodology can also be used for the exploration of many more materials of technological interest, including monatomic systems and alloys.

3.2 Reconciling simulated melting and ground-state properties of metals with a modified many-body potential

Different many-body potentials [76, 77, 122–124], that have a general form defined by expressions (2.22) or (2.23), are capable of describing geometrical, mechanical, and energetic properties of different metals (e.g., cohesive energy, lattice parameters, and elastic constants), but can rarely reproduce the experimentally measured melting temperature. An illustrative case study is bulk gold whose melting temperature, as calculated using the many-body potentials which account for the interaction of a given atom with several surrounding atomic layers, differ from experimental values by several hundred degrees [125, 126]. A similar order of discrepancy was observed also for other metals, e.g. titanium [127, 128], and also for inorganic systems, such as silicon [126]. Thus, it is essential to amend the existing force fields, so that they can reproduce correctly properties of both the ground- and finite-temperature states of metal systems.

In this work, we have proposed a recipe for constructing an interatomic potential that is able to correctly reproduce both the melting temperature and the ground-state properties of metal systems by means of classical MD simulations [21]. The new potential should satisfy the following principal condition: curvature of the modified potential energy profile in the vicinity of the equilibrium point must coincide with that of the original potential. This condition is set to reproduce, with the new potential, ground-state properties which are governed by the behavior of the potential energy curve in the vicinity of the equilibrium point.

There are different functional forms that satisfy this mathematical condition. As an illustration, we have added a linear function to the existing formula, so that the modified expression for the potential energy of the system reads as:

$$U_{\text{mod}}(r_{ij}) = U(r_{ij}) + B r_{ij} + C , \quad (3.4)$$

where $U_{\text{mod}}(r_{ij})$ is the proposed modified potential, $U(r_{ij})$ is the original many-body potential in the form (2.22) or (2.23), and B and C are adjustable parameters. The

term $B r_{ij}$ makes the resulting potential steeper (less attractive) at interatomic distances exceeding the equilibrium point but, at the same time, it also slightly changes the depth of the potential well at the equilibrium point. The constant term C is thus introduced to discard the latter effect. As a case study, we used the exact form of the potential $U(r_{ij})$ which is based on the second-moment approximation of the tight-binding model. Both the attractive and repulsive terms are introduced in this approach in the exponential form, see Eqs. (2.23) and (2.24)–(2.25).

One should note that the introduced modification (3.4) is spiritually similar to the so-called Dzugutov pairwise potential [129] which was developed to model glass-forming liquid metals. The Dzugutov potential was constructed to suppress crystallization common to most monatomic systems by the introduction of a repulsive term representing the Coulomb interactions that are present in a liquid metal. The similar idea of increasing repulsion at large interatomic distances for modeling metals in highly-vibrational states far from the potential energy minimum is pursued with the introduced linear modification.

The impact of the modified potential is investigated by analyzing thermal, geometrical, and energetic properties of nanoscale samples composed of four representative metals. We consider gold and platinum, which are important metallic constituents of the nanosystems currently proposed for radiotherapy applications, as well as titanium and magnesium, which are of interest for the development of biocompatible implants for medical applications. A generality of the introduced correction is emphasized by considering metals with different characteristics of the electron structure, namely (i) s, p -bonding (Mg), (ii) transition metal with less than half-filled d band (Ti), (iii) transition metal with almost filled d band (Pt), and (iv) noble metal with completely filled d band (Au).

We have considered finite-size spherical nanoparticles with radii from 1 to 7 nm, cut from ideal face-centered cubic (fcc) (in the case of Au and Pt) or hexagonal close-packed (hcp) (for Ti and Mg) crystals. The nanoparticles were composed of approximately 300 to 80,000 atoms. The crystalline structures were constructed and optimized, and the MD simulations were carried out using the MBN Explorer software package [61]. Energy minimization was performed using the velocity-quenching algorithm.

The MD simulations of the nanoparticle heating/melting were performed without boundary conditions in the NVT canonical ensemble. The temperature T was controlled by a Langevin thermostat with a damping coefficient $\gamma = 1 \text{ ps}^{-1}$. In Langevin dynamics, atoms in the system are considered to be embedded in a "sea" of fictional particles. In this case, the dynamics of atoms in the system is described by Langevin equations of motion [61]. The Langevin equation of motion for an atom includes additional terms

Table 3.2: Utilized parameters of the original ((2.23), (2.24) and (2.25)) and the modified (3.4) FS-type potentials describing the interactions in gold, platinum, titanium, and magnesium

	d (Å)	A (eV)	p	ξ (eV)	q	Ref.	B (eV/Å)	C (eV)	r_c (Å)
Au	2.88	0.206	10.23	1.79	4.04	[123]	0.0065	-0.034	6.65
Pt	2.78	0.297	10.61	2.70	4.00	[123]	0.0064	-0.031	6.6
Ti	2.95	0.153	9.25	1.88	2.51	[108]	0.0114	-0.060	7.0
Mg	3.21	0.029	12.82	0.50	2.26	[123]	0.0061	-0.032	7.0

that account for the friction force and the noise terms and reads as:

$$m_i \mathbf{a}_i(t) = \mathbf{F}_i(t) - \frac{1}{\tau_d} m_i \mathbf{v}_i(t) + \sqrt{\frac{2k_B T_0 m_i}{\tau_d}} \mathbf{R}_i(t). \quad (3.5)$$

Here, \mathbf{F}_i is the physical force acting on the atom, $k_B T$ denotes the thermal energy in the system with k_B being the Boltzmann constant, $\tau_d = 1/\gamma$ is the characteristic viscous damping time, and $\mathbf{R}_i(t)$ represents a delta-correlated stationary Gaussian process with zero-mean, satisfying

$$\langle \mathbf{R}_i(t) \rangle = 0 \quad (3.6)$$

$$\langle \mathbf{R}_i(t) \mathbf{R}_i(t') \rangle = \delta(t - t'), \quad (3.7)$$

where $\langle \dots \rangle$ denotes time-averaging. The viscous damping time parameter, τ_d , describes the characteristic time of energy exchange between particles and the heat bath. The Langevin equation of motion (3.5) gives a physically correct description of a many-particle system interacting with a heat bath, maintained at a constant temperature T_0 [61].

In the performed simulations, the nanoparticles were heated up with a constant rate of 0.5 K/ps. The time integration of the equations of motion was done using the velocity-Verlet algorithm [130] with an integration time step of 5 fs. In all the calculations, the interatomic interactions were truncated at the cutoff radius r_c which was introduced to reduce the computation time. Depending on the system, the utilized cutoff value was in the range between 6.6 and 7 Å. Parameter B was derived independently for each considered metal so that the extrapolated bulk melting point corresponds to the reference value. The parameter C was then tuned to reproduce the reference value of cohesive energy. Parameters of the original FS-type potential (Eqs. (2.23), (2.24) and (2.25)) and its modification (3.4) are summarized in Table 3.2.

In the proposed modification, the linear term $B r_{ij} + C$ is responsible for a monotonic increase of the potential at large distances. In this case the cutoff distance is set to the value at which the modified potential (3.4) is equal to zero. The parametrization of the original EAM-type potential for titanium, given in Table 3.2, was obtained in

Table 3.3: Comparison of ground-state parameters of the modeled crystals for different specifications of the potential

	U	U_{mod}	exp.	U	U_{mod}	exp.
	Au			Pt		
a , Å	4.07	4.05	4.08	3.93	3.91	3.92
E_{coh} , eV	3.78	3.80	3.78	5.85	5.84	5.85
	Ti			Mg		
a , Å	2.92	2.92	2.95	3.20	3.20	3.21
c , Å	4.76	4.76	4.68	5.22	5.22	5.21
E_{coh} , eV	5.04	4.85	4.87	1.52	1.49	1.52

Ref. [108] with the cutoff distance of 4.2 Å as another adjustable parameter. The other three metals are described in this work with the parametrization by Cleri and Rosato [123] where the summation in the EAM-type potential was ”.. extended up to the fifth neighbors for cubic structures”. The analysis of radial pair distribution function for gold and platinum demonstrates that the fifth neighbors in these metals are located at the distance 6.45 and 6.15 Å from the given atom, respectively. These values are slightly smaller than the cutoff values which have been used in the present simulations, see Table 3.2. In Ref. [123], hcp metals were described ”... with cutoff values ranging between $\sqrt{11/3}d$ and $\sqrt{5}d$ ” where d is the first-neighbor distance. The original cutoff for titanium, as formulated in Ref. [123], thus lies in the range from 5.65 to 6.60 Å which is smaller than the cutoff used in our simulations. Similarly, the original cutoff for magnesium lies in the range between 6.15 and 7.2 Å and corresponds to the value of $r_c = 7$ Å which we have adopted in the simulations.

To quantify the effect due to the potential modification, we have analyzed first the ground-state geometrical and energetic properties of the samples, namely lattice parameters and cohesive energy (see Table 3.3). The quantity E_{coh} represents the cohesive energy per atom of an infinitely large ideal crystal, which was obtained by extrapolating the binding energies of Au_N , Pt_N , Ti_N , and Mg_N ($N \approx 300 - 80,000$) nanoparticles to the $N \rightarrow \infty$ limit. Table 3.3 demonstrates that, similar to the case of the original potential (the column labeled as ” U ”), the modification of the potential (the column ” U_{mod} ”) allows one to reproduce experimental values [117] with a relative discrepancy of less than 2%.

As another benchmark of the modified potential, vacancy formation energy was analyzed. This quantity is given by

$$E_{\text{vf}} = E_{N-1} - \frac{N-1}{N} E_N . \quad (3.8)$$

where E_N and E_{N-1} are the energies of a perfect crystal and a vacancy-formed structure

after relaxation, and N is the number of atoms in the simulation box. To calculate E_{vf} , the following procedure was adopted. A perfect crystal was created, which spans at least three cutoff distances in each direction. The crystal comprising N atoms was relaxed using periodic boundary conditions. Then, one atom was removed from the crystal. The crystal now comprising $N - 1$ atoms was relaxed again using periodic boundary conditions. To check the consistency of the results, we have analyzed the samples of different size, containing from about 500 up to 2048 atoms.

Table 3.4 presents the vacancy formation energy calculated with the original (the column " U_{orig} ") and the modified (the column " U_{mod} ") potentials. The calculated values are compared with available experimental data and the results of earlier DFT and classical calculations. This analysis demonstrates that the numbers obtained with the original EAM-type potential (2.23)-(2.25) and its modification (3.4) are consistent with one another and agree in general with the existing experimental and theoretical values.

Table 3.4: Vacancy formation energy (in eV) calculated with the original (U_{orig}) and the modified (U_{mod}) potential. The calculated values are compared with available experimental data and the results of earlier calculations. The experimental methods comprise positron annihilation (PA), thermal expansion (TE) and quenching (Q) measurements. Earlier theoretical calculations performed by means of density functional theory are labeled as DFT. EAM denotes the classical MD simulations performed using an EAM-type potential.

	this work		exp. data	calculations
	U_{orig}	U_{mod}		
Ti	1.56	1.52	1.55 [131] 1.27 ± 0.05 (PA) [132]	1.56 (EAM) [108] 2.14 (DFT-LDA) [133] 1.97 (DFT-GGA) [134]
Mg	0.60	0.62	0.58 ± 0.01 (TE) [135] 0.79 ± 0.03 (Q) [137]	0.88 (EAM) [136] 0.77 – 0.80 (DFT-GGA) [138]
Au	0.61	0.64	0.62 – 0.67 (TE) [139] 0.70 – 1.10 (Q) [139]	0.60 (EAM) [122] 0.75 (EAM) [123]
Pt	1.16	1.14	1.35 ± 0.09 (PA) [140]	1.28 (EAM) [122] 1.15 (DFT-LDA) [141] 1.18 (DFT-GGA) [141]

Melting temperature of the finite-size nanoparticles was estimated from analyzing the temperature dependence of the heat capacity, $C_V = (\partial E / \partial T)_V$, defined as a derivative of the internal energy of the system with respect to temperature. A typical caloric curve, that is the temperature dependence of the time-averaged total energy $\langle E_{\text{tot}} \rangle$ of the nanoparticle, and the heat capacity C_V are shown in Figure 3.5. A sharp maximum of C_V is attributed to the nanoparticle melting.

The bulk melting temperature was estimated by extrapolating the obtained values

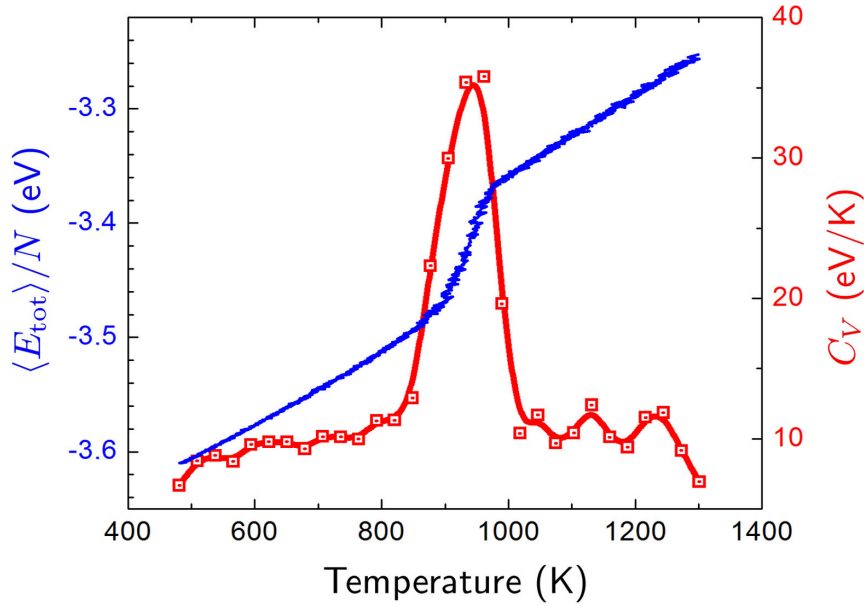


Figure 3.5: Temperature dependence of (i) the time-averaged total energy per atom $\langle E_{\text{tot}} \rangle / N$ of a 5 nm-radius gold nanoparticle, composed of $N \approx 31,000$ atoms (blue curve), and of (ii) the heat capacity C_V (red curve and symbols). A sharp maximum of the heat capacity at $T = 945$ K arises at the nanoparticle melting temperature.

to the $N \rightarrow \infty$ limit according to the Pawlow law [63, 142, 143]. It describes the dependence of the melting temperature of spherical particles on the number of atoms they are composed of as $T_m = T_m^{\text{bulk}} - \alpha N^{-1/3}$, where T_m^{bulk} is the melting temperature of a bulk material and α is the factor of proportionality. Thus evaluated values of melting temperature are summarized in Figure 3.6 and Table 3.5 for all the studied metals.

In Figure 3.6, symbols illustrate the results of the simulations for the finite-size nanoparticles. The estimated values of the bulk melting temperature obtained with the use of the original potential (2.24)-(2.25) (open symbols) lead to a significant deviation of about 300 K from the experimental values which are marked by stars. The situation changes drastically when introducing the linear correction to the original potential. The figure illustrates that the use of the modified force field (closed symbols) leads to a much better correspondence of the bulk-limit extrapolations with the experimental values for all studied metals. The extrapolation procedure yields the values of the melting temperature presented in Table 3.5 which differ from the reference values by less than a few percent.

For additional analysis, melting temperature of titanium was evaluated with the original FS-type potential using different values of the cutoff (see Figure 3.7). We have considered several values of r_c , ranging from 4.2 Å up to a significantly larger value of 14 Å. The former value slightly exceeds the second-neighbor distance in the hcp-Ti crystal, $d_2 = 4.17$ Å. In the case of a small cutoff radius (open squares / dashed

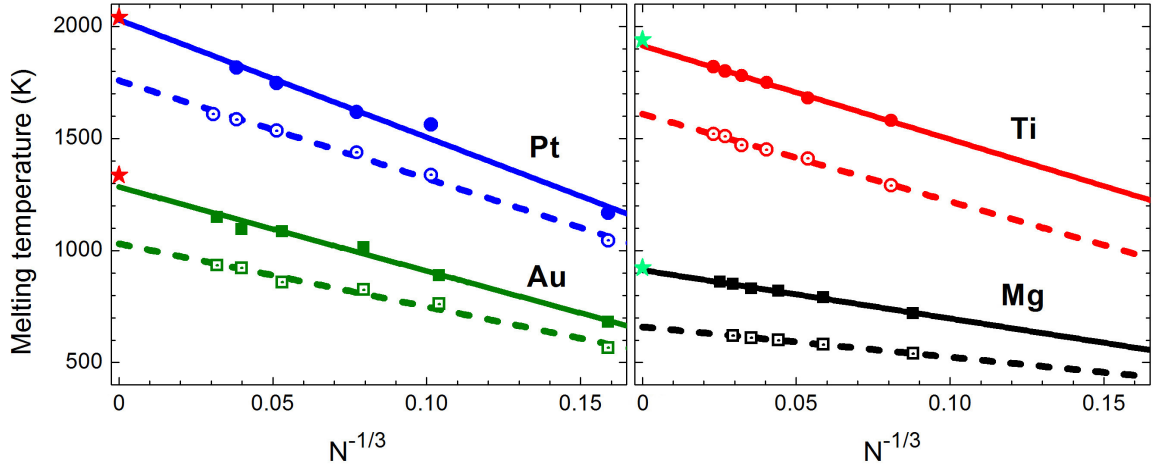


Figure 3.6: Melting temperature of spherical Au_N , Pt_N , Ti_N , and Mg_N nanoparticles calculated by means of the original, U (open symbols), and the modified, U_{mod} (closed symbols), potential. Lines represent the linear extrapolation of the calculated numbers to the bulk ($N \rightarrow \infty$) limit. Experimental values of melting temperature are shown by stars. The figure is adapted from Ref. [21].

Table 3.5: Melting temperature T_m^{bulk} (in kelvin) of different metals which is evaluated on the basis of the performed MD simulations

	U	U_{mod}	exp.
Mg	658	913	923
Au	1030	1284	1337
Ti	1610	1915	1941
Pt	1759	2030	2041

black line), the difference between the extrapolated bulk melting temperature and the reference value is as large as 500 K, while the increase of the cutoff up to 7 Å (open circles / dashed red line) reduces the gap but still yields the discrepancy of about 300 degrees. We have also tested another parametrization of the Ti-Ti force field, which was suggested in Ref. [123] (dotted grey line). The further increase of the cutoff up to a very large value of 14 Å does not quantitatively change the description of thermal properties of the system. Simulation of melting of the nanoparticles with $R = 2$ and 3 nm with the use of the increased cutoff (triangles) results in an increase of the melting temperature only by 20 K, as compared to the case of $r_c = 7$ Å. Thus, an explicit account of very distant interatomic interactions does not improve the quantitative description of melting, and the potential modification is required to bring the calculated melting temperature closer to the experimental value.

In order to understand the physical effects which are behind the above-described improvement, melting of the studied metal systems was analyzed in terms of the Lindemann criterion [144]. It states that melting occurs because of vibrational instability,

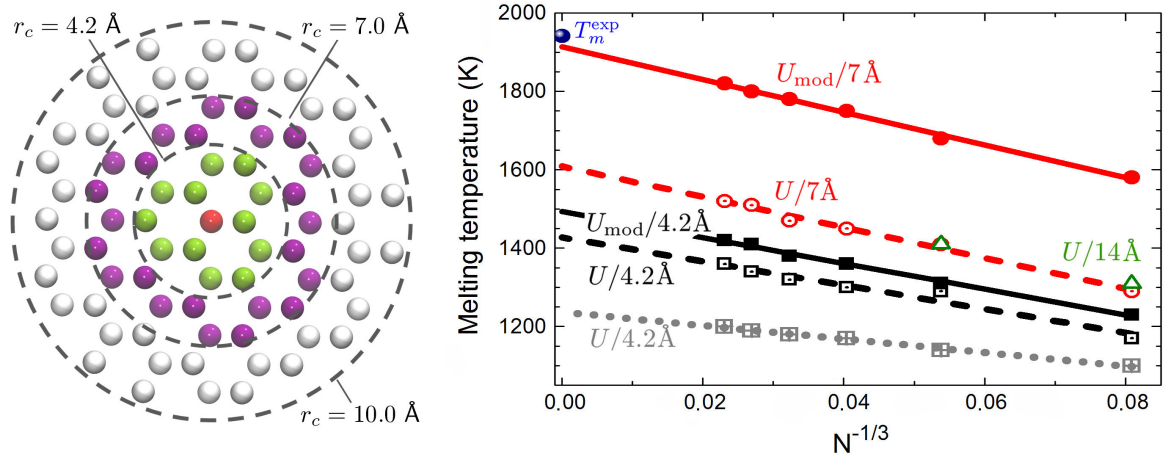


Figure 3.7: Left panel: Crystalline structure of hcp-Ti. Concentric circles show different cutoff radii with respect to the central atom, marked by red color. Right panel: Melting temperature of spherical titanium nanoparticles (symbols) calculated by means of the original U and modified U_{mod} potential using different values of the cutoff radius, as indicated.

i.e. a crystalline structure melts when the average amplitude of thermal vibrations of atoms is relatively high compared to interatomic distances. This condition can be expressed as $\sqrt{\langle(\delta u)^2\rangle} > \delta_L d$, where δu is the atomic displacement, δ_L is the Lindemann parameter typically equal to 0.10 – 0.15, and d is the interatomic distance [101].

The analysis revealed that interatomic interactions at distances, exceeding the equilibrium distance by a characteristic vibration amplitude defined by the Lindemann criterion, significantly affect the correctness of simulations. To elaborate on this issue, we analyzed the potential energy surfaces (PES) for large 6 nm-radius nanoparticles with the optimized structure, composed of the titanium, gold, and magnesium. Positions of all atoms in the systems except for a given one were fixed. The movable atom was displaced from its equilibrium position and the interaction energy was calculated. Then, the energy of the perturbed system was subtracted from the energy of the fully optimized system. The resulting PES for the metal nanoparticles are presented in Figure 3.8. Each panel shows several isolines corresponding to a given energy difference between the optimized and the perturbed systems. For the sake of clarity, this quantity has been converted into temperature.

Due to the additional linear term, the modified many-body potential (solid curves) makes the resulting potential steeper at large interatomic distances, as compared to the original FS-type potential (dashed curves). For instance, in the case of titanium, the displacement of an atom for about 0.3 \AA , that is approximately 1/10 of the closest interatomic distance ($d_{\text{Ti}} = 2.95 \text{ \AA}$), results in the energy difference of about 0.17 eV that corresponds to 2000 K. Thus, interatomic interactions at distances, exceeding the equilibrium distance by a characteristic vibration amplitude δu , are overestimated

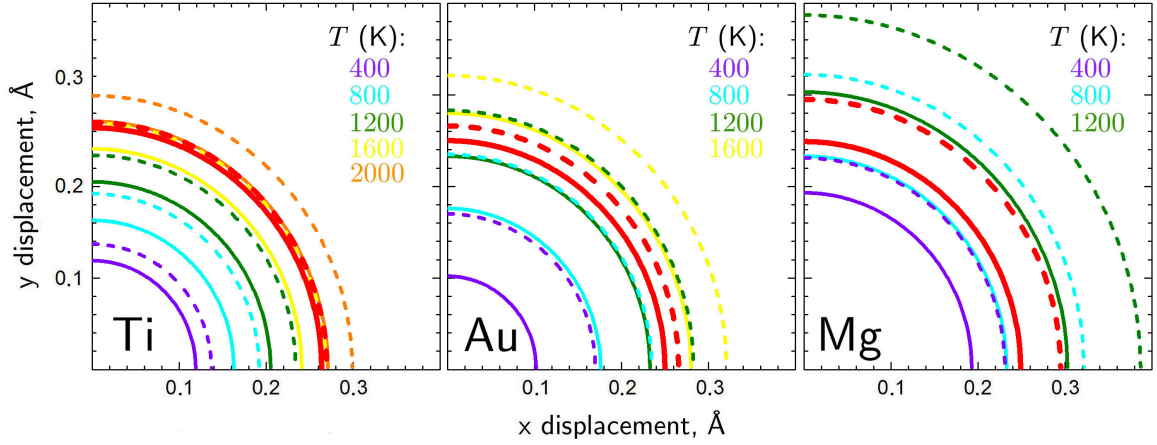


Figure 3.8: Potential energy surface for 6 nm-radius metal nanoparticles whose constituent atoms interact via the original (dashed lines) or the modified (solid lines) potentials. The thick dashed and solid (red) lines denote the energy difference corresponding to the predicted bulk melting temperatures (see Table 3.5). The figure is adapted from Ref. [21].

by conventional many-body potentials and should be corrected in order to reproduce the quantitatively correct value of the melting point. A more accurate description of the interatomic interaction in the region beyond the equilibrium distance allows one to handle the problem of the accurate description of thermo-mechanical properties of metal materials.

Chapter 4

Low-energy electron production by metal nanoparticles

This chapter presents the results of a theoretical and numerical analysis of electronic properties of nanometer-size nanoparticles made of gold, platinum, silver, and gadolinium. This study was motivated by the fact that nanoparticles composed of these materials are of current interest for radiation therapy applications. Metal nanoparticles were proposed recently to act as radiosensitizers in cancer treatments with ionizing radiation [8–12, 41, 145]. It is currently suggested that, being delivered to the tumor region, such nanoparticles can boost the production of secondary electrons near the target [16, 17]. Therefore, the use of radiosensitizing nanoparticles can result in a well-localized dose enhancement that will lead to the enhanced radiation damage of the tumor cells thus increasing efficiency of the treatment.

After the first experimental evidence of radiosensitization by gold nanoparticles [42] a number of follow-up experiments with nanoparticles composed of other metals, such as platinum, silver, gadolinium and iron, were performed in recent years [8–10, 43, 146, 147]. Application of gold nanoparticles in combination with photons demonstrated an increase of cancer cell killing [11, 42, 148]. In recent experimental studies with fast ions as a radiation source the radiosensitizing effect done by metal nanoparticles was also observed [8, 10, 149]. This opens a possibility for using nanoparticles in ion-beam cancer therapy which is currently considered as a very promising modern treatment technique [13, 150, 151].

In this chapter, we focus attention on electron production by sensitizing nanoparticles irradiated by photons and fast ions. We provide a methodology for analyzing the dynamic response of nanoparticles of the experimentally relevant sizes, namely of about several nanometers, exposed to ionizing radiation. Because of a large number of constituent atoms (about $10^3 - 10^4$ atoms) and consequently high computational costs, the electronic properties of such systems can hardly be described by means of *ab ini-*

tio methods based on a quantum-mechanical treatment of electrons, and this analysis should rely on model approaches. By comparing the response of smaller systems (of about 1 nm size) calculated within the *ab initio*- and the model framework, we validate this methodology and make predictions for the electron production in larger systems.

The atomic system of units, $m_e = |e| = \hbar = 1$, is used throughout this chapter.

4.1 Collective electron excitations in gold clusters under photon impact

It is well known that an important mechanism of excitation/ionization of metallic clusters and nanoparticles, as well as some other nanoscale systems, relies on the formation of plasmons, that is, collective excitations of delocalized valence electrons induced by an external electric field [20, 36, 152]. Plasmon excitations correspond to oscillations of the electron density with respect to the positively charged ions and are described in the classical physics terms [19, 80]. These excitations appear as prominent resonances in the excitation/ionization spectra of various systems, and the position of the resonance peak depends strongly on the type of a system (see Figure 4.1, panels (a) and (b)). In the case of metallic clusters, a typical energy of the plasmon excitations is about several electronvolts, and the resonance peak is located in the vicinity of the ionization threshold [153, 154].

Another important ionization mechanism is associated with the collective excitation of electrons localized on individual atoms. Such excitations appear in the electronic shells which have a large number of highly-correlated electrons, for instance, in the *d* shells. These excitations are associated with a short-range potential well due to screening effects and a centrifugal barrier for electrons with large angular momentum, and result in the formation of the so-called atomic giant resonances in the ionization spectra of many-electron atoms [155, 156] (see Figure 4.1, panels (c) and (d)). The resonances appear as broad peaks positioned above the ionization threshold of a given shell.

All these collective electron phenomena occur in various processes of interaction of ionizing radiation with matter. In particular, dipole collective excitations result in the formation of prominent resonances in the photoabsorption spectra of atomic clusters and nanoparticles [36, 152], while the impact ionization cross sections comprise also the contributions of higher multipole terms [20].

In this work, the contribution of the plasmon excitations is evaluated by means of the so-called Plasmon Resonance Approximation (PRA) [19, 20, 159]. This approach postulates that the dominating contribution to the cross section in the vicinity of the

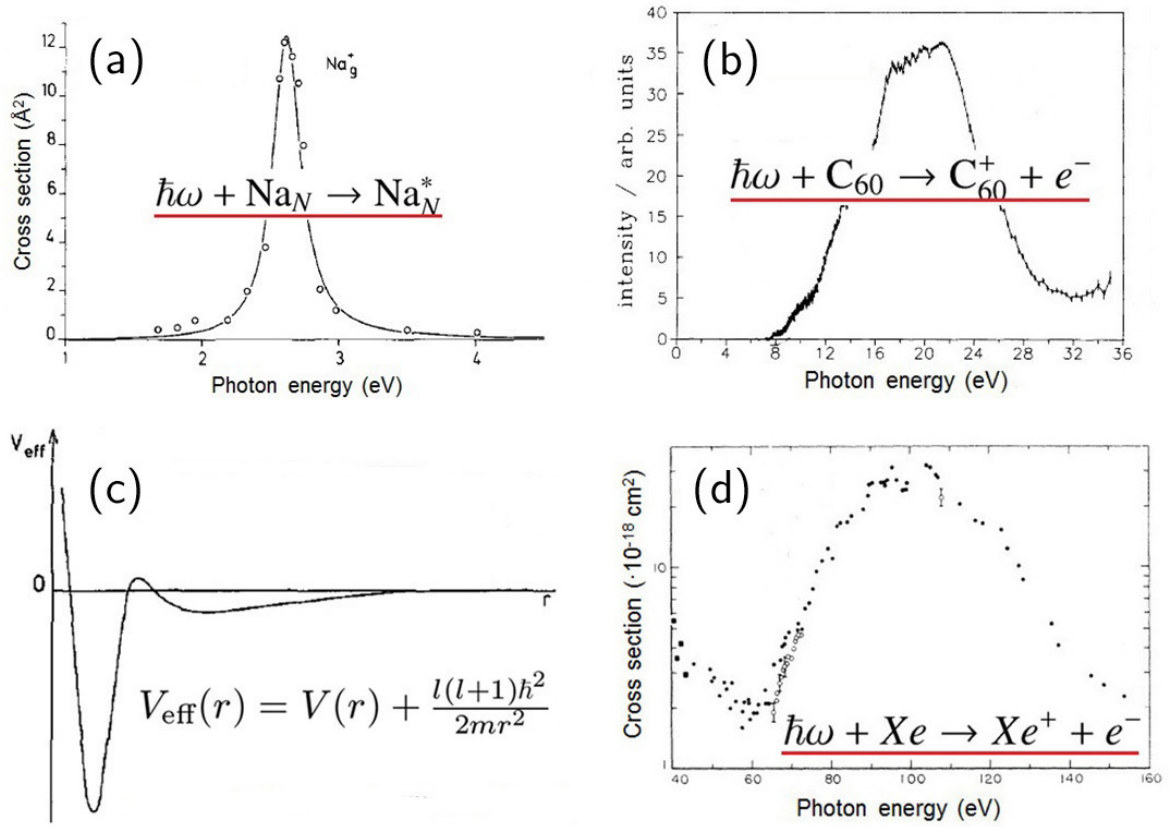


Figure 4.1: Plasmon resonance peaks in the photoabsorption spectra of a small sodium cluster (a) and a C_{60} fullerene (b). In the case of metallic clusters, a typical energy of the plasmon excitations is about several eV, while in the case of fullerenes the plasmon peak represents a broad feature positioned at about 20 eV. The formation of atomic giant resonances in individual atoms is associated with a short-range potential well formed due to screened Coulomb interaction and a centrifugal barrier for electrons with large angular momentum (c). These resonances appear as broad peaks positioned above the ionization threshold of a given shell (d). The figures are adapted from Refs. [153, 156–158].

plasmon resonance comes from collective electron excitations, while single-particle effects give much smaller contribution [160,161]. During the past decades, this approach provided a clear physical explanation of the resonant-like structures in photoionization spectra [19, 29] and differential inelastic scattering cross sections [18, 27, 28, 161–163] of metal clusters and carbon fullerenes under the photon and electron impact. This approach is briefly described in this chapter and also outlined in Appendix A.

The PRA relies on a few parameters, which include the oscillator strength of the plasmon excitation, position of the plasmon resonance peak and its width. The choice of these parameters can be justified by comparing the model-based spectra either with experimental data or with the results of more advanced calculations. References [16,17] provided an experimental evidence that a considerable portion of radiosensitization by gold nanoparticles arises from the emitted low-energy electrons. However, it is hardly

possible to find experimentally measured impact ionization cross sections of gold clusters and nanoparticles with photons and charged projectiles covering the photon energy (or energy loss range) of about 1 – 10 eV. In order to get this information, photoionization spectra of several gold clusters were calculated in this study by means of TDDFT. Then, the *ab initio*-based spectra were fitted with those calculated within the model approach. Such a methodology allowed us to define the resonance frequencies and to calculate the oscillator strength of the plasmon excitations in gold nanoparticles.

We begin with the analysis of TDDFT-based ionization spectra of small systems. As a case study, four three-dimensional gold clusters consisting of 18 to 42 atoms, namely Au₁₈, Au₂₀, Au₃₂, and Au₄₂, have been considered. The former two systems, which were observed experimentally, possess C_{2v} and T_d symmetry, respectively [164, 165]. The latter two are hollow, fullerene-like icosahedral structures whose high stability was predicted theoretically on the basis of DFT calculations [166–168].

The TDDFT-based photoabsorption spectra were calculated as follows. At first, we performed the geometry optimization using the Gaussian 09 package [107]. The optimization procedure was performed by means of DFT within the generalized gradient approximation (GGA) and using the effective-core potential CEP-121G basis set [169], augmented by *d*-polarization functions. The utilized basis set has the *4f* frozen core, so that 19 electrons (*5s*, *5p*, *5d*, and *6s*) from each gold atom were explicitly treated in the course of optimization. The main principles, the performed calculations are based on, as well as the corresponding definitions are outlined in Appendix B.

To account for the exchange and correlation corrections, the PBE functional [85] was utilized. Different spin multiplicities were considered in the course of geometry optimization. Figure 4.2 shows the ground-state geometries of the studied clusters.

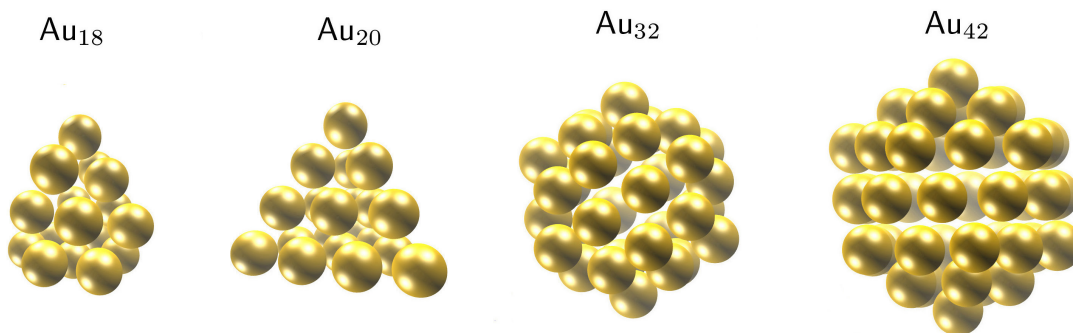


Figure 4.2: Optimized structures of the studied gold clusters. The figure is adapted from Ref. [24].

The linear response function of the clusters was calculated within the dipole approximation, based on the formalism described in Section 2.4. The photoabsorption spectra were obtained using the TDDFPT module [170] of the Quantum Espresso software pack-

age [171]. The optimized geometries were introduced into a supercell of $20 \times 20 \times 20 \text{ \AA}^3$. Then, the system of Kohn-Sham equations was solved self-consistently for valence electrons of the clusters to calculate the ground-state eigenvalues using a plane-wave approach [171]. The calculations were performed using a Vanderbilt ultrasoft nonlinear core-corrected pseudopotential [172], which substitutes real valence atomic orbitals in the core region with smooth nodeless pseudo-orbitals [94]. For that, eleven outer-shell electrons ($5d^{10}6s^1$) of each gold atom were treated as the valence ones. The obtained results were checked by performing a series of calculations with different values of the supercell size and the energy cutoff. The spectra presented below were obtained with the kinetic energy cutoff of 30 Ry for the wave functions and 180 Ry for the electron densities.

It should be stressed that, although the size of the studied clusters is not so large (about 1 nm in diameter), the largest considered cluster, Au_{42} , contains 462 outer-shell electrons which should be simultaneously accounted for in the DFT/TDDFT calculations. This makes the *ab initio*-based calculation of the spectra quite demanding from the computational viewpoint. To analyze the dynamic response of the systems, which are currently used in the experimental studies on sensitization [8–10, 146], one should therefore utilize model approaches. They should also describe adequately the response of smaller systems and must be validated by comparing the results of the *ab initio*- and model-based calculations.

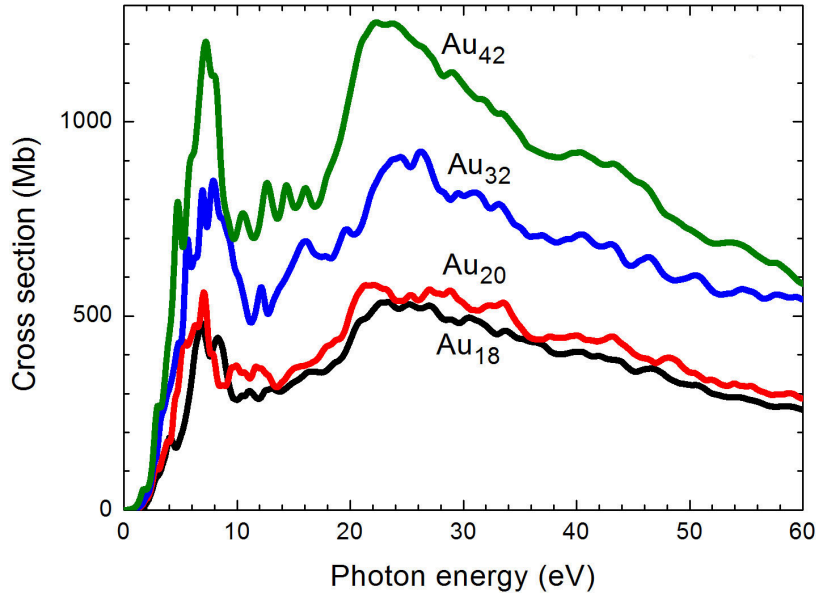


Figure 4.3: The photoabsorption cross section of the Au_{18} (black), Au_{20} (red), Au_{32} (blue) and Au_{42} (green) clusters calculated within the TDDFT framework. The figure is adapted from Ref. [24].

Figure 4.3 shows the photoabsorption spectra of the Au_{18} , Au_{20} , Au_{32} and Au_{42}

clusters calculated by means of TDDFT for the photon energy up to 60 eV. The spectra, having a similar profile, are characterized by a low-energy peak located below 10 eV and by a broad feature which has the maximum at about 20 – 25 eV.

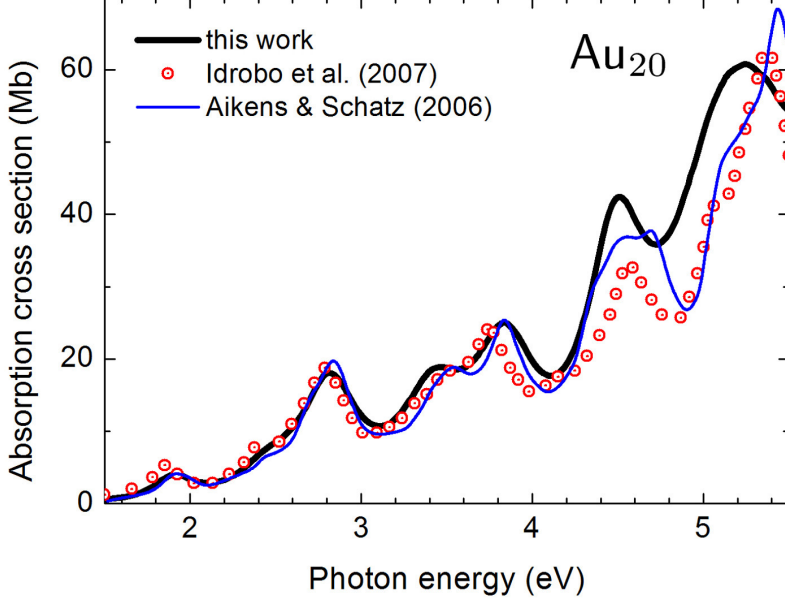


Figure 4.4: Comparison of the photoabsorption cross section for Au_{20} calculated in this work (thick black line) with the spectra from previous studies by Idrobo *et al.* [173] (symbols) and Aikens and Schatz [174] (thin blue line). The spectrum obtained in this work is given in Mb. The spectra from other studies were provided in arbitrary units; for a quantitative comparison they were normalized to the present spectrum at the point of maximum of the peak at 2.8 eV.

As a benchmark of the utilized approach, we have compared the photoabsorption spectrum for Au_{20} calculated in this work with the spectra obtained in earlier studies [173, 174]. This comparison is presented in Figure 4.4. It demonstrates that the spectra are in good mutual agreement thus confirming the accuracy of the present calculations. Minor discrepancies can be attributed to different exchange-correlation functionals used in this work (GGA-PBE) and in earlier studies (GGA-PB86 [174] and LDA [173]).

The analysis performed in this study revealed that the broad feature in the spectra of gold clusters, having the maximum at about 20 – 25 eV, is the giant resonance formed due to the excitation of electrons in the $5d$ atomic shell. To prove this, we have analyzed the oscillator strength distribution, $df/d\omega$, which is proportional to the photoabsorption cross section,

$$\sigma_{\gamma}(\omega) = \frac{2\pi^2}{c} \frac{df}{d\omega}. \quad (4.1)$$

Integration of this expression leads to the oscillator strength f in the photon energy

range from ω_1 to ω_2 :

$$f = \int_{\omega_1}^{\omega_2} \frac{df}{d\omega} d\omega = \frac{c}{2\pi^2} \int_{\omega_1}^{\omega_2} \sigma_\gamma(\omega) d\omega . \quad (4.2)$$

The total oscillator strength, including both excitations in the discrete and in the continuum spectrum, should be equal to the total number of electrons in the system:

$$f_{\text{total}} = \int_0^\infty \frac{df}{d\omega} d\omega = N_e . \quad (4.3)$$

The spectra presented in Figure 4.3 were integrated in the photon energy range from 20.2 eV (ionization threshold of the 5*d* shell in a single atom of gold) up to 57.2 eV, which is the ionization threshold of the 5*p* shell [175]. The obtained values are 139.8, 153.3, 240.5 and 318.7 for Au₁₈, Au₂₀, Au₃₂ and Au₄₂, respectively. This indicates that about eight atomic *d*-electrons contribute to the excitation of the 5*d* shell forming the broad resonance peak in the photoionization spectra. The 5*d* giant resonance can be fitted with a Fano resonance profile [176],

$$\sigma_{5d}(\omega) \equiv \sigma_{5d \rightarrow \varepsilon p, \varepsilon f}(\omega) \propto \frac{(\Gamma_{5d} + \omega - \omega_{5d})^2}{(\Gamma_{5d}/2)^2 + (\omega - \omega_{5d})^2} , \quad (4.4)$$

which is frequently utilized in atomic, nuclear and condensed matter physics to describe resonant scattering processes occurring in various systems. Here, ω_{5d} stands for the resonance frequency and Γ_{5d} is the width of the peak. To describe this feature, the values $\omega_{5d} = 22$ eV and $\Gamma_{5d} = 12$ eV were utilized. The fitting for the Au₃₂ cluster is illustrated in Figure 4.5 by the thick solid purple line.

The low-energy peak is related to the surface plasmon, which arises due to collective excitation of delocalized electrons in a whole cluster. The integration of the oscillator strength in this energy region reveals that about 1.0 (in Au₂₀) to 1.5 (in Au₃₂) electrons from each atom contribute to the plasmon. Integration of the photoabsorption spectrum of Au₃₂ up to 11.2 eV (energy at which the first dip after the resonance peak is observed) yields the oscillator strength of 1.43 per atom. The collective nature of the low-energy peak is analyzed in more detail in Section 4.1.1.

The low-energy peak was fitted by means of the PRA scheme. To describe plasmon excitations arising in gold nanoparticles, we have adopted a simple but physically grounded model which treats the studied highly-symmetric clusters, Au₃₂ and Au₄₂, as a spherical "jellium" shell of a finite width, $\Delta R = R_2 - R_1$. In other words, the electron density in these systems is assumed to be homogeneously distributed over the shell with the thickness ΔR . Such a "jellium"-shell representation has been also utilized

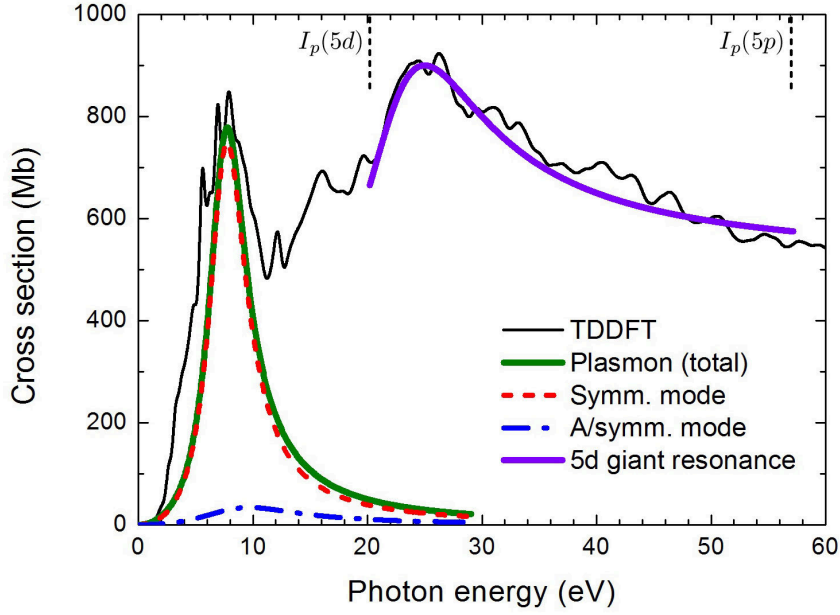


Figure 4.5: Photoabsorption cross section of Au_{32} calculated within the TDDFT method (thin black curve). Thick green curve denotes the contribution of the plasmon excitations calculated within the PRA. Red (dashed) and blue (dash-dotted) curves show the contribution of the symmetric and antisymmetric plasmon modes, respectively. Thick purple line illustrates the fit of the 5d giant atomic resonance by a Fano-type profile. Black vertical marks denote the ionization potentials of the 5d and 5p atomic shells. The figure is adapted from Ref. [24].

Table 4.1: Values of R_1 and R_2 used to model the electron density distribution in hollow Au_{32} and Au_{42} clusters

	R_1 (Å)	R_2 (Å)
Au_{32}	3.99	4.53
Au_{42}	4.60	5.25

successfully for the description of plasmon formation in fullerenes, see Chapter 5 and Refs. [27, 29, 177–179]. Values of ΔR were defined from the analysis of the ground-state geometries of Au_{32} and Au_{42} . This analysis revealed that the atoms are located on two concentric spheres of the radii R_1 and R_2 (see Table 4.1).

Within the PRA, the dynamic polarizability $\alpha(\omega)$ has a resonance behavior in the region of frequencies where collective electron modes in a many-electron system are excited (see Eq. (A27) in Appendix A). Thus, the photoionization cross section $\sigma_\gamma(\omega)$ of a spherically symmetric system can be written as:

$$\sigma_\gamma(\omega) = \frac{4\pi\omega}{c} \text{Im} \alpha(\omega) \sim \frac{\omega^2 \Gamma}{(\omega^2 - \omega_r^2)^2 + \omega^2 \Gamma^2}, \quad (4.5)$$

where ω is the photon energy, ω_r the plasmon resonance frequency, and Γ its width.

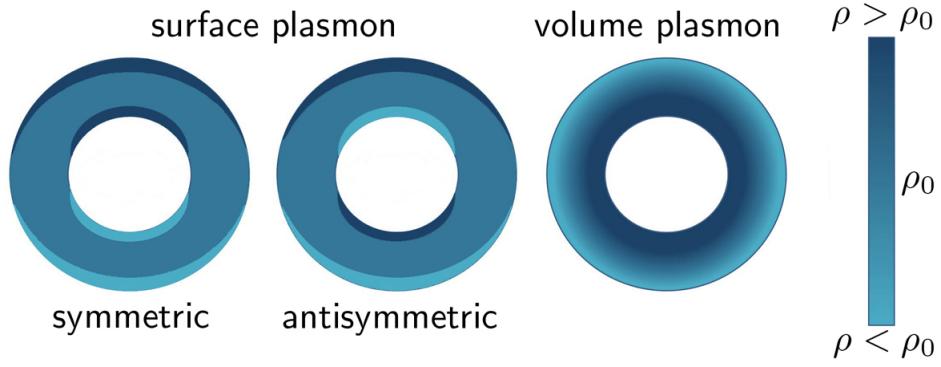


Figure 4.6: Schematic representation of the two modes of the surface plasmon (left and middle panels) and of the volume plasmon (right panel). Light-blue and dark-blue regions represent the additional positive and negative charge, respectively. The figure is adapted from Ref. [181].

The interaction of a hollow system with the uniform external field, $\mathbf{E}(\omega)$, leads to the variation of the electron density occurring on the inner and outer surfaces of the hull. As described in detail in Appendix A, this variation leads to the formation of the surface plasmon, which has two normal modes, the symmetric and antisymmetric ones. It has been argued previously [19, 159, 180] that only the surface plasmon can occur in the system interacting with a uniform external electric field, as it happens in the photoionization process. Non-uniformity of the external field causes the formation of the volume plasmon [180] which appears due to compression of the electron density inside the volume of the shell. The different plasmon modes are schematically depicted in Figure 4.6.

Thus, in the case of irradiation of hollow gold clusters by dipole photons, two surface plasmon modes, characterized by resonance frequencies $\omega_r = \omega^{(s)}$ and $\omega_r = \omega^{(a)}$ and the widths $\Gamma^{(s)}$ and $\Gamma^{(a)}$, are formed. The frequencies are defined as:

$$\omega^{(s/a)} = \left[\frac{N^{(s/a)}}{2(R_2^3 - R_1^3)} (3 \mp p) \right]^{1/2}, \quad (4.6)$$

where the signs '−' and '+' correspond to the symmetric (s) and antisymmetric (a) surface mode, respectively, $p = \sqrt{1 + 8\xi^3}$ with $\xi = R_1/R_2$ being the ratio of the inner to the outer radius. The values

$$N^{(s)} = N \frac{p+1}{2p}, \quad N^{(a)} = N \frac{p-1}{2p} \quad (4.7)$$

are the number of delocalized electrons which are involved in each plasmon mode. They obey the sum rule $N^{(s)} + N^{(a)} = N$ where N stands for a total number of delocalized electrons participating in the collective excitation.

In the case of Au_{32} , we have utilized the value $N = 46$, assuming that 1.43 electrons from each of 32 atoms are involved in the plasmon excitation. The values of $\Gamma^{(s)}$ and $\Gamma^{(a)}$ were chosen to get the best agreement of the model-based curve with the TDDFT one. In Figure 4.5, the thick solid green curve represents the total plasmon contribution to the cross section. The red and the blue curves illustrate the symmetric and antisymmetric modes, respectively. In this calculation, we have utilized the values $\Gamma^{(s)} = 4.0$ eV and $\Gamma^{(a)} = 10.5$ eV. The ratio of the widths, $\Gamma^{(s)}/\Gamma^{(a)} = 0.38$, is close to the value of 0.34, which was utilized for the description of the plasmon excitations in fullerenes (see Chapter 5) [28,29]. The *ab initio*-based spectrum reveals a more detailed structure which is formed atop the plasmon resonance. This structure represents a series of individual peaks appearing due to single-particle excitations [29] which are neglected in the model.

It should be noted that values of the plasmon width cannot be obtained directly on the basis of the utilized model. A precise calculation of the widths can be performed by analyzing the decay of the collective excitation mode into the incoherent sum of single-electron excitations. This process should be considered within the quantum-mechanical framework [161] and cannot be treated within the classical physics framework, as the PRA does. Thus, the widths of the plasmon excitations were chosen to obtain the best agreement with the results of the TDDFT calculations.

The oscillator strength for Au_{32} , calculated by means of TDDFT in the photon energy range up to the $5p$ ionization threshold ($\omega = 57.2$ eV), is equal to 338. This value agrees with the total number of valence electrons in the cluster, $N = 352$, with the relative discrepancy of about 5%. As mentioned above, it is assumed that about 1.5 and 8 electrons from each atom contribute to the surface plasmon and the $5d$ giant resonance, respectively. Thus, in this analysis we have accounted for the contribution of 9.5 from 11 valence electrons from each atom. The contribution of the rest results in a series of individual peaks, positioned in the photon energy range from 11.2 (the first dip after the low-energy peak) to 20.2 eV (the $5d$ ionization threshold), that are not accounted for in our model analysis. Integration of this part of the spectrum yields the oscillator strength of 51.5, i.e. 1.6 electrons from each atom contribute to the excitations in this energy region. The individual peaks appear due to single-particle excitations from the $s - d$ band formed due to hybridization of the $6s$ and $5d$ atomic shells.

On the basis of the performed analysis, one can state that the total photoabsorption cross section of gold clusters and nanoparticles in the energy region up to 60 eV is approximately equal to the sum of the plasmon contribution and that of the $5d$ electron excitations in individual atoms,

$$\sigma_{\gamma} \approx \sigma_{\text{pl}} + \sigma_{5d} . \quad (4.8)$$

In order to stress the different nature of the low- and high-energy features in the photoabsorption spectra of the clusters, an additional comparison with the spectrum of a smaller molecular system, a gold dimer, was performed. Figure 4.7 demonstrates the spectra of Au_{32} and Au_2 normalized to the number of atoms in each system. The spectra have a similar profile in the energy region above 15 eV. This indicates the same origin of excitations in the dimer and in larger atomic clusters, that is related to the excitation of electrons in the $5d$ shell. The ripple, which is seen at high photon energies, has an artificial origin and arises due to the method of calculation of the polarizability [170], which is obtained at complex frequencies $\omega = \omega' + i\omega''$ with an imaginary part of 0.27 eV. The real part ω' is the scanned photon energy and imaginary part ω'' corresponds to a broadening of the discrete lines due to the excited states finite lifetime [182]. The normalized spectra are compared also to the x-ray absorption data for atomic gold taken from the Henke tables [175]. From this comparison, one could state a consistency of the TDDFT-based spectra and well-established set of data.

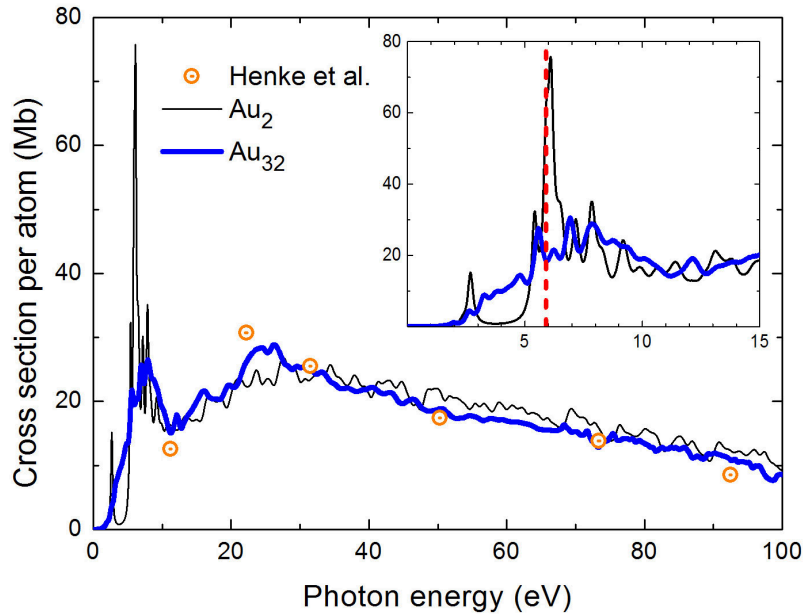


Figure 4.7: The normalized photoabsorption cross section of Au_{32} (thick blue curve) and of the Au_2 molecule (thin black curve) calculated within the TDDFT framework. Symbols represent the x-ray absorption data for atomic gold compiled by Henke *et al.* [175]. The inset shows the low-energy part of the spectra. Red vertical line illustrates the ionization threshold of a single gold atom as obtained from the DFT calculations. The figure is adapted from Ref. [24].

On the contrary, the low-energy part of the spectrum is quite different in the two considered cases. The cross section of the dimer is represented by several well-resolved narrow peaks due to particular molecular transitions, as opposed to a broader feature appeared in the spectrum of Au_{32} . The inset of Figure 4.7 shows that the low-energy

part of the spectrum of Au₂ is described by the two peaks, positioned at 2.7 and 5.4 eV, followed by the prominent peak at 6.1 eV. The latter peak corresponds to ionization of the molecule. Therefore, one can observe a clear difference in the structure of the two spectra below 10 eV, that indicates two different mechanisms of electronic excitations arising in this energy region, namely well-resolved molecular transitions in the case of Au₂ and the collective excitation of delocalized electrons in the Au₃₂ cluster. In the following section, the difference in the structure of the valence band of Au₃₂ and Au₂ is analyzed in greater detail.

4.1.1 Plasmon nature of the low-energy peak

This section provides an explanation of why the low-energy peak in the photoabsorption spectra of gold clusters can be attributed to a plasmon-type excitation.

The term "plasmon" is generally used to describe a collective excitation of delocalized electrons of a system to an external electromagnetic field. Quite commonly, it is understood in terms formulated, for example, by Fano. In his review [183] on collective phenomena in nanoscale systems and in condensed matter, it is stated that "... common to these phenomena [plasmons, superconductivity, etc., i.e. those phenomena which are based on the motion of (quasi)independent particles] is the role of a dense spectrum of states viewed initially as independent. The seemingly weak interaction among these states often condenses into a single eigenvalue separated from the rest of the spectrum by an energy gap". Thus, if a system has a dense packing of states with a small state separation, the excitation of these states may be considered as a collective, plasmon-type one.

In a number of papers [184–187], the term "surface plasmon resonance" (SPR) in relation to gold nanoparticles described a peak in the visible part of the absorption spectra (at about 2.3 eV or 540 nm). It was stated that this feature is caused by the collective excitation of 6s electrons in the gold atoms [184–187]. The corresponding electronic levels are located in the vicinity of the Fermi surface, so that these electrons delocalize over the whole nanoparticle. It was also stated [184, 185] that such a SPR (also referred to as the "localized SPR", LSPR) is a characteristic feature of relatively large systems, while the threshold nanoparticle size for emergence of such plasmonic absorption is about 1.5 – 2 nm (this value corresponds to the number of atoms in the system of about 150 – 200). Smaller gold nanoparticles (less than 1 nm in diameter) should have discrete energy levels and, thus, molecular-type transitions between the occupied and unoccupied states [186].

On the other hand, it is also well acknowledged that the occupied 6s states in the gold atoms are strongly hybridized with the 5d orbitals. A general remark on this issue

is made in Ref. [187] that "... almost always a rather strong mixing is observed, this finding reveals the "collective" nature of the electron excitation".

In Figure 4.8, the dipole oscillator strength distribution of the Au_{32} cluster is compared to that of the Au_2 molecule. The low-energy peak in the spectrum of Au_{32} corresponds to the ionization of the valence band whose structure is shown in the inset. The valence orbitals in Au_{32} span over the energy range of about 5.8 eV, so that the highest occupied molecular orbital (HOMO) and the innermost valence state have the ionization potentials of 5.77 and 11.57 eV, respectively. The $6s$ and $5d$ orbitals are hybridized and degenerated according to the cluster symmetry. Since Au_{32} is a highly-symmetric structure possessing icosahedral symmetry [166,167], its molecular orbitals are singly, triply, fourfold and fivefold degenerated in accordance with the irreducible representation of the I_h point group [188]. Analysis of the valence state separation indicates that this value varies from 0.01 to 0.64 eV, resulting in the average value of 0.13 eV. This value corresponds to those calculated [189] for a number of silver clusters Ag_N ($N = 20 \dots 120$). The emergence of a plasmon peak was observed in these systems by means of the TDDFT approach.

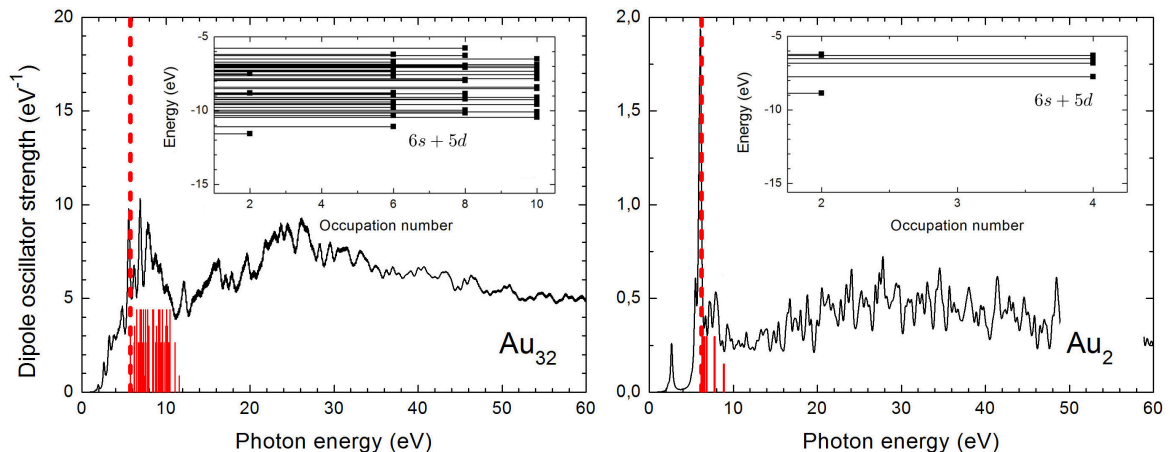


Figure 4.8: Dipole oscillator strength of the Au_{32} cluster (left) and of Au_2 dimer (right) calculated within the TDDFT framework. Vertical red lines mark ionization thresholds of each of the $6s + 5d$ valence states. Thick dashed lines denote the ionization threshold of the HOMO state in each system. Inset: Single-electron energy levels of the valence band as calculated at CEP-121G(d)/PBEPBE level of theory. The figure is adapted from Ref. [24].

Based on the analysis of the valence band structure and on the explanation given by Fano [183], the low-energy peak in the photoabsorption spectra of the gold clusters was thus associated with a collective, plasmon-type excitation. However, one should point out that this excitation involves not only the $6s$ electrons (as it happens in the case of the LSPR located at about 2.3 eV [184–187]) but also some fraction of the $5d$ electrons because of the strong overlap between the s and d states.

To the further support of this statement, this collective excitation was analyzed in terms of the classical Mie theory [190]. The Au₃₂ cluster has a hollow, fullerene-like structure [166, 167]. Geometry optimization performed in this work revealed that all atoms of the cluster are located at two concentric spheres with the radius of 3.99 and 4.53 Å (see Table 4.1). Within the classical framework, the electron density is assumed to be distributed in between these two spheres. Calculating the frequency of a surface plasmon excited in a hull-like system with the help of Eq. (4.6), one derives the value of 6.3 eV that matches well the position of the dominant feature in the TDDFT-based spectrum of Au₃₂. Thus, one can state that the low-energy peak arises due to the collective, plasmon-type excitation of electrons delocalized over the whole cluster. In this estimate, it was assumed that 46 electrons (1.43 electrons from each atom) delocalize and participate in the collective excitation. This value is in agreement with the results of Ref. [191], where the dipole polarizability of a series of three-dimensional gold clusters as a function of their size was calculated. It was found that the calculated polarizabilities suggest a delocalized character of some fraction of d electrons, so that 1.56 delocalized valence electrons contribute to the linear response to an external field.

4.2 Impact ionization of gold nanoparticles irradiated by fast ions

Investigation of the photoionization process allows one to analyze only optically allowed dipole excitations. On the contrary, energy loss studies, where a charge projectile scattered at a certain angle is detected, give access to electronic excitations of higher angular momenta. Having justified the parameters of the model that describe the dipole plasmon excitation in gold nanoparticles, the PRA approach is utilized for studying the electron production due to the plasmon excitation mechanism due to irradiation with fast ions.

4.2.1 Theoretical description of inelastic scattering on atomic clusters

In the process of inelastic scattering, the projectile undergoes the transition from the initial state $(\varepsilon_1, \mathbf{p}_1)$ to the final state $(\varepsilon_2, \mathbf{p}_2)$ which is accompanied by the ionization (or, excitation) of a target system from the initial state i with the energy ε_i to the final state f with ε_f .

The matrix element, M , which defines the amplitude of the inelastic scattering is

given by [65]:

$$\begin{aligned}
 M &= \left\langle f, 2 \left| \sum_a \frac{Z}{|\mathbf{r} - \mathbf{r}_a|} \right| 1, i \right\rangle \\
 &= \sum_a \int \psi_2^{(-)*}(\mathbf{r}) \psi_f^*(\{\mathbf{r}_a\}) \frac{Z}{|\mathbf{r} - \mathbf{r}_a|} \psi_i(\{\mathbf{r}_a\}) \psi_1^{(+)}(\mathbf{r}) \{d\mathbf{r}_a\} d\mathbf{r} , \quad (4.9)
 \end{aligned}$$

where $\{\mathbf{r}_a\} = \mathbf{r}_1 \dots \mathbf{r}_N$ are the position vectors of the delocalized electrons in the target, \mathbf{r} is the position vector of the projectile, $\psi_1^{(+)}(\mathbf{r})$ and $\psi_2^{(-)}(\mathbf{r})$ stand for the initial and the final state wave functions of the projectile, respectively, and Z is its charge. Superscripts (+) and (-) indicate that asymptotic behavior of the wave functions is "plane wave + outgoing spherical wave" and "plane wave + incoming wave", respectively [65].

The matrix element can be written as follows:

$$M = \int \frac{4\pi Z}{q^2} \frac{d\mathbf{q}}{(2\pi)^3} \langle 2 | e^{-i\mathbf{q}\cdot\mathbf{r}} | 1 \rangle \left\langle f \left| \sum_a e^{i\mathbf{q}\cdot\mathbf{r}_a} \right| i \right\rangle , \quad (4.10)$$

where $\mathbf{q} = \mathbf{p}_1 - \mathbf{p}_2$ is the transferred momentum.

In this study, we focus on the irradiation of noble metal and gadolinium nanoparticles with fast protons of 0.1 – 10 MeV incident energy. The collision velocity, $v \approx 2 - 20$ a.u., is larger than the characteristic velocity of delocalized electrons in the target, $v_e \approx 0.5$ a.u.; thus, the first Born approximation is applicable [65, 162]. Within this approximation, the initial and the final states of the incident particle can be described by plane waves:

$$\psi_1^{(+)}(\mathbf{r}) = e^{i\mathbf{p}_1\cdot\mathbf{r}} , \quad \psi_2^{(-)}(\mathbf{r}) = e^{i\mathbf{p}_2\cdot\mathbf{r}} . \quad (4.11)$$

Within the framework of the plane-wave Born approximation, the amplitude of the process reduces to

$$M = \frac{4\pi Z}{q^2} \left\langle f \left| \sum_a e^{i\mathbf{q}\cdot\mathbf{r}_a} \right| i \right\rangle_{\mathbf{q}=\mathbf{p}_1-\mathbf{p}_2} . \quad (4.12)$$

The magnitude of q^2 is related to $p_{1,2}$ and the scattering angle $\theta = \widehat{\mathbf{p}_1 \mathbf{p}_2}$ via:

$$q^2 = p_1^2 + p_2^2 - 2p_1 p_2 \cos \theta \approx p_1^2 \theta^2 . \quad (4.13)$$

The final approximate equality is valid when $p_1 \approx p_2$ and the scattering angle is small, $\theta \ll 1$ rad.

Performing the multipole expansion of the exponential factors in (4.12) (see, e.g.,

[193]), one obtains:

$$M = 4\pi \sum_{lm} i^l Y_{lm}^*(\mathbf{q}) \left\langle f \left| \sum_a \phi_l(r_a) Y_{lm}(\mathbf{r}_a) \right| i \right\rangle, \quad (4.14)$$

where the following notation is introduced:

$$\phi_l(r) = 4\pi Z \frac{j_l(qr)}{q^2} \quad (4.15)$$

and j_l is a spherical Bessel function.

Consider a general expression for the cross section of the scattering process [65]:

$$d\sigma = \frac{2\pi}{p_1} \delta(\omega_{fi} - \omega) \sum_{\text{pol}_f} \overline{\sum_{\text{pol}_i}} |M|^2 \frac{d\mathbf{p}_2}{(2\pi)^3} d\rho_f, \quad (4.16)$$

where $\omega = \varepsilon_1 - \varepsilon_2$ is the energy transfer, $\omega_{fi} = \varepsilon_f - \varepsilon_i$ and $\omega = \omega_{fi}$ due to the energy conservation law. The sign \sum_{pol_f} denotes the summation over the projection of the final state f orbital momentum, whereas $\overline{\sum_{\text{pol}_i}}$ denotes the averaging over the projections of the initial state orbital momentum, and $d\rho_f$ is the density of the final states of the target.

Substituting the scattering amplitude (4.14) into equation (4.16), one derives the doubly differential cross section:

$$\frac{d^2\sigma}{d\varepsilon_2 d\Omega_{\mathbf{p}_2}} = \frac{1}{\pi} \frac{p_2}{p_1} \sum_{lm} \int \left| \left\langle f \left| \sum_a V_{lm}(\mathbf{r}_a) \right| i \right\rangle \right|_{\text{pol}}^2 \delta(\omega_{fi} - \omega) d\rho_f, \quad (4.17)$$

where

$$V_{lm}(\mathbf{r}) = \phi_l(r) Y_{lm}(\mathbf{r}) \quad (4.18)$$

is the multipolar potential of the projectile, $d\Omega_{\mathbf{p}_2}$ denotes the differentiation over the solid angle of the scattered particle, and sign $\int d\rho_f$ means the summation over the final states (which includes the summation over the discrete spectrum and the integration over the continuous spectrum).

The cross sections (4.16) and (4.17) are valid for collisions with any charge particle. For collisions with ions, the cross sections have a quadratic dependence on the projectile charge Z . For collisions with electrons or positrons, the cross sections should be thus divided by a Z^2 scaling factor due to the change of Coulomb field of the projectile.

4.2.2 Inelastic scattering cross section within the plasmon resonance approximation

According to Kubo linear response theory [95, 162], the integral on the right-hand side of equation (4.17) can be related to the electron density variation $\delta\rho_l$ (see Eq. (A37) in Appendix A), so one can perform the following substitution:

$$\int \left| \left\langle f \left| \sum_a V_{lm}(\mathbf{r}_a) \right| i \right\rangle \right|_{\text{pol}}^2 \delta(\omega_{fi} - \omega) d\rho_f \longrightarrow \frac{1}{\pi} \text{Im} \int V_{lm}^*(\mathbf{r}) \delta\rho_l(\omega, q, \mathbf{r}) d\mathbf{r} . \quad (4.19)$$

It is assumed here that the target system interacts with a weak external perturbation which causes only a small spatial inhomogeneity in the electron density distribution within the system. The function $\delta\rho_l(\omega, q, \mathbf{r})$ is a partial density variation due to the exposure of the system to the multipolar potential $V_{lm}(\mathbf{r})$. In a general case, this variation depends on the transferred energy ω , transferred momentum q , and the position vector \mathbf{r} .

Using (4.19) in (4.17), the doubly differential cross section acquires the form:

$$\frac{d^2\sigma}{d\varepsilon_2 d\Omega_{\mathbf{p}_2}} = \frac{1}{\pi^2} \frac{p_2}{p_1} \sum_l \text{Im} [I_l(\omega, q)] , \quad (4.20)$$

where

$$I_l(\omega, q) = (2l + 1) \int V_{lm}^*(\mathbf{r}) \delta\rho_l(\omega, q, \mathbf{r}) d\mathbf{r} . \quad (4.21)$$

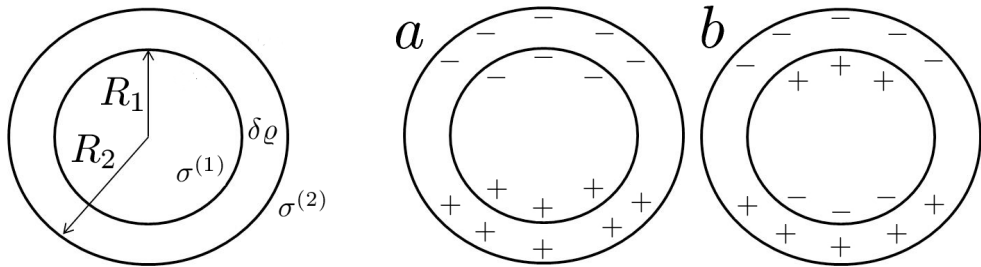


Figure 4.9: Left panel: Exposure of a spherical shell of a finite width $\Delta R = R_2 - R_1$ to an external electric field causes variation of the surface charge densities, $\sigma^{(1,2)}$, and that of the volume charge density, $\delta\rho$. Right panel: representation of the symmetric (a) and the antisymmetric (b) modes of the surface plasmon.

Interaction with an electric field of a charge projectile leads to the variation of electron density in the system. In the case of a non-uniform external field, the total variation $\delta\rho_l \equiv \delta\rho_l(\omega, q, \mathbf{r})$ in a hollow system is defined as a sum of the surface charge densities $\sigma_l^{(1,2)}$ at the inner and the outer surfaces of the spherical shell and of the

volume density variation $\delta\rho_l \equiv \delta\rho_l(\omega, q, r)$ inside the shell (see Figure 4.9):

$$\delta\rho_l(r) = \sigma_l^{(1)}\delta(r - R_1) + \sigma_l^{(2)}\delta(r - R_2) + \delta\rho_l(r)\Theta(r - R_1)\Theta(R_2 - r) . \quad (4.22)$$

The volume density variation causes the formation of the volume plasmon, while the variations of the surface densities correspond to two surface plasmon modes. The volume plasmon is formed due to compression of the electron density inside the volume of the shell and, therefore, does not interfere with either of the surface plasmon modes. The formation of the volume plasmon in the electron impact ionization of metal clusters was studied in Ref. [161]. Recently, the model accounting for the contribution of different plasmon modes was successfully utilized to describe the experimentally observed variation of the electron energy loss spectra of C₆₀ in collision with fast electrons [27,28].

Presenting the multipole variation of the electron density, $\delta\rho_l(\omega, q, \mathbf{r})$, as a sum of three contributions, and using the explicit expression for the multipolar potential $V_{lm}(\mathbf{r})$, defined by equations (4.15) and (4.18), the function $I_l(\omega, q)$ can be written as follows:

$$I_l(\omega, q) = I_l^{(v)}(\omega, q) + I_l^{(s)}(\omega, q) + I_l^{(a)}(\omega, q) , \quad (4.23)$$

where

$$\begin{aligned} I_l^{(v)}(\omega, q) &= \frac{4\pi Z^2}{q^2} (2l + 1) \int_0^\infty r^2 j_l(qr) \delta\rho_l(\omega, q, r) dr, \\ I_l^{(s/a)}(\omega, q) &= \frac{4\pi Z^2}{q^2} (2l + 1) \int_0^\infty r^2 j_l(qr) \sigma_l^{(j)}(\omega, q, r) dr, \quad j = 1, 2 . \end{aligned} \quad (4.24)$$

The double differential inelastic scattering cross section of a fast projectile in collision with a hull-like system is defined within the PRA as a sum of three terms:

$$\frac{d^2\sigma_{\text{pl}}}{d\varepsilon_2 d\Omega_{\mathbf{p}_2}} = \frac{d^2\sigma^{(s)}}{d\varepsilon_2 d\Omega_{\mathbf{p}_2}} + \frac{d^2\sigma^{(a)}}{d\varepsilon_2 d\Omega_{\mathbf{p}_2}} + \frac{d^2\sigma^{(v)}}{d\varepsilon_2 d\Omega_{\mathbf{p}_2}} , \quad (4.25)$$

which describe the partial contribution of the surface (the two modes, s and a) and the volume (v) plasmons. Different plasmon terms appearing on the right-hand side of (4.25) are constructed as a sum over different multipole contributions corresponding to different values of the angular momentum l :

$$\begin{aligned}
 \frac{d^2\sigma^{(s)}}{d\varepsilon_2 d\Omega_{\mathbf{p}_2}} &= \frac{2R_2 Z^2 p_2}{\pi q^4 p_1} \omega \sum_l \frac{\omega_l^{(s)2} \Gamma_l^{(s)} S_l^{(s)}(q)}{(\omega^2 - \omega_l^{(s)2})^2 + \omega^2 \Gamma_l^{(s)2}} \\
 \frac{d^2\sigma^{(a)}}{d\varepsilon_2 d\Omega_{\mathbf{p}_2}} &= \frac{2R_2 Z^2 p_2}{\pi q^4 p_1} \omega \sum_l \frac{\omega_l^{(a)2} \Gamma_l^{(a)} S_l^{(a)}(q)}{(\omega^2 - \omega_l^{(a)2})^2 + \omega^2 \Gamma_l^{(a)2}} \\
 \frac{d^2\sigma^{(v)}}{d\varepsilon_2 d\Omega_{\mathbf{p}_2}} &= \frac{2R_2 Z^2 p_2}{\pi q^4 p_1} \omega \sum_l \frac{\omega_p^2 \Gamma_l^{(v)} V_l(q)}{(\omega^2 - \omega_p^2)^2 + \omega^2 \Gamma_l^{(v)2}} .
 \end{aligned} \tag{4.26}$$

Here ε_2 is the kinetic energy of the scattered projectile, \mathbf{p}_2 its momentum, and $d\Omega_{\mathbf{p}_2}$ its solid angle. $\omega_l^{(s)}$ and $\omega_l^{(a)}$ are the frequencies of the symmetric and antisymmetric surface plasmons of multipolarity l :

$$\omega_l^{(s/a)} = \left(1 \mp \frac{1}{2l+1} \sqrt{1 + 4l(l+1)\xi^{2l+1}} \right)^{1/2} \frac{\omega_p}{\sqrt{2}} , \tag{4.27}$$

where "−" and "+" stand for symmetric and antisymmetric modes, respectively. In the dipole case ($l = 1$), this expression reduces to Eq. (4.6). The volume plasmon frequency ω_p , associated with the ground-state electron density ρ_0 of N electrons, is given by

$$\omega_p = \sqrt{4\pi\rho_0} = \sqrt{3N/(R_2^3 - R_1^3)} . \tag{4.28}$$

The functions $S_l^{(s)}(q)$, $S_l^{(a)}(q)$ and $V_l(q)$ in (4.26) are the diffraction factors depending on the transferred momentum q [159]. They determine the relative significance of the multipole plasmon modes in various ranges of scattering angles. The dominant contribution of different multipole modes results in a significant angular dependence for the differential cross sections [28]. Explicit expressions for these functions are given in Ref. [159].

4.2.3 Electron production via the plasmon excitation mechanism

Let us utilize the above-presented formalism for studying electron production by small gold nanoparticles via the plasmon excitation mechanism. The doubly differential cross section $d^2\sigma_{\text{pl}}/d\varepsilon_2 d\Omega_{\mathbf{p}_2}$, Eq. (4.25), can be written in terms of the energy loss $\Delta\varepsilon = \varepsilon_1 - \varepsilon_2$ of the incident projectile of energy ε_1 . Integration of $d^2\sigma_{\text{pl}}/d\Delta\varepsilon d\Omega_{\mathbf{p}_2}$ over the solid angle leads to the single differential cross section:

$$\frac{d\sigma_{\text{pl}}}{d\Delta\varepsilon} = \int d\Omega_{\mathbf{p}_2} \frac{d^2\sigma_{\text{pl}}}{d\Delta\varepsilon d\Omega_{\mathbf{p}_2}} = \frac{2\pi}{p_1 p_2} \int_{q_{\text{min}}}^{q_{\text{max}}} q dq \frac{d^2\sigma_{\text{pl}}}{d\Delta\varepsilon d\Omega_{\mathbf{p}_2}}, \quad (4.29)$$

where \mathbf{p}_1 is the initial momentum of the projectile and $\mathbf{q} = \mathbf{p}_1 - \mathbf{p}_2$ the transferred momentum.

Figure 4.10 shows the cross section $d\sigma_{\text{pl}}/d\Delta\varepsilon$ calculated for the Au_{32} cluster irradiated by fast protons of incident energies ranging from 0.1 to 10 MeV. As mentioned above, the utilized formalism relies on the the plane-wave Born approximation, which is applicable since the considered collision velocities ($v = 2 - 20$ a.u.) are significantly larger than the characteristic velocities of delocalized valence electrons in the cluster ($v_e \approx 0.5$ a.u.). The figure demonstrates that the amplitude of the plasmon resonance depends strongly on the kinetic energy of the proton. It was shown previously [162] that the relative contribution of the quadrupole ($l = 2$) and higher multipole terms to the cross section decreases significantly with an increase of the collision velocity. At high velocities, the dipole contribution dominates over the higher multipole contributions, since the dipole potential decreases slower at large distances than the higher multipole potentials.

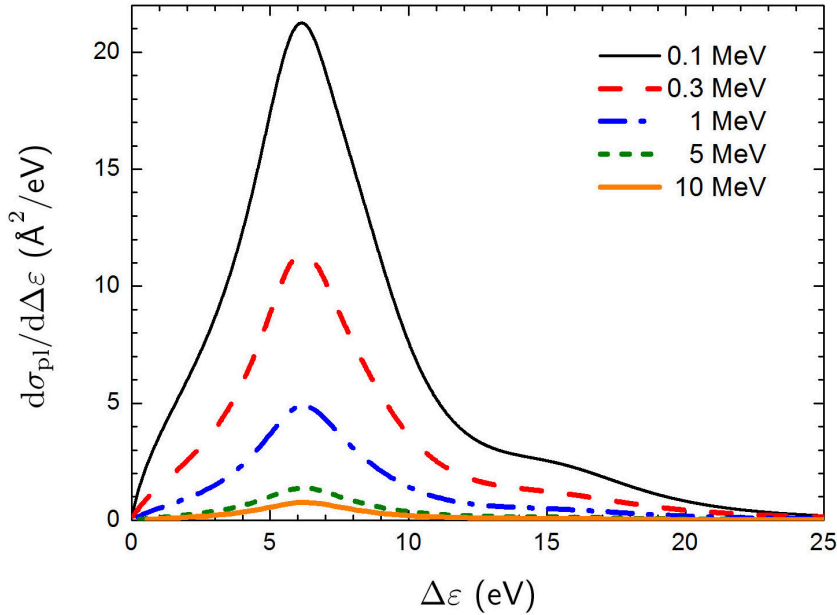


Figure 4.10: Contribution of the plasmon excitations to the single differential cross section, $d\sigma_{\text{pl}}/d\Delta\varepsilon$, of the Au_{32} cluster irradiated by fast protons of different incident energies as a function of the energy loss. The figure is adapted from Ref. [24].

The presented spectra comprise contributions of both the surface and the volume plasmon excitations, and different multipole terms contribute to each of them. Calculating the cross sections presented in Figure 4.10, we accounted for the contribution of

the dipole ($l = 1$), quadrupole ($l = 2$) and octupole ($l = 3$) terms. The excitations with large angular momenta have a single-particle rather than a collective nature [162]. With increasing l , the wavelength of a plasmon excitation, $\lambda_{pl} = 2\pi R/l$, becomes smaller than the characteristic wavelength of the delocalized electrons in the system, $\lambda_e = 2\pi/\sqrt{2}\epsilon$. Here $\epsilon \sim I_p$ is the characteristic electron excitation energy in the cluster, and I_p is the ionization threshold of the system. The DFT calculations of the electronic structure of Au₃₂ (see Section 4.1) derived the value of $I_p = 5.77$ eV, while the calculated HOMO-LUMO gap is 1.54 eV. Thus, one estimates a characteristic excitation energy of delocalized electrons in Au₃₂ to be of the order of several electronvolts, that results in the account of the three multipole plasmon terms.

Following the methodology utilized in Ref. [28], it was assumed that the ratio $\gamma_l = \Gamma_l/\omega_l$ of the width of the plasmon resonance to its frequency equals to $\gamma_l^{(s)} = 0.6$ for all multipole terms of the symmetric mode, and to $\gamma_l^{(a)} = 1.0$ for the antisymmetric mode. These values were also utilized successfully to describe the main features of the photon and electron impact ionization cross sections of the C₆₀ fullerene (see Chapter 5), whose topology is similar to the Au₃₂ cluster. For the volume plasmon the ratio $\gamma_l^{(v)} = \Gamma_l^{(v)}/\omega_p = 1.0$ was considered.

Figure 4.11 illustrates the contribution of different plasmon modes to the spectrum of Au₃₂ irradiated by a 1 MeV proton and also partial contributions of different multipole modes. The main contribution to the cross section comes from the symmetric mode of the surface plasmon, which, in turn, is dominated by the dipole excitation. The figure shows that the relative contribution of the surface plasmon exceeds that of the volume plasmon by more than an order of magnitude. Thus, the leading mechanism of electron production by gold nanoparticles is related to the surface plasmon. This result contradicts with the recent Monte Carlo simulations [192], where the authors claimed to include the contribution of plasmon excitations when calculating the cross sections of electron and proton impact on noble metal nanoparticles. One should note, however, that only "...the most simplest type of volume plasmon excitation..." was accounted for in those simulations [192]. On this basis, it was stated that the plasmon excitation does not play an important role in the process of electron emission from metallic nanoparticles, contributing much less to the overall cross sections than individual excitations. As will be shown further in this section, the emission of the low-energy electrons from the gold nanoparticles is indeed a prominent effect, which should be accounted for when estimating the secondary electron yield in a biological medium with embedded nanoparticles.

Note that the maximum of the resonance peak is located at 6.3 eV, that is slightly above the ionization threshold of Au₃₂, $I_p = 5.77$ eV. The plasmons located above the ionization threshold can decay via the ionization process [161]. On the contrary,

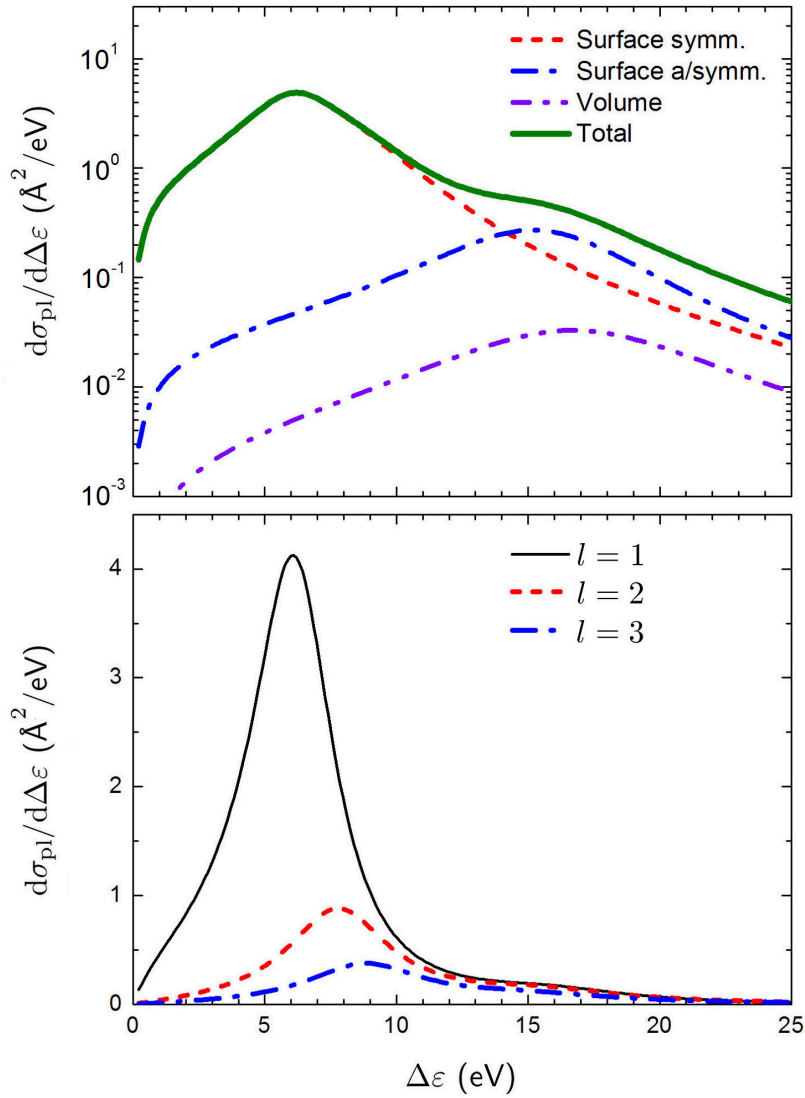


Figure 4.11: Single differential cross section $d\sigma_{pl}/d\Delta\varepsilon$ of the Au_{32} cluster irradiated by a 1 MeV proton as a function of the energy loss. Upper panel illustrates the contribution of different plasmon excitations to the resulting spectrum. Lower panel shows the contribution of different multipole terms. The figure is adapted from Ref. [24].

the decay of a collective excitation located below the ionization threshold results in single-electron excitations, which can also be coupled with the ionic motion by the electron-phonon coupling [194]. Therefore, decay of the surface plasmon in Au_{32} results in the electron emission from the system which can be accompanied by vibrations of the ionic core.

To quantify the production of electrons via the plasmon excitation mechanism, the cross section $d\sigma_{pl}/d\Delta\varepsilon$ was redefined as a function of the kinetic energy E of emitted electrons. This quantity is related to the energy loss via $E = \Delta\varepsilon - I_p$, where I_p is the ionization threshold of the system. The cross section $d\sigma_{pl}/dE$ can be related to the probability to produce N electrons with kinetic energy E , in the interval dE , emitted

from a segment dx , via [13]:

$$\frac{d^2N(E)}{dx dE} = \frac{1}{V} \frac{d\sigma_{pl}}{dE}, \quad (4.30)$$

where V is the volume occupied by the nanoparticle. Assuming that the linear size of the Au_{32} cluster is $d \approx 0.9$ nm [166,167], we calculated the number of electrons per unit length per unit energy emitted from this system due to proton irradiation. Figure 4.12 illustrates the dependence of this quantity on kinetic energy of emitted electrons for different incident energies of the proton.

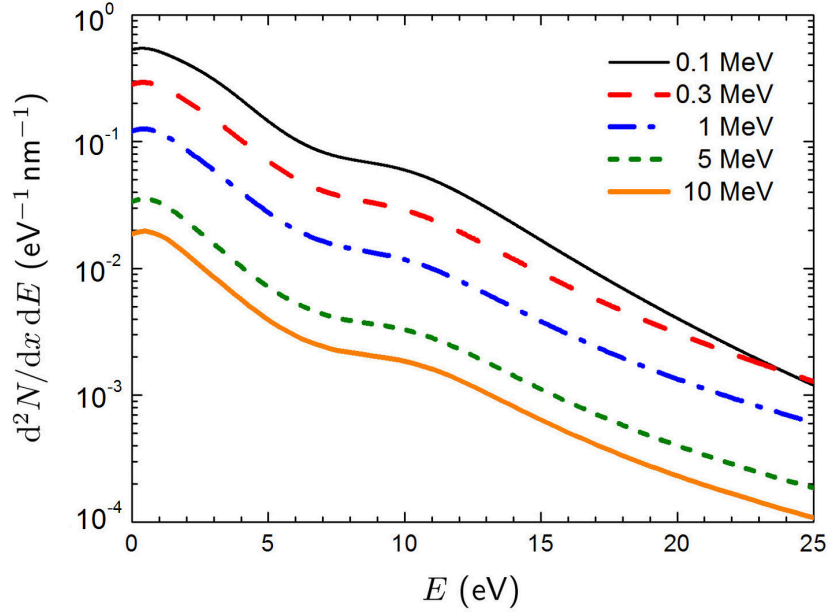


Figure 4.12: Number of electrons per unit length per unit energy emitted via the plasmon excitation mechanism from the Au_{32} cluster irradiated by a fast proton. Different curves illustrate different values of the proton's kinetic energy. The figure is adapted from Ref. [24].

Figure 4.13 compares the electron production by Au_{32} (red curve) and by an equivalent volume of pure water medium (blue curves) irradiated by a 1 MeV proton. Solid and dashed blue curves represent the results obtained recently within the dielectric formalism [195,196]. This approach is based on the experimental measurements of the energy-loss function of the target medium, $\text{Im}[-1/\epsilon(\omega, q)]$, where $\epsilon(\omega, q)$ is the complex dielectric function, with ω and q being the energy and the momentum transferred to the electronic excitation, respectively. Comparative analysis of the spectra reveals that the number of the low-energy electrons (with the kinetic energy of about a few eV) produced by the gold nanoparticle is about one order of magnitude higher than by liquid water.

In the above-presented analysis, the hollow cluster of diameter $d \approx 0.9$ nm was considered. An additional estimate was done also for a space-filling structure of a similar

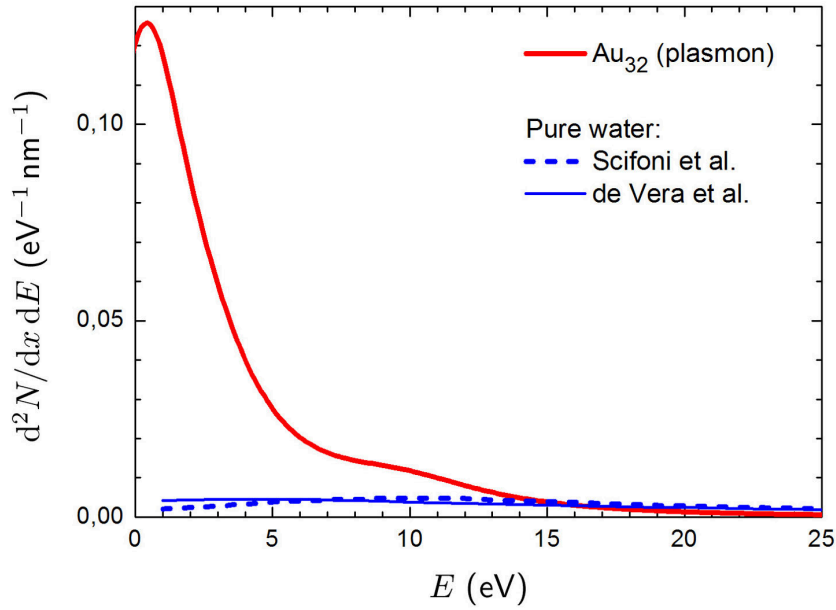


Figure 4.13: Number of electrons per unit length per unit energy emitted via the plasmon excitation mechanism from the Au_{32} cluster irradiated by a 1 MeV proton (red curve). Blue curves represent the number of electron generated from an equivalent volume of pure water. Solid and dashed blue curves represent the results obtained within the dielectric formalism by Scifoni *et al.* [195] and de Vera *et al.* [196], respectively. The figure is adapted from Ref. [24].

size. As a case study, we considered a 1 nm nanoparticle "cut" from an ideal gold crystal having the face-centered cubic (fcc) lattice with the parameter $a = 4.08 \text{ \AA}$ [117]. It was found that the 1 nm solid gold nanoparticle is composed of 31 atoms. Thus, its atomic density is close to that of the above-considered Au_{32} cluster.

The dynamic response of a solid nanoparticle can also be modeled by means of the PRA formalism assuming that the system is treated not as a "jellium" hull but as a full sphere. In this case, the electron density is uniformly distributed inside the sphere of a radius R , and the above defined radii R_1 and R_2 transform into $R_1 \rightarrow 0$ and $R_2 \equiv R$. In this case, the electron density variation on the surface and in the volume of the nanoparticle leads to the formation of the surface (symmetric mode) and the volume plasmon, respectively,

$$\frac{d^2\sigma_{\text{pl}}}{d\varepsilon_2 d\Omega_{\mathbf{p}_2}} = \frac{d^2\sigma^{(s)}}{d\varepsilon_2 d\Omega_{\mathbf{p}_2}} + \frac{d^2\sigma^{(v)}}{d\varepsilon_2 d\Omega_{\mathbf{p}_2}}, \quad (4.31)$$

while the antisymmetric surface plasmon mode does not contribute to the cross section [159]:

$$\lim_{R_1 \rightarrow 0} \frac{d^2\sigma^{(a)}}{d\varepsilon_2 d\Omega_{\mathbf{p}_2}} = 0. \quad (4.32)$$

As shown in Figure 4.11 in the case of the hollow system, the contribution of the antisymmetric mode in the 1 – 10 eV range is an order of magnitude smaller than that

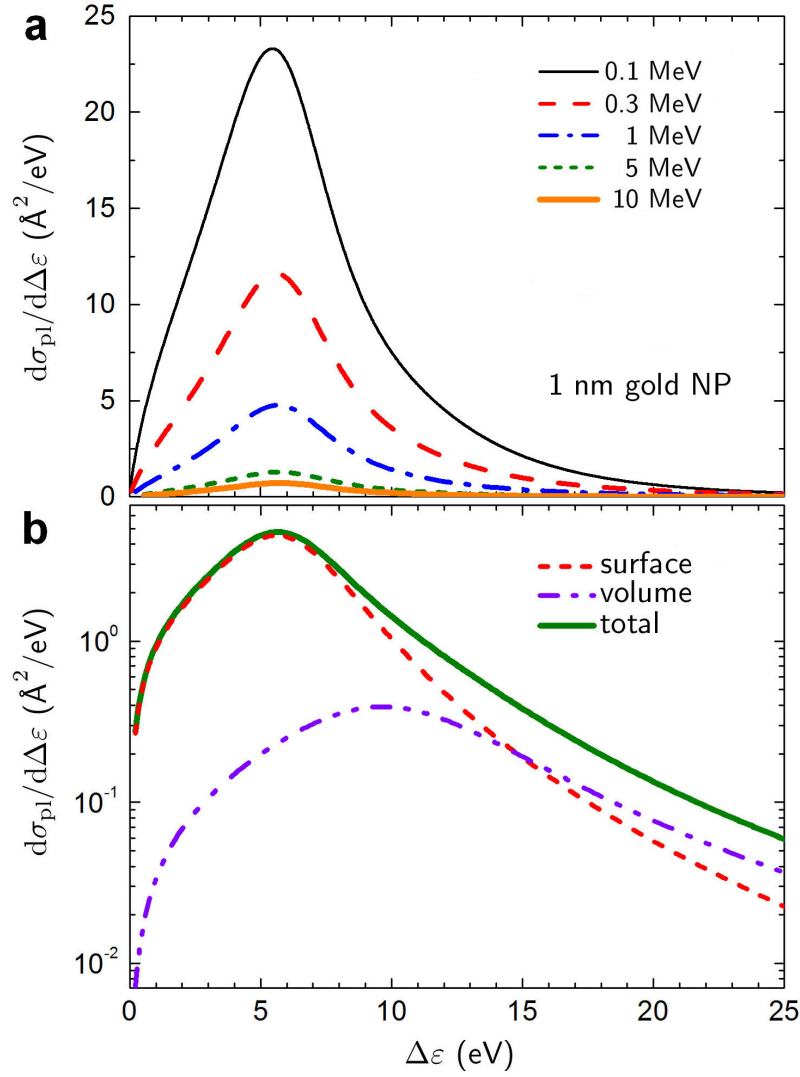


Figure 4.14: Upper panel: Contribution of the plasmon excitations to the single differential cross section, $d\sigma_{\text{pl}}/d\Delta\varepsilon$, of 1 nm gold NP irradiated by fast protons of different incident energies as a function of the energy loss. Lower panel: Contribution of different plasmon excitations to the resulting cross section $d\sigma_{\text{pl}}/d\Delta\varepsilon$ of a 1 nm gold NP irradiated by a 1 MeV proton.

of the symmetric mode. Thus, the absence of the antisymmetric mode in the excitation spectrum of the solid nanoparticle should not lead to quantitatively different results from those presented in Figure 4.11. To check this hypothesis, we have calculated the cross section $d\sigma_{\text{pl}}/d\Delta\varepsilon$ for a 1 nm solid gold nanoparticle irradiated by fast protons of different incident energies, see Figure 4.14. The figure confirms that all the above-given estimates on the electron production yield by the hollow nanoparticle of about 1 nm diameter are also valid for the case of the fcc structure. Electron production by solid nanoparticles composed of gold and other metals is analyzed in greater detail in Section 4.3.

4.2.4 Contribution of individual atomic excitations

As illustrated above (see Figure 4.5), the d electrons in the atoms of gold play a dominant role at the excitation energies from approximately 20 to 60 eV. Thus, the photoabsorption spectra of gold nanoparticles in the energy region up to 60 eV were approximated as the sum of the plasmon contribution and that of the $5d$ electron excitations in individual atoms, see Eq. (4.8). Similar to the photoionization, the two distinct types of collective electron excitations appear in the process of charge particle impact ionization. To evaluate the contribution of individual atomic excitations under ion impact, we introduce an analytical expression, which relates the cross section of photoionization with that of inelastic scattering in the dipole approximation.

For distant collisions, i.e. when the impact parameter exceeds the radius R_{at} of the atomic subshell, the ionization spectra are dominated by the dipole term [65]. On this basis, the cross sections of photoionization, $\sigma_\gamma(\omega)$, were compared to the dipole term of atomic inelastic scattering, $d\sigma_{5d}/d\Delta\varepsilon$, calculated in the Born approximation. As a result, one derives the following expression:

$$\frac{d\sigma_{5d}}{d\Delta\varepsilon} = \frac{2c}{\pi\omega v_1^2} \sigma_\gamma \ln\left(\frac{v_1}{\omega R_{5d}}\right), \quad (4.33)$$

where $\sigma_\gamma \equiv \sigma_{5d}(\omega)$ is the $5d$ photoionization cross section estimated by a Fano-type profile, Eq. (4.4), $\omega = \varepsilon_1 - \varepsilon_2$ the energy transfer, v_1 the projectile velocity, and R_{5d} a characteristic radius of the $5d$ electron shell. More details about the derivation of this expression are provided in Appendix C.

Equation (4.33), obtained within the so-called "logarithmic approximation", assumes that the main contribution to the cross section $d\sigma_{5d}/d\Delta\varepsilon$ comes from the region of large distances, $R_{5d} < r < v_1/\omega$. This relation has the logarithmic accuracy which implies that the logarithmic term dominates the cross section while all non-logarithmic terms are neglected (this approximation is described in greater detail in Ref. [197]). Making an estimate for the gold atoms, we assumed $\omega \approx 1$ a.u. which corresponds to the maximum of the $5d$ giant resonance in gold (see Fig. 4.5), $v_1 \approx 6.3$ a.u. for a 1 MeV proton, and the electron shell radius $R_{5d}(\text{Au}) \approx 2$ a.u. The latter parameter was estimated by analyzing the density distribution of the $5d$ electron shell in the atom of gold, carried out within the Hartree-Fock approach, see Figure 4.15.

It should be stressed that the interaction of the incident projectile with the nanoparticle leads to the formation of the $5d$ giant resonance not in all atoms of the system but only in those located within the impact parameter interval from $r_{\text{min}} \simeq R_{5d}$ to $r_{\text{max}} \simeq v_1/\omega$. This estimate indicates that the $5d$ giant resonance is formed in about one third of atoms of the nanoparticle.

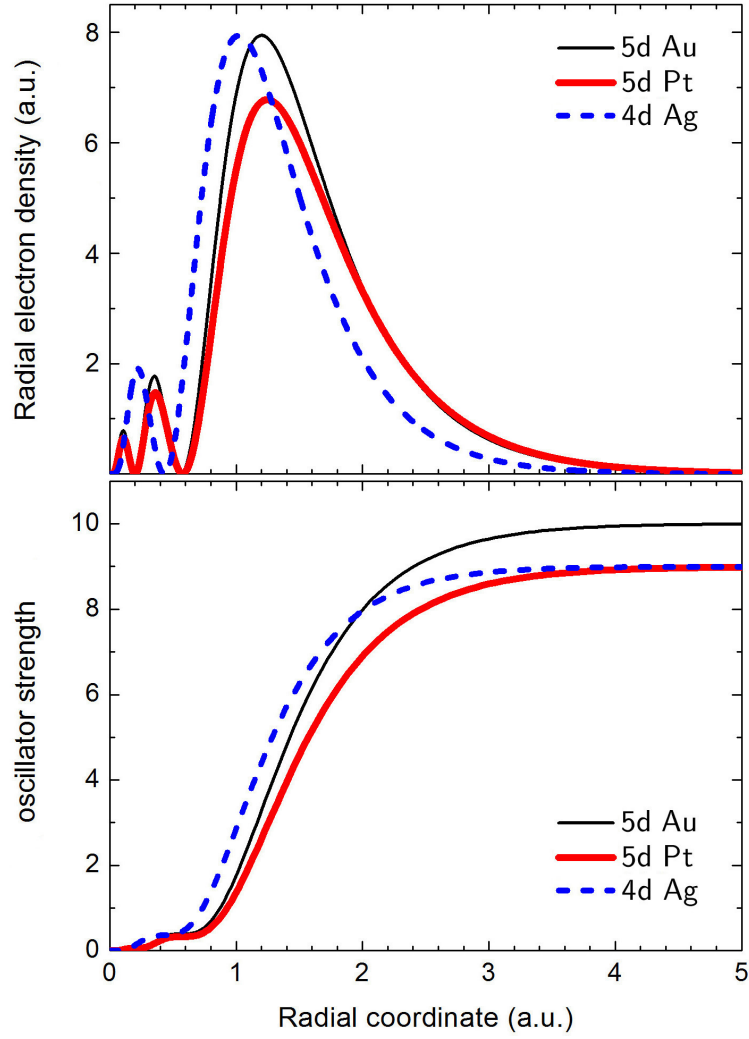


Figure 4.15: Upper panel: Radial electron density of the 5*d* and 4*d* electron shells in the atoms of gold, platinum, and silver, carried out within the Hartree-Fock approach. Lower panel: Integrated oscillator strength distributions for the 5*d* and 4*d* electron shells, which yield the number of electrons occupying a given shell.

The number of electrons per unit length per unit energy produced via the excitation of 5*d* electrons in individual gold atoms, is defined as:

$$\frac{d^2N(E)}{dx dE} = A n \frac{d\sigma_{5d}}{dE}, \quad (4.34)$$

where n is the atomic density of the target, and $A \approx 1/3$ is the ratio of the number of atoms possessing the 5*d* resonance to the total number of atoms in the nanoparticle.

To estimate the total number of electrons produced due to the collective excitations in the gold nanoparticle, we have accounted for the contribution of the plasmon excitations and excitations of 5*d* electrons in individual atoms. Figure 4.16 shows the relative enhancement of the electron yield from the Au₃₂ cluster as compared to pure

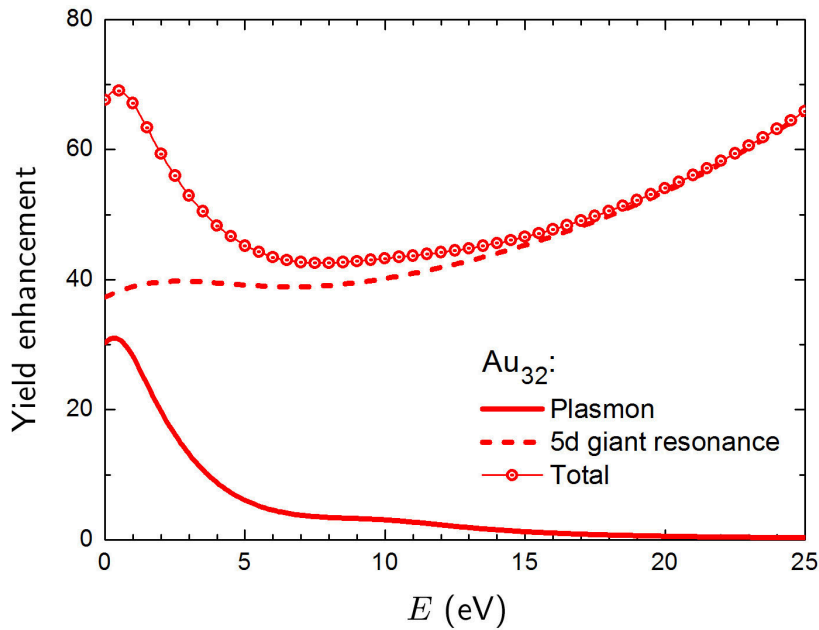


Figure 4.16: Yield enhancement from the Au_{32} cluster as compared to an equivalent volume of pure water [196]. The solid and dashed lines show the contribution of the plasmons and the atomic $5d$ excitations, respectively. Symbols illustrate the resulting enhancement. The figure is adapted from Ref. [24].

water. The data for the gold nanoparticle are normalized to the spectrum for liquid water [196]. The solid line shows the contribution of the plasmon excitations to the electron yield, while the dashed line presents the contribution from the atomic $5d$ giant resonance, estimated using Eq. (4.33) and (4.34). When making this estimate, it was assumed that the ionization cross sections of individual atoms are dominated by the dipole excitation. Contribution of quadrupole and higher multipole terms will lead to an increase in the number of emitted electrons but their relative contribution will be not as large as that from the dipole excitation. Accounting for the plasmon contribution leads to a significant additional increase in the number of $1 - 5$ eV emitted electrons as compared to the pure water. Due to the collective electron excitations arising in the ~ 1 nm gold nanoparticle, it can thus produce up to 70 times larger number of the low-energy electrons comparing to the equivalent volume of pure water medium. These results indicate that the decay of the collective electron excitations in gold nanoparticles is an important mechanism of electron yield enhancement.

4.2.5 Different kinematic conditions for charged-particle impact

In this section, we analyze how the contribution of the plasmon and the $5d$ excitation mechanisms evolves for different projectile velocities.

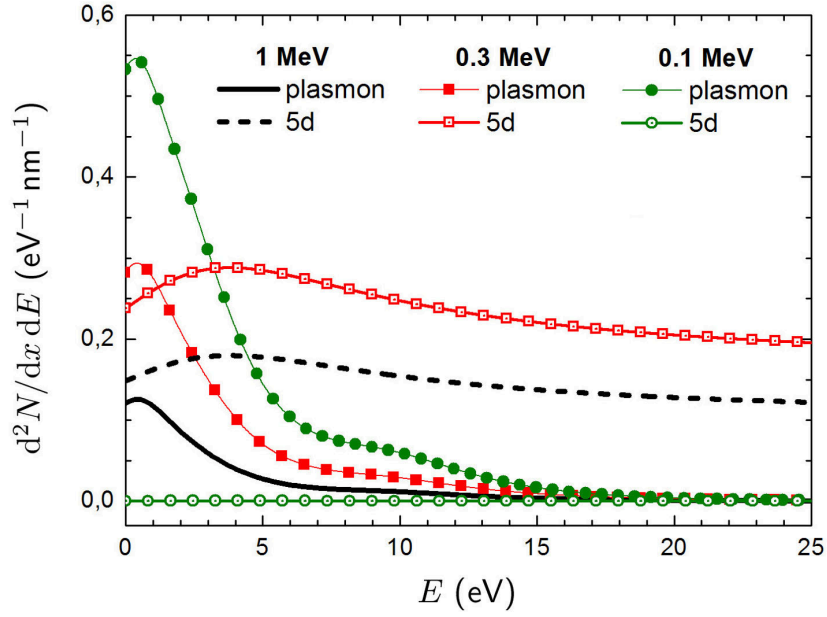


Figure 4.17: Number of electrons per unit length per unit energy produced via the plasmon and the $5d$ excitation mechanisms in the Au_{32} cluster irradiated by a proton of different kinetic energies. Solid line and filled symbols illustrate the plasmon contribution to the electron production yield. Dashed line and open symbols show the contribution of the $5d$ giant resonance. The figure is adapted from Ref. [24].

In the case of the Au_{32} cluster irradiated by a 1 MeV proton, the number of electrons produced via the excitations in individual atoms is generally higher than that produced via the plasmon excitation mechanism (see Figure 4.16). At certain kinematic conditions, the plasmon contribution to the low-energy (of about 1 – 10 eV) electron yield from the gold nanoparticle can exceed significantly that due to the atomic giant resonance. An illustration of this effect is given in Figure 4.17, where the yields of electron production due to irradiation by 1, 0.3, and 0.1 MeV protons have been compared. The electron yield due to the plasmon excitations grows with decreasing the projectile's energy (see also Figure 4.12). On the contrary, the yield due to the atomic excitations exhibits a different behavior. The number of electrons emitted from the Au_{32} cluster via the decay of the atomic $5d$ excitation by a 0.3 MeV proton is larger than in the case of a 1 MeV projectile. However, a decrease of incident energy down to 0.1 MeV leads to an abrupt decrease of the number of produced electrons. As follows from Eq. (4.33), at $\varepsilon_1 = 0.1$ MeV ($v_1 = 2.00073$ a.u.), the dipole term of the $5d$ inelastic scattering cross section is strongly suppressed, as the $\ln(v_1/\omega R_{5d})$ term approaches zero. In this case, the yield of electrons with kinetic energy below 5 eV due to the plasmon excitation exceeds that due to the $5d$ atomic excitation by the factor of about 10^3 .

4.3 Comparative analysis of electron production by different metal nanoparticles

In this section, the above-presented methodology is applied to compare electron production by different metal nanoparticles irradiated by fast protons. In addition to gold nanoparticles, we focus our attention on the systems composed of platinum, silver and gadolinium. Similar to the analysis presented in Section 4.2, we account for the two collective electron effects, namely excitation of delocalized electrons in a nanoparticle (plasmons) and that of d electrons in individual atoms (atomic giant resonances). Thus, the single differential inelastic scattering cross section of a fast projectile in collision with a nanoparticle is described as a sum of the contributions of the plasmon and individual atomic excitations:

$$\frac{d\sigma}{d\Delta\varepsilon} = \frac{2\pi}{p_1 p_2} \int_{q_{\min}}^{q_{\max}} q dq \frac{d^2\sigma}{d\Delta\varepsilon d\Omega_{\mathbf{p}_2}} \approx \frac{d\sigma_{\text{pl}}}{d\Delta\varepsilon} + \frac{d\sigma_{\text{at}}}{d\Delta\varepsilon}. \quad (4.35)$$

As noted above, this assumption relies on the similarity of the collective electron phenomena that occur in the ionization with photons and charged projectiles.

As follows from Eq. (4.31), the plasmon contribution to the double differential cross section, $d^2\sigma_{\text{pl}}/d\Delta\varepsilon d\Omega_{\mathbf{p}_2}$, for a solid spherical nanoparticle is defined by the surface (s) and the volume (v) plasmon terms, which are constructed as a sum over different multipole contributions corresponding to different values of the angular momentum l . Similar to the analysis presented in Section 4.2.3, we account for the dipole ($l = 1$), quadrupole ($l = 2$), and octupole ($l = 3$) terms. In the dipole case, parameters of the PRA were validated by fitting the TDDFT-based spectra of gold clusters to those calculated within the model approach (see Section 4.1). It came out from this analysis that about 1.5 electrons from each gold atom contribute to the plasmon excitation. This value was also utilized for our estimates of electron production by other metals. Because of significant difficulties in calculating the *ab initio*-based spectra for platinum and gadolinium, it was not possible to define precisely the PRA parameters for the considered metals. Thus, we utilized the same ratio of the plasmon resonance width to its frequency, $\Gamma_l^{(s)}/\omega_l^{(s)} = \Gamma_l^{(v)}/\omega_p = 0.6$, as in the case of gold. In the latter case, it was based on the dipole plasmon width $\Gamma_1^{(s)} = 4.0 \text{ eV} \approx 0.6\omega_1^{(s)}$, which was used to reproduce the low-energy peak in the photoabsorption spectra of gold clusters by means of the PRA scheme (see Figure 4.5).

At higher excitation energies, the photoionization cross sections of different metals were estimated based on the X-ray absorption data by Henke et al. [175]. Figure 4.18 demonstrates that, similar to the case of gold, the ionization spectra of platinum and

silver are also characterized by the prominent features at about 20 eV and above, which can be associated with the d electrons.

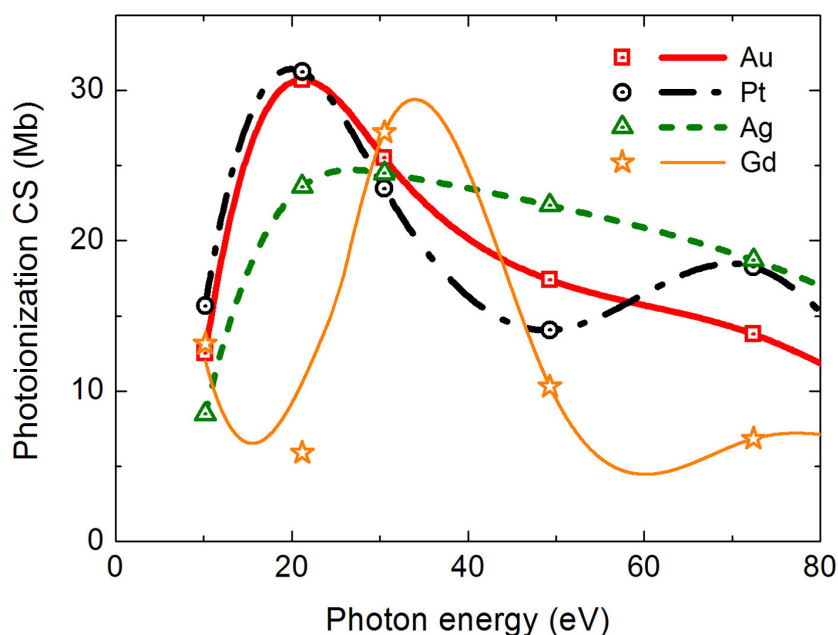


Figure 4.18: Photoionization cross section of the atoms of gold (squares), platinum (circles), silver (triangles), and gadolinium (stars). Symbols represent the X-ray absorption data taken from the Henke tables [175]. The spline interpolation of these data is illustrated by lines.

With the help of Eq. (4.33), one can relate the cross sections of photoionization, σ_γ , and the dipole term of inelastic scattering, $d\sigma_{\text{at}}/d\Delta\varepsilon$, calculated in the Born approximation. For the studied noble metal atoms, we assumed $\omega \approx 1$ a.u. which corresponds to the maximum of the $5d(4d)$ giant resonance in gold and platinum (silver), $v_1 \approx 6.3$ a.u. for a 1 MeV proton, and the electron shell radii $R_{5d}(\text{Au, Pt}) \approx R_{4d}(\text{Ag}) \approx 2$ a.u (see Figure 4.15). A similar estimate was made also for a Gd atom. Contrary to the noble metals, the Gd atom has a single electron in the $5d$ shell. Thus, there is no atomic giant resonance in the ionization spectrum of Gd in the 20 – 60 eV range, and the spectrum is characterized by a narrower peak at $\omega \approx 1.2$ a.u. (see Figure 4.18), formed due to ionization of the $5p$ shell.

Figure 4.19 presents the number of electrons per unit length per unit energy produced via the *plasmon excitation* mechanism by the 1 nm spherical nanoparticles due to 1 MeV proton irradiation. The electron production by the equivalent volume of pure water medium [196] is also shown. Comparative analysis of the spectra demonstrates that the number of low-energy electrons (with the kinetic energy of about a few eV) produced due to the plasmon excitations in all considered noble metal nanoparticles is much higher than that by liquid water.

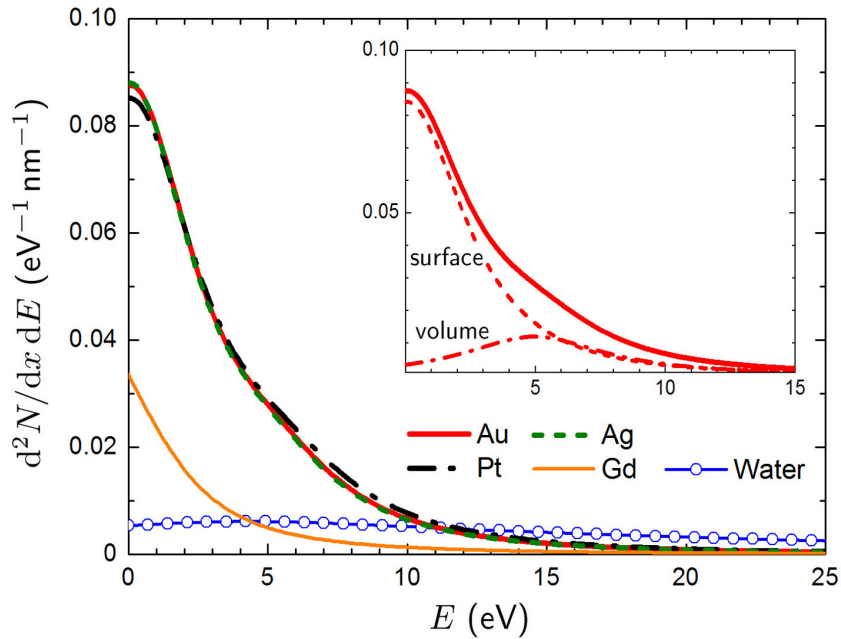


Figure 4.19: Number of electrons per unit length per unit energy produced via the plasmon excitations in the Au, Pt, Ag and Gd nanoparticles irradiated by a 1 MeV proton. Open circles represent the number of electron generated from the equivalent volume of water [196]. Inset: contributions of the surface (dashed) and the volume (dash-dotted) plasmons to the electron yield from the gold nanoparticle. The figure is adapted from Ref. [25].

The low electron yield from the Gd nanoparticle, as compared to the noble metal targets, is explained by the density effects (the atomic density of Gd is about two times smaller than that of the studied noble metals) as well as by the lower plasmon frequency. The maximum of the plasmon resonance peak in the Gd nanoparticle (4.1 eV) is located below the ionization potential of the system (~ 5.0 eV) [198]. In the case of noble metal nanoparticles, the plasmon peak maxima are in the range between 5.5 and 6.0 eV, being in the vicinity of the ionization thresholds. Therefore, the plasmon decay in noble metal nanoparticles results in the more intense electron emission as compared to the system composed of gadolinium. In the latter case, the plasmon will mostly decay into the single-electron excitations, which can lead to the vibration of the ionic core as a result of the electron-phonon coupling [194].

The inset of Fig. 4.19 demonstrates that the surface plasmon (dashed curve) gives the dominating contribution to the electron production by the solid gold nanoparticle, exceeding that of the volume plasmon (dash-dotted curve) by an order of magnitude. This result coincides with the analysis carried out in Section 4.2 for the case of a hollow system. Thus, this study reveals the significance of the plasmon excitations in the process of electron production by sensitizing nanoparticles.

To estimate the total number of electrons produced due to the collective excita-

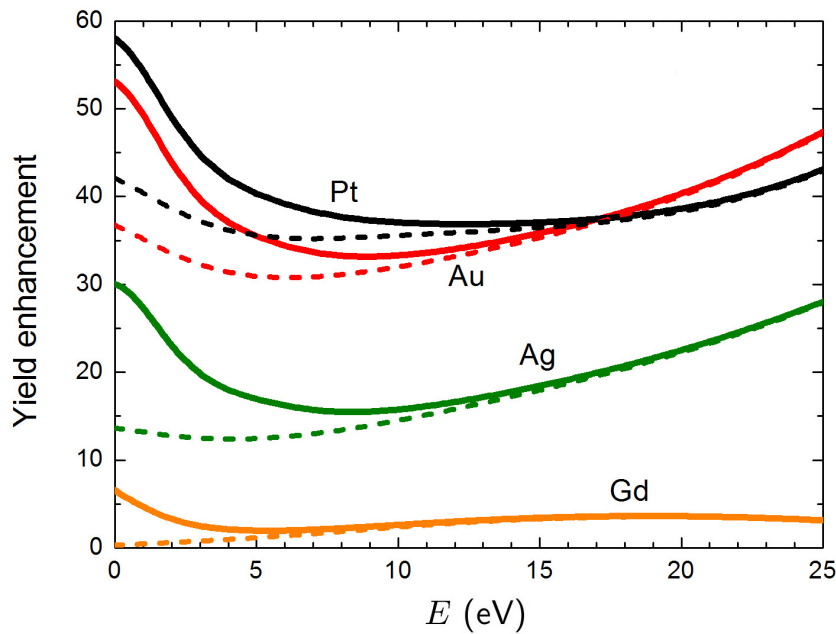


Figure 4.20: Yield enhancement from the 1 nm metallic nanoparticles. Dashed lines show the contribution of individual atomic excitations. Solid lines show the resulting contribution with an account of the plasmons. The figure is adapted from Ref. [25].

tions in the nanoparticles, we have also accounted for the contribution of excitations in individual atoms. Figure 4.20 demonstrates the relative enhancement of the electron yield from the considered nanoparticles as compared to pure water. This quantity was obtained by summing up the contribution of the plasmons and individual atomic excitations. The dashed lines present the contribution of the atomic giant resonances ($5d$ in Au and Pt, and $4d$ in Ag) as well as the total $5p + 5d$ contribution in Gd, estimated using Eq. (4.33). The solid line is the sum of the excitations in individual atoms and the plasmons. The significant yield enhancement arises in those nanoparticles whose constituent atoms possess the giant resonance, contrary to case of gadolinium which has a single $5d$ electron. Accounting for the plasmon contribution leads to a significant increase of the $1 - 5$ eV electron yield. Due to the collective electron excitations arising in these systems, the gold and platinum nanoparticles can thus produce much larger (of more than an order of magnitude) number of low-energy electrons comparing to the equivalent volume of pure water medium.

Finally, let us analyze the role of the nanoparticle size on the intensity of electron production. Figure 4.21 illustrates the electron yield from the solid gold nanoparticles of different size irradiated by the 0.1, 0.3, 1 and 10 MeV protons. We have focused on the systems of about 1 – 10 nm in diameter. Metal nanoparticles of this size range were studied recently in relation to the radiotherapies with charged ions [8, 10]. For the sake of clarity, we have calculated the number of electrons per unit energy, dN/dE . At

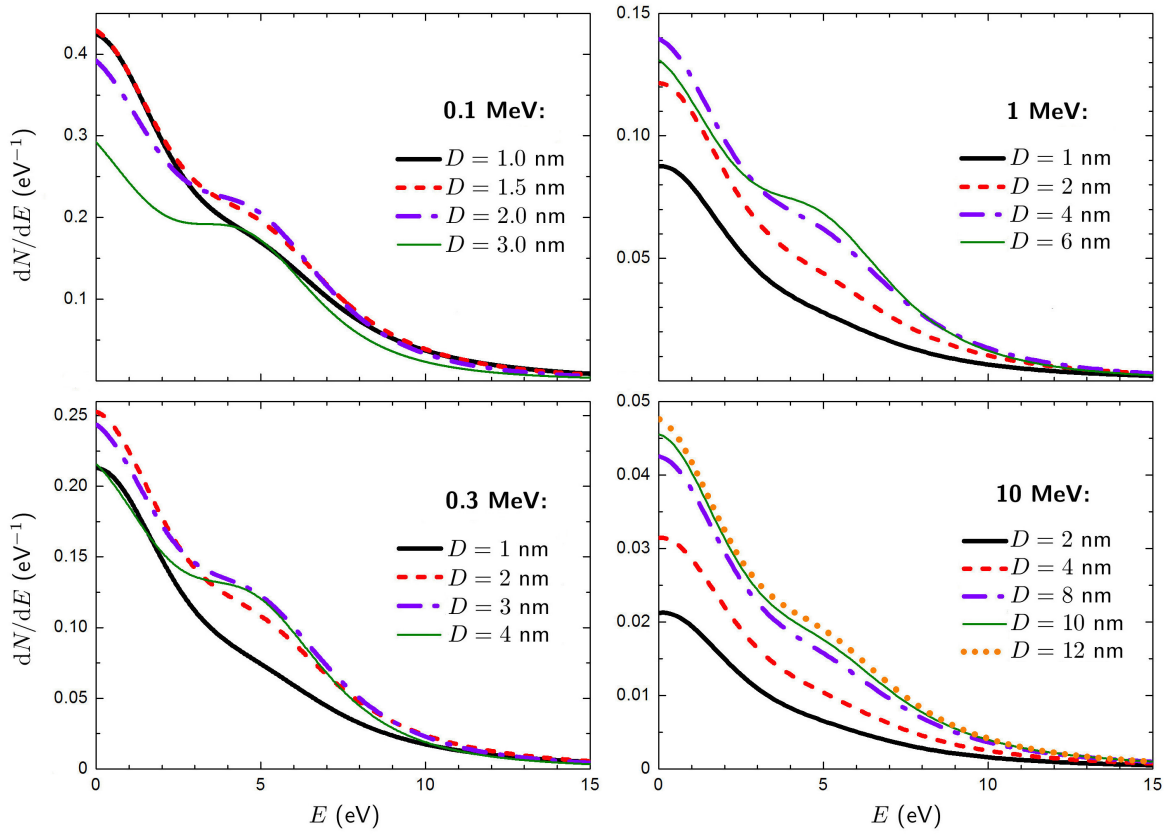


Figure 4.21: Number of electrons per unit energy produced via the plasmon excitation mechanism in the solid gold nanoparticles of different size irradiated by the protons of different kinetic energy. The figure is adapted from Ref. [24].

certain kinematic conditions, the contribution of the plasmon excitations saturates, so that larger nanoparticles emit a smaller number of electrons via the plasmon damping mechanism.

It was shown previously [162] that the dipole mode of the plasmon excitations arising in a nanoparticle gives the dominating contribution to the ionization cross section when the characteristic collision distance exceeds significantly the nanoparticle size, $v_1/\omega \gg D/2$, where D is the nanoparticle diameter. At large collision distances, the dipole contribution dominates over the higher multipole contributions. Terms with higher l become significant only in the case when the collision distances become comparable with the cluster size. This means that for a given incident energy the plasmon mechanism of electron production will be efficient for relatively small nanoparticles, while the dipole plasmon mode will be suppressed for larger D . This behavior is illustrated in Figure 4.21. For instance, the number of low-energy electrons emitted via the surface plasmon mechanism from a 2 nm nanoparticle irradiated by a 0.3 MeV proton (dashed red curve) is higher than that from a 4 nm nanoparticle (thin solid green curve). In the former case, the characteristic collision distance $v_1/\omega \approx 18$ a.u. becomes

comparable with the nanoparticle radius, $D/2 = 1 \text{ nm} \approx 19 \text{ a.u.}$. Therefore, a larger nanoparticle with the diameter of 4 nm emits a smaller number of electrons via the plasmon mechanism. A small increase in the number of 5 eV electrons produced by the 4 nm nanoparticle as compared to the smaller one is the result of an increased role of the volume plasmon due to the increased volume/surface ratio. A similar scenario holds for other incident velocities. For a 1 MeV proton, the plasmon contribution to the electron yield saturates for the nanoparticle with the diameter of approximately 4 nm, while for higher energies ($\varepsilon_1 = 10 \text{ MeV}$) the saturation takes place for the 12 nm nanoparticle. Thereby, the plasmon excitations play a prominent role in the production of low-energy electrons from gold nanoparticles of about 1 – 5 nm in diameter. One should stress again that this size range corresponds to the size of gold, platinum, and Gd-based nanoparticles studied recently in relation to the radiotherapy with charged ions [8, 10, 12].

Chapter 5

Emission of low-energy electrons from carbon nanoparticles

Excitation of plasmons by an external electric field is a characteristic feature of not only metal but also, to some extent, of carbon nanoscale systems. For instance, it is well established that plasmon excitations dominate the spectra of photo-, electron, and ion impact ionization of fullerenes [27, 29, 157, 163, 199, 200] and polycyclic aromatic hydrocarbons (PAHs) [201–203]. Contrary to the case of metal clusters, where the plasmon resonance peak is located in the vicinity of the ionization threshold, ionization spectra of carbon-based nanosystems are characterized by a prominent peak positioned at the energy of about 20 eV.

This chapter demonstrates that the decay of plasmons excited in carbon nanoparticles also plays a prominent role in the production of low-energy electrons. Due to the collective response to an external electric field, these systems can enhance the production of secondary electrons in a biological medium, in the energy range where the plasmons play the dominant role. This is done by the calculation of spectra of secondary electrons ejected from a carbon nanoparticle composed of fullerite, a crystalline form of C_{60} fullerene, irradiated by fast protons.

5.1 Plasmon excitations in an isolated C_{60} molecule

Similar to the case of metal nanoparticles, the contribution of plasmon excitations to the electron production is evaluated by means of the PRA. To start with, we evaluate the plasmon contribution to the ionization spectrum of an isolated C_{60} molecule. Within the utilized model, the fullerene is represented as a spherical "jellium" shell of a finite width ΔR with a homogeneous distribution of the electron density [177–179]. The chosen value, $\Delta R = 1.5 \text{ \AA}$, corresponds to the size of the carbon atom [178]. Figure 5.1

shows the radial distribution of the density of 240 delocalized electrons in C_{60} (the four valence $2s^2 2p^2$ electrons in each carbon atom form a cloud of delocalized electrons) considered within the model and that obtained from DFT calculations [204].

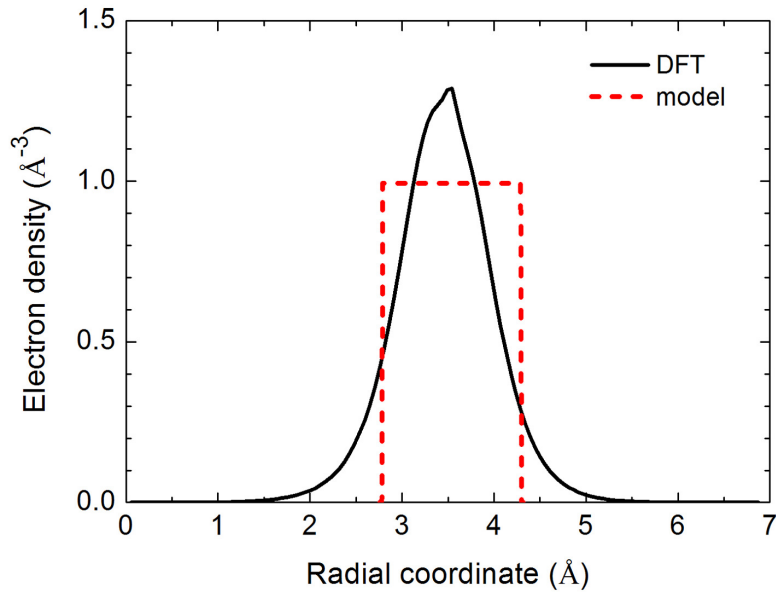


Figure 5.1: Radial distribution of the valence electron density of C_{60} obtained from DFT calculations [204] (solid curve) and that considered within the model (dashed curve). The DFT calculations were performed by means of the Gaussian 09 package [107] utilizing the local density approximation (LDA) and the 6-31G(d) basis set.

The choice of the parameters entering the PRA, namely the oscillator strength of the plasmon excitation, position of the plasmon resonance peak, and its width, has been justified by comparing the model-based spectra with experimental data and the results of more advanced *ab initio* calculations. As a benchmark of the utilized approach, the photo- and electron impact ionization cross sections of carbon-based systems, namely fullerenes and PAHs, were calculated [27–29,202]. The results obtained for C_{60} , see Figures 5.2 and 5.3, agreed well with experimental data on photoionization [205] and electron inelastic scattering [27, 28]. Being a clear physical model which describes collective electron excitations, the PRA has thus been proven to be a useful tool for interpretation of experimental results and making new numerical estimates.

Within the PRA, the double differential inelastic scattering cross section of a fast projectile in collision with a hull-like system is defined as a sum of three terms which describe the partial contribution of the two modes of the surface plasmon and of the volume plasmon, see Eq. (4.25)-(4.26). The frequencies of the symmetric and antisymmetric modes of the surface plasmon are given by Eq. (4.27) and the volume plasmon frequency, associated with the ground-state electron density ρ_0 , is given by Eq. (4.28). In the case of a fullerene C_n , the number N of delocalized electrons represents the

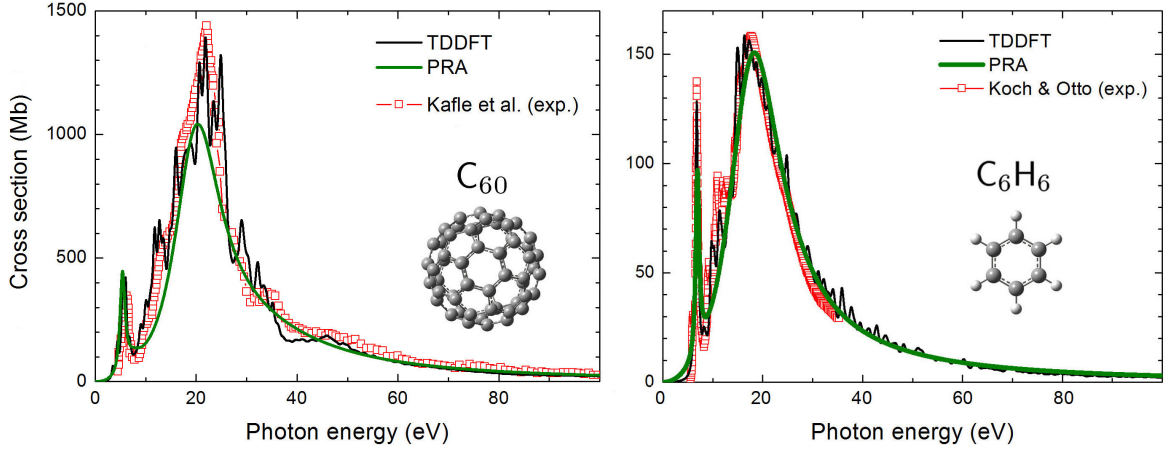


Figure 5.2: The photoabsorption cross section of C_{60} (left panel) and benzene (right panel) calculated within the TDDFT method (black line) and the plasmon resonance approximation (green line). Theoretical curves are compared to the experimental data from Kafle *et al.* [205] and Koch and Otto [206]. The figure is adapted from Ref. [202].

four $2s^22p^2$ valence electrons from each carbon atom. Thus, it is assumed that 240 delocalized electrons of C_{60} contribute to the formation of plasmons.

Studying the plasmon excitations in C_{60} , we have also accounted for the dipole ($l = 1$), quadrupole ($l = 2$) and octupole ($l = 3$) in the sum over l in Eq. (4.26). Similar to the analysis performed in Section 4.2.3 for small gold clusters, the number of multipole terms to be accounted for is evaluated by comparing the wavelength of plasmon excitation, $\lambda_{pl} = 2\pi R/l$, with the characteristic wavelength of the delocalized electrons in the system, $\lambda_e = 2\pi/\sqrt{2\epsilon}$, where $\epsilon \sim I_p(C_{60}) \approx 7.5$ eV [157]. In the case of C_{60} , this estimate shows that the excitations with $l > 3$ are formed by single electron transitions rather than by the collective ones. In Ref. [29], the single-particle excitations in C_{60} were mapped to a series of individual peaks formed atop the broad plasmon resonance peak. These peaks were either assigned to a series of optically allowed discrete transitions or related to the ionization of particular molecular orbitals of the system.

Table 5.1: Peak positions of the surface and the volume plasmon modes as well as their widths used in the present calculations. All values are given in eV.

	$\omega_l^{(s)}$	$\Gamma_l^{(s)}$	$\omega_l^{(a)}$	$\Gamma_l^{(a)}$	ω_p	$\Gamma_l^{(v)}$
$l = 1$	19.0	11.4	33.2	33.2	37.1	37.1
$l = 2$	25.5	15.3	31.0	31.0	37.1	37.1
$l = 3$	30.5	18.3	29.5	29.5	37.1	37.1

In the performed analysis, we assumed that the ratio $\gamma_l = \Gamma_l/\omega_l$ of the width of the plasmon resonance to its frequency equals to $\gamma_l^{(s)} = 0.6$ for all multipole terms of the symmetric mode, and to $\gamma_l^{(a)} = 1.0$ for the antisymmetric mode [28]. These values

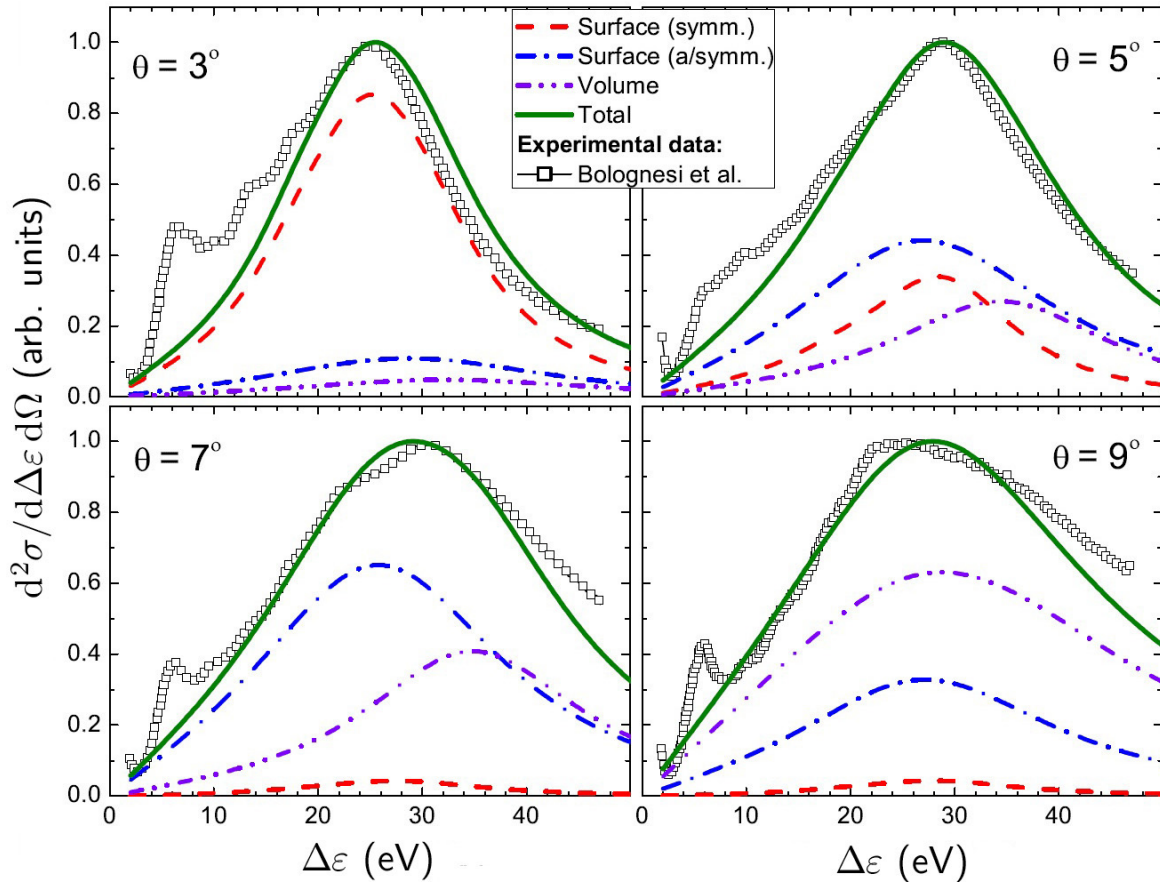


Figure 5.3: Comparison of the electron energy loss spectra calculated within the PRA and the experimental spectra measured for the incident electron energy range 1002 – 1050 eV and for the scattering angles $\theta = 3^\circ \dots 9^\circ$. The symmetric and antisymmetric modes of the surface plasmon are shown by dashed red and the dash-dotted blue lines, respectively; the volume plasmon contribution is shown by the double-dotted purple line. The total cross section is shown by the thick green line. Open squares represent the experimental data [27,28]. For the sake of convenience, both the experimental and the theoretical curves are normalized to 1 at the point of maximum. The energy scale is the same for all panels. The figure is adapted from Ref. [181].

have been utilized to describe experimental data on photoionization [205] and electron inelastic scattering [27,28] of gas-phase C_{60} , see Figures 5.2 and 5.3. The value $\gamma_i^{(s)} = 0.6$ is also close to the numbers obtained from the earlier photoionization and electron energy loss experiments on neutral C_{60} [157, 163]. The value $\gamma_i^{(a)} = 1.0$ is consistent with the widths of the second plasmon resonance observed in the photoionization of C_{60}^{q+} ($q = 1 - 3$) ions [199]. For the volume plasmon, we consider the ratio $\gamma_i^{(v)} = \Gamma_i^{(v)}/\omega_p = 1.0$. The values of the plasmon resonance peaks and the widths are summarized in Table 5.1.

5.2 Electron production by C_{60} fullerene due to the plasmon excitation mechanism

Figure 5.4 illustrates the single differential cross section $d\sigma_{\text{pl}}/d\Delta\varepsilon$ calculated by means of the PRA for the C_{60} fullerene irradiated by fast protons of different incident energies as indicated. The presented spectra comprise contributions of both the surface and volume plasmon excitations of different angular momenta l . The contribution of different plasmon modes to the spectrum of C_{60} irradiated by a 1 MeV proton is illustrated in the lower panel of Figure 5.4. Similar to electron production by noble metal nanoparticles (Section 4.2.3), the main contribution to the cross section comes from the symmetric mode of the surface plasmon, whose relative contribution is much larger than that of the volume plasmon.

Figure 5.4 demonstrates that the amplitude and the shape of the plasmon resonance depend strongly on the kinetic energy of protons. It can be explained by the fact that the relative contributions of the quadrupole and higher multipole terms to the cross section decrease significantly with an increase of the collision velocity [162]. At high velocities, the dipole term dominates over the contributions of larger l , since the dipole potential decreases slower at large distances than the higher multipole potentials. To illustrate this effect, we have plotted the partial contributions of different multipole modes which are excited due to irradiation by 0.1, 1, and 10 MeV protons. These dependencies are presented in Figure 5.5. For the sake of clarity, the cross sections, which represent the sum of three multipole contributions, have been normalized to unity at the point of maximum. Thus, one can compare directly the relative contribution of the different terms to the cross section at different incident energies. A prominent interplay of the different multipole terms at the lowest incident energy (left panel) results in a shift in the position of the maximum of the cross section.

To quantify the production of electrons in collision with a nanoparticle, the cross section $d\sigma/d\Delta\varepsilon$ is redefined as a function of the kinetic energy E of emitted electrons, $E = \Delta\varepsilon - I_p$. Figure 5.6 shows the cross section $d\sigma/dE$ of C_{60} (thick solid and dash-dotted black curves) and of a water molecule (thin solid and dashed blue curves) irradiated by a 1 MeV proton as a function of the kinetic energy of emitted electrons. The thick solid curve demonstrates the contribution of the plasmon excitations to the spectrum of C_{60} , $d\sigma_{\text{pl}}/dE$, calculated within the PRA approach. This cross section is compared to the single-differential cross section of C_{60} [26] obtained within the dielectric formalism. The results for water, also obtained within the dielectric formalism, are taken from Refs. [195, 196]. Symbols show the cross section $d\sigma/dE$ for the 1 MeV proton impact of a single carbon atom calculated by means of the binary encounter approximation (BEA), multiplied by 60. This approximation considers the collision as

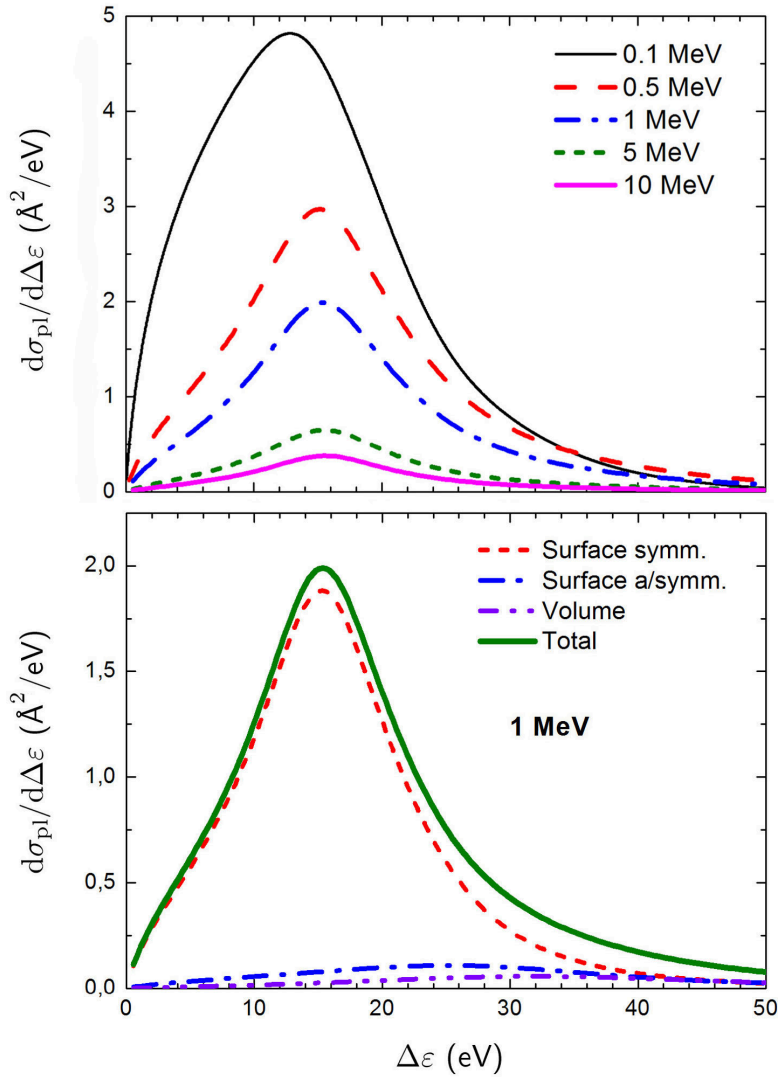


Figure 5.4: Upper panel: contribution $d\sigma_{\text{pl}}/d\Delta\varepsilon$ of the plasmon excitations to the single differential cross section of C_{60} fullerene irradiated by fast protons of different incident energies as a function of the energy loss. Lower panel illustrates the contribution of different plasmon excitations to the cross section $d\sigma_{\text{pl}}/d\Delta\varepsilon$ of C_{60} irradiated by a 1 MeV proton. The figure is adapted from Ref. [26].

a classical one between the projectile and a single electron in the target; the nucleus and the remaining electrons in the target play no part except that of providing a binding energy for the electron being ejected [207]. An agreement between the cross section for C_{60} obtained within the dielectric formalism with that within the BEA at the energy of about 20 eV and above indicates that the emission of electrons with kinetic energy of several tens of eV takes place via single-electron excitations of the system. The plasmon excitations dominate the spectrum at lower energies, i.e. in the vicinity of the plasmon resonance, while this contribution drops off at higher energies of emitted electrons. In the energy range where the plasmons are excited, single-particle effects give a small contribution as compared to the collective modes, while at higher energies, the collec-

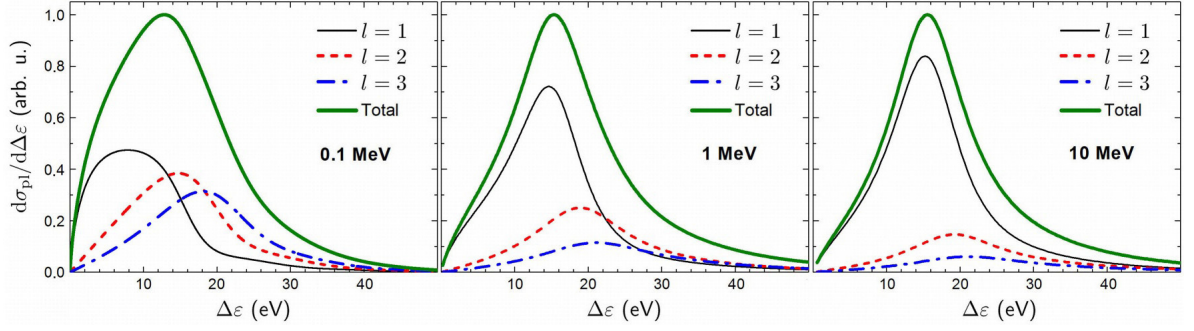


Figure 5.5: Relative contribution of different multipole terms to the single differential cross section $d\sigma_{pl}/d\Delta\varepsilon$ of C_{60} fullerene irradiated by 0.1, 1, 10 MeV protons as a function of the energy loss. The figure is adapted from Ref. [26].

tive excitation decays to the incoherent sum of single-electron excitations. Note that at lower electron energies (from 1 to approximately 20 eV) the BEA-based results start to deviate significantly from that of the dielectric formalism. This deviation indicates that the BEA is not applicable for the description of low-energy electron emission, since these electrons are produced in distant rather than in binary collisions. In this energy range, the PRA approach better describes the low-energy electron emission since it accounts for the collective electron effects omitted in other models.

5.3 Electron production by a large fullerite nanoparticle

The single differential cross section $d\sigma/dE$ calculated for an isolated C_{60} molecule (Figure 5.6) can be utilized to evaluate the production of secondary electrons by a large solid carbon nanoparticle whose density corresponds to that of fullerite, the crystalline form of C_{60} . The cross section can be related to the probability to produce N secondary electrons with kinetic energy E , in the interval dE , emitted from a segment Δx of the trajectory of a single ion [13, 208]:

$$\frac{dN(E)}{dE} = n \Delta x \frac{d\sigma}{dE}, \quad (5.1)$$

where n is the atomic density of a system of compounds,

$$n = \frac{\rho}{N_{at} m_{at}}, \quad (5.2)$$

with ρ being the mass density of a target, N_{at} the number of atoms in the target compound, and m_{at} the atomic mass.

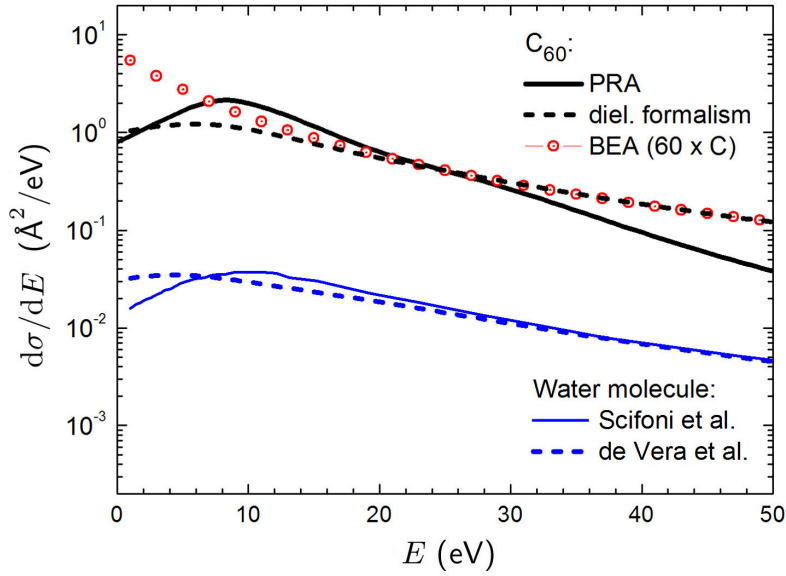


Figure 5.6: Single differential cross section $d\sigma/dE$ of the C_{60} fullerene (thick solid and dash-dotted black curves) and of a water molecule (thin solid and dashed blue curves) irradiated by a 1 MeV proton as a function of the kinetic energy of emitted electrons. Thick solid (black) curve illustrates the contribution of the plasmon excitations to the emission spectrum from C_{60} . Thin solid and dashed (blue) curves represent the results obtained within the dielectric formalism by Scifoni *et al.* [195] and de Vera *et al.* [196], respectively. Symbols represent the cross section of a single C atom calculated by means of BEA, multiplied by 60. The figure is adapted from Ref. [26].

As a case study, we have considered a large nanoparticle of 50 nm in diameter. In the calculations, it was assumed that (i) C_{60} molecules in fullerite are packed in the fcc crystalline lattice, and (ii) a unit cell is composed of four C_{60} molecules. Knowing the lattice parameter of fullerite, $a = 1.417$ nm [209], and the mass of a single carbon atom, $m_C = 12$ u, we have calculated the density of the fullerite crystal:

$$\rho(\text{fullerite}) = \frac{4 \cdot 60 m_C}{a^3} = 1.68 \text{ g/cm}^3. \quad (5.3)$$

Utilizing these values, we have obtained the atomic density of fullerite:

$$n(\text{fullerite}) = \frac{\rho(\text{fullerite})}{60 \cdot m_C} = 1.4 \cdot 10^{21} \text{ cm}^{-3}, \quad (5.4)$$

which is by about an order of magnitude smaller than that of water, $n(\text{water}) = 3.34 \times 10^{22} \text{ cm}^{-3}$.

In Figure 5.7, the electron yield from a 50 nm spherical carbon nanoparticle is compared to that from the equivalent volume of pure water medium. We have calculated the number of electrons per unit energy produced due to irradiation by a 1 MeV proton. The contribution of collective electron excitations estimated by means of the PRA

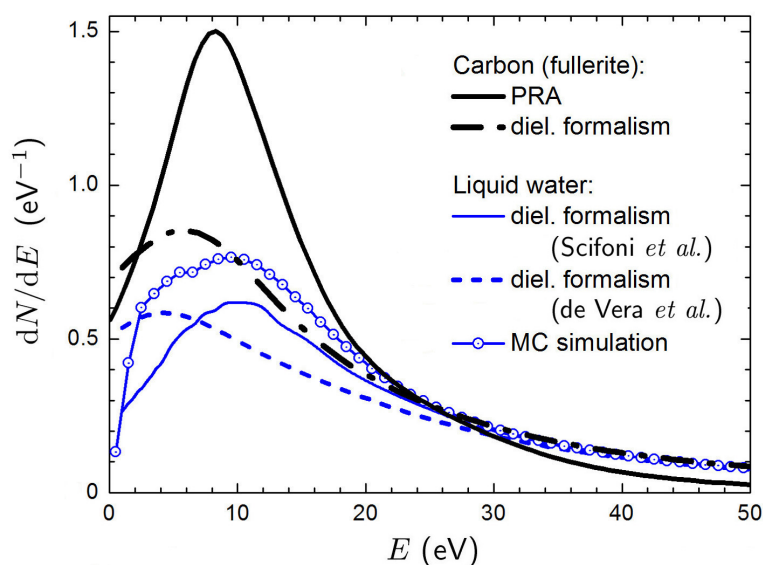


Figure 5.7: Number of electrons per unit energy produced by irradiation of a 50 nm carbon nanoparticle by a single 1 MeV proton (black curves). Blue curves represent the number of electron generated in the equivalent volume of liquid water. Solid and dashed blue curves represent the results obtained within the dielectric formalism by Scifoni *et al.* [195] and de Vera *et al.* [196], respectively. Open circles illustrate this quantity obtained on the basis of Monte Carlo simulations using the Geant4-DNA simulation tool. The figure is adapted from Ref. [26].

(thick black curve) is compared to the number of electrons estimated by means of the dielectric formalism (dash-dotted black curve) [26]. These results are also compared to the results of Monte Carlo simulations carried out by means of the Geant4 tool for pure water medium (symbols) [26]. Thin solid and dashed blue curves represent the results of recent calculation for liquid water obtained within the dielectric formalism taken from Refs. [195, 196]. Comparative analysis of the spectra demonstrates that the number of electrons with the energy of about 10 eV, produced by the carbon nanoparticle via the plasmon excitation mechanism, is several times higher than that created in pure water. Similar to the case of noble metal nanoparticles, the use of carbon-based nanostructures in radiotherapy applications can thus produce the sensitization effect. As shown in Chapter 4, the number of electrons with the energy of about a few eV produced by the gold and platinum nanoparticles via the plasmon excitation mechanism exceeds that generated in the same volume of liquid water by more than an order of magnitude. In the case of a carbon nanoparticle, the electron yield reaches the maximum at slightly higher electron energies, namely at about 10 eV.

In order to quantify the difference in electron production by the carbon nanoparticle and by an equivalent volume of pure water, we have calculated the relative enhancement of the electron yield from the nanoparticle as compared to water. This quantity is presented in Figure 5.8. The enhancement was calculated by comparing the contribution

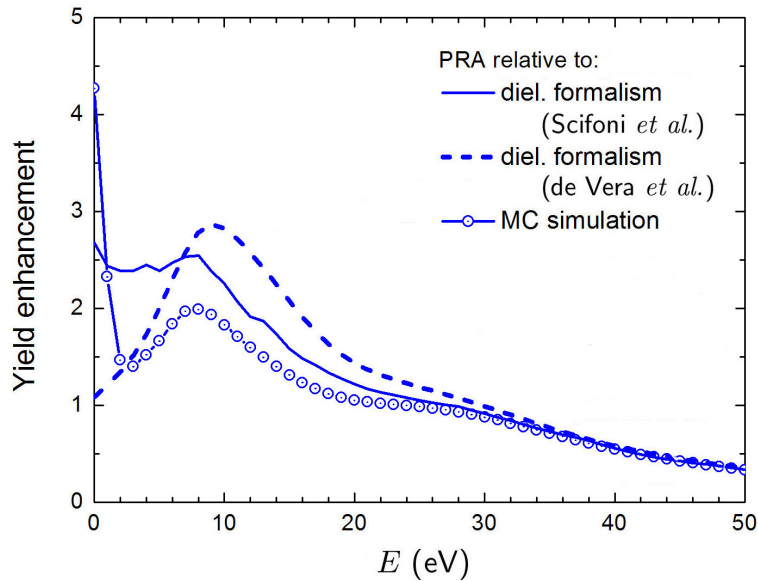


Figure 5.8: Yield enhancement from the 50 nm carbon nanoparticle as compared to pure water medium. Solid and dashed blue lines show the enhancement due to the plasmon excitations as compared to the results obtained within the dielectric formalism by Scifoni *et al.* [195] and de Vera *et al.* [196], respectively. Open symbols illustrate the plasmon-based enhancement compared to the results of Monte Carlo simulations. The figure is adapted from Ref. [26].

of the plasmon excitations, obtained within the PRA, to the electron yield from pure water calculated by means of the dielectric formalism (solid and dashed blue curves) and Monte Carlo simulations (open symbols). Depending on the data to be chosen as a reference, the collective electron excitations result in 2 to 3 times greater number of emitted 10 eV electrons as compared to the case of water. This effect is less pronounced than the enhancement done by the small noble metal nanoparticles which can produce up to 15-20 times greater number of electrons via the plasmon decay mechanism as compared to water (see Figure 4.20). On the other hand, this enhancement results in an excessive emission of the very low-energy electrons of about a few eV, while the carbon-based nanoparticle can enhance the yield of more energetic electrons. Assuming this, one may consider novel types of nanoparticles for radiotherapy applications, composed of a metal and an organic parts, where collective excitations will arise in both parts of the system. A proper choice of the constituents will allow one to tune the position of the resonance peaks in the ionization spectra of such systems and, subsequently, to cover a broader kinetic energy spectrum of electrons emitted from such nanoparticles, thus enhancing effectiveness of their biomedical applications. The fabrication of new, more efficient types of radiosensitizers would allow one to advance further modern techniques of radiotherapy treatments with ionizing radiation.

Chapter 6

Conclusion and outlook

This work has been devoted to a theoretical and computational study of stability, electronic and thermo-mechanical properties of nanomaterials which are of current interest for biomedical applications.

We have explored the ability of existing classical interatomic potentials to reproduce stability and thermo-mechanical properties of metal systems, assuming that these potentials have been fitted to describe ground-state properties of the perfect bulk materials. By studying the stability of small atomic clusters within the classical and *ab initio* frameworks, we evaluated the accuracy of the existing potentials for the description of systems on the atomistic scale, where quantum effects play a crucial role. This issue is important, for instance, in the case of nanostructured materials, where grains or nanocrystals have a typical size of about a few nanometers. For such systems, it is important to describe rather accurately both bulk properties and the properties of nanoscale systems consisting of several tens-hundreds of atoms.

As a case study, we investigated the force fields which describe interactions between nickel and titanium atoms. Nanomaterials made of these metals attract attention for the development of biocompatible implants. We demonstrated that the classical interatomic potentials fitted to describe ground-state properties of bulk titanium, nickel and an equiatomic NiTi alloy can also describe, with a reasonable accuracy, the properties of much smaller systems that are driven by classical interatomic interactions. Therefore, one can use a single set of the force fields to describe the bulk properties of the material as well as some point defects and local irregularities of a perfect crystalline structure, which occur on the atomistic scale. The presented methodology can also be used for the exploration of other materials of technological interest, including monatomic systems and alloys.

It was found that the existing classical interatomic potentials often poorly describe highly-excited vibrational states when the system is far from the potential energy minimum, e.g., when a phase transition occurs in the system. The proper quantitative de-

scription of phase transitions in general and the melting process in particular by means of molecular dynamics simulations is a major scientific challenge that concerns metal materials, as well as inorganic and biomolecular systems. To overcome this problem, a new interatomic potential that is able to correctly reproduce both the melting temperature and the ground-state properties of different metals by means of classical molecular dynamics simulations has been proposed in this work. The new potential represents a modification of the widely used embedded-atom method-type potential. The applicability of the new potential to metals with different characteristics of the electronic structure, such as gold, platinum, titanium, and magnesium, was demonstrated. It was found that interatomic interactions at distances, exceeding the equilibrium distance by a characteristic vibration amplitude, are overestimated by conventional many-body potentials and should be corrected in order to reproduce the quantitatively correct value of the melting point.

We have analyzed electronic properties of nanometer-size nanoparticles made of gold, platinum, silver, and gadolinium; nanoparticles composed of these materials are of current interest for radiation therapy applications [8–12]. It is currently suggested that such nanoagents delivered to the tumor region can boost the production of secondary electrons near the target. The use of metal-based nanoparticles in combination with ionizing radiation may thus result in the local enhancement of the radiation damage of the tumor cells. Approaches that can enhance radiosensitivity within tumors relative to normal tissues have the potential to become advantageous radiotherapies [44].

In this work, we have provided a methodology for analyzing the dynamic response of nanoparticles of the experimentally relevant sizes, namely of about several nanometers, exposed to ionizing radiation. Because of a large number of constituent atoms (about $10^3 - 10^4$ atoms) and consequently high computational costs, the electronic properties of such systems can hardly be described by means of *ab initio* methods based on a quantum-mechanical treatment of electrons, and this analysis should rely on model approaches. By comparing the response of smaller systems (of about 1 nm size) calculated within the *ab initio*- and the model framework, this methodology has been validated and used to make predictions for the electron production in larger systems. We focused our attention on the production of low-energy electrons, having the kinetic energy from a few electronvolts to several tens of electronvolts. It is currently established that the low-energy secondary electrons of such energies play an important role in the nanoscale mechanisms of biological damage resulting from ionizing radiation [13–15].

The analysis performed has revealed that a significant increase in the number of the low-energy electrons emitted from nanometer-size noble metal nanoparticles arises from collective electron excitations formed in the systems. It was demonstrated that the dominating mechanisms of electron yield enhancement are related to the formation

of plasmons excited in a whole system and of atomic giant resonances formed due to excitation of valence d electrons in individual atoms of a nanoparticle. Plasmons, that is, collective excitations of delocalized valence electrons, dominate the spectra of electron emission from the noble metal nanoparticles in the energy range of about 1 – 10 eV. The leading mechanism of the increased electron production has been associated with the surface plasmon, whose contribution to the electron yield significantly exceeds that of the volume plasmon. For higher electron energies (of a few tens of eV), the main contribution to the electron yield arises from the collective excitation of $5d$ electrons in gold and platinum and of $4d$ in silver, localized on individual atoms.

The analysis of the plasmon contribution was performed within the model approach based on the plasmon resonance approximation [18–20]. To justify parameters of the model, photoabsorption spectra of several gold atomic clusters were calculated and compared with the spectra obtained by means of time-dependent density-functional theory. The accuracy of the results was proven by the comparison of *ab initio*-based spectra with well-established experimental data for atomic gold and the results of earlier *ab initio* calculations. Additional validation of the model was made by an extensive comparison with recent experimental data on photoionization and electron scattering from carbon fullerenes.

In this study, we have demonstrated that the number of the low-energy electrons produced by the noble metal nanoparticles of a given size (especially, those composed of gold and platinum) exceeds that produced by an equivalent volume of liquid water by more than an order of magnitude. Being embedded in a biological medium, the noble metal nanoparticles thus represent an important source of the low-energy electrons. This result supports the conclusions of the recent experimental studies [16, 17] which revealed the importance of gold nanoparticles in facilitating the production of low-energy electrons, which are responsible for a significant irreparable damage in biological systems. We found that the electron yield from a small gadolinium nanoparticle also exceeds the electron production from pure water medium but is lower than that from noble metal systems. This result generally corresponds to the conclusions of recent experimental studies [10] where it was found that the effect of gadolinium-based nanoparticles is less pronounced than that of platinum-based compounds, tested under the same conditions.

The utilized approach for evaluation of the electron production yield from sensitizing nanoparticles has an advantage as compared to other widely used approaches like track structure Monte Carlo simulations, which are utilized in the microdosimetric calculations (see, e.g., Ref. [210] and references therein). In most of the Monte Carlo simulations, the contribution of collective excitations, which play a significant role in the ionization of gold and other noble metal nanoparticles, is not accounted for. Apart

from that, the utilized methodology can be adopted for other projectiles, e.g. carbon ions, which are the most clinically used projectiles, besides protons.

The methodology for studying electronic properties of nanosystems was also used to make quantitative predictions for electron production by non-metal nanoparticles. We have demonstrated that due to a prominent collective response to an external electric field, carbon nanoparticles embedded in a biological medium also emit a large number of low-energy electrons. The number of emitted 10 eV electrons has been shown to be several times higher as compared to the case of liquid water. Assuming this, one may consider novel types of nanoparticles for radiotherapy applications, composed of a metal and an organic parts, where collective excitations will arise in both parts of the system. A proper choice of the constituents will allow one to tune the position of the resonance peaks in the ionization spectra of such systems and, subsequently, to cover a broader kinetic energy spectrum of electrons emitted from such nanoparticles thus enhancing effectiveness of their biomedical applications.

Directions for future research

One of the outcomes of this work is that the fundamental mechanisms of the enhanced production of low-energy electrons emitted from sensitizing nanoparticles have been suggested and explored. These findings will be utilized in future research aimed at a closer connection to radiobiological studies.

Recent experiments demonstrated that irradiation of cancer cells, loaded with metallic sensitizing nanoparticles, with photons or ion beams leads to an increase of cell killing [10, 147, 149]. Such studies are typically based on the analysis of survival curves, that is, the dependence of the clonogenic cell survival probability on the deposited dose (see Figure 6.1). These dependencies generally vary for different types of cells, cell cycle, and radiation modalities, and are the starting point for a treatment plan. It was also shown experimentally that injection of the nanoparticles into the tumor region leads to an increase of the relative biological effectiveness (RBE) of ionizing radiation [149]. This quantity is defined as the ratio of the dose delivered by photons to that delivered by different radiation modalities (e.g., electrons, protons, or heavier ions), leading to the same biological effect, such as the probability of an irradiated cell inactivation. All these results have demonstrated that radiosensitizing nanoparticles can enhance the radiation damage of the tumor cells and may thus increase the efficiency of radiotherapy. However, the full potential of the new techniques of radiotherapy can be realized only if the fundamental mechanisms leading to lethal cell damage under the action of ionizing radiation are well understood. The results obtained in this work will serve as a starting point for this further analysis.

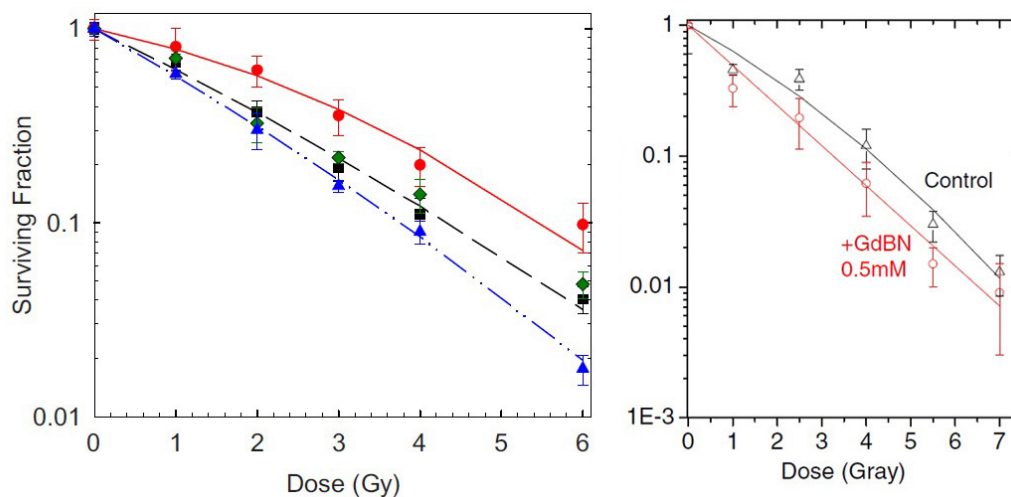


Figure 6.1: Left panel: Cell survival as a function of dose for DU145 human prostate cancer cells irradiated solely with x-rays (circles) and proton beams (squares), as well as for the cells irradiated with protons in the presence of gold nanoparticles (triangles). Right panel: Survival of U87 brain tumor cells (black triangles) and those loaded with Gd-based nanoparticles (red squares) irradiated by photons. The figures are adapted from Refs. [147, 149].

In particular, the calculated spectra of secondary electrons emitted by nanoparticles will be used as the input data for investigation of radiobiological effects by means of the MultiScale Approach to the physics of radiation damage with ions [13]. This approach has the goal of developing knowledge about biodamage at the nanoscale and molecular level and finding the relation between the characteristics of incident particles and the resultant biological damage. It is capable of predicting the biological damage based on the physical effects related to ionization of the medium, transport of secondary particles, chemical interactions, thermo-mechanical pathways of biodamage, and heuristic biological criteria for cell survival [13]. In the future work, this approach will be extended to include the physical effects due to the presence of nanoparticles in cells.

An important problem to be explored in future studies is how the presence of nanoparticles in cells affects the production and evolution of free radicals and reactive oxygen species. This research direction relies on the idea that the enhanced production of low-energy electrons by the nanoparticles should lead to an increase in the number of free radicals (in particular, OH^\bullet and O_2^-) and other reactive species, e.g., hydrogen peroxide H_2O_2 [211, 212]. By now, it is generally accepted that all these secondary species play an important role in the biological damage resulting from ionizing radiation [13, 213–215].

It is also argued that H_2O_2 can deliver damaging impacts onto the DNA in the cell nucleus from the radiation induced damages associated with the presence of nanoparticles in other cell compartments (see Figure 6.2). This issue might be important because

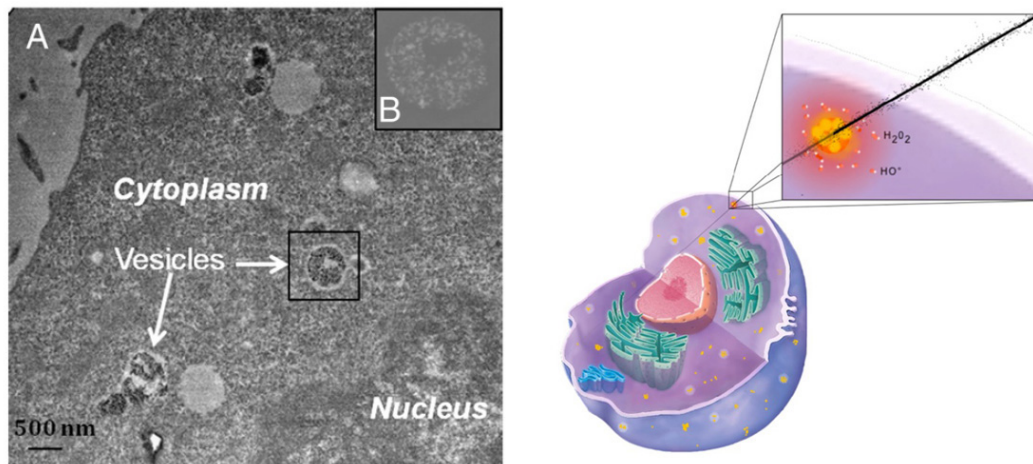


Figure 6.2: Left panel: Transmission electron microscopy image of gadolinium-based nanoparticles in mammalian CHO cells; Right panel: Scheme of a cell loaded with nanoparticles (in yellow) irradiated by an ion track (black line). The zoom highlights the production in the cytoplasm of a nano-size cluster composed of reactive oxygen species. The figures are adapted from Ref. [10].

a number of recent experiments demonstrated that the nanoparticles penetrate cells but are localized in the cytoplasm rather than in the cell nucleus [10,147]. Despite this, the presence of small (about 2 nm diameter) gold nanoparticles in the cell nucleus was also experimentally detected [12]. In the case if the sensitizing nanoparticles are localized in the nucleus, the low-energy electrons emitted from the nanoparticles can produce direct damage to DNA, e.g., by dissociative electron attachment [216].

The future research will hopefully give answers to the fundamental questions regarding the nanoscale mechanisms of radiation-induced damage of cells in the presence of nanoparticles. Understanding and exploiting the nanoscale processes that drive physical, chemical, and biological effects induced by ionizing radiation is within the scope of an ongoing international project, entitled “Advanced Radiotherapy, Generated by Exploiting Nanoprocesses and Technologies (ARGENT)”, supported by the European Commission [44].

Acknowledgements

First and foremost I would like to thank my supervisors, Prof. Dr. Andrey Solov'yov and Prof. Dr. Stefan Schramm, for their strong interest in the progress of this work and the immeasurable amount of guidance and support they have provided throughout my study. I would like to express my sincere gratitude to Dr. Andrei Korol, in a close collaboration with whom we did a substantial part of the present work, for his valuable comments and for numerous enlightening talks we had during this time.

While working on the thesis, I profited a lot from the opportunities to present and discuss my work-in-progress at various meetings, conferences and other events. I would like to thank Dr. Gennady Sushko, Dr. Eugene Surdutovich, Dr. Iliia Solov'yov, Christian Kexel and Dr. Pablo de Vera, with whom we have collaborated during the last years, for fruitful and stimulating discussions. My special thanks are extended to Oksana Verkhovtseva and Christian Kexel for helping me with the translation of the summary.

My work has been supported by the FP7 European project “Theoretical analysis, design and virtual testing of biocompatibility and mechanical properties of titanium-based nanomaterials (ViNaT)”, COST Action MP1002 “Nano-scale Insights into Ion Beam Cancer Therapy (Nano-IBCT)” and by the International training network “Advanced Radiotherapy, Generated by Exploiting Nanoprocesses and Technologies (ARGENT)” (GA 608163) in the frame of the FP7 European Programme. The opportunity of carrying out resource-demanding calculations at the Frankfurt Center for Scientific Computing is also gratefully acknowledged.

Most importantly, none of this would have been possible without the wonderful support of my family who has inspired me and provided constant encouragement during the entire period of working on the thesis.

Appendix A: Plasmon resonance approximation

The plasmon resonance approximation (PRA) [19,20,159] represents an effective method for evaluating the contribution of plasmons to the excitation/ionization spectra of atomic clusters and nanoparticles. It postulates that the dominating contribution to the cross section comes from collective electron excitations, while single-particle effects give much smaller contribution in the vicinity of the plasmon resonance. This Appendix gives a brief overview into the PRA formalism [159].

It is assumed that the considered system has spherical symmetry with a homogeneous distribution of the negative charge over the volume of the system. The equilibrium electron density distribution, $\rho_0(r)$, is expressed via the number N of delocalized electrons and the system's volume V :

$$\rho_0 = \begin{cases} N/V & , R_1 \leq r \leq R_2 \\ 0 & , r < R_1, r > R_2 . \end{cases} \quad (\text{A1})$$

In the general case, the volume of the system can be expressed as

$$V = \frac{4\pi}{3} (R_2^3 - R_1^3) = \frac{4\pi}{3} R_2^3 (1 - \xi^3) , \quad (\text{A2})$$

where R_1 and R_2 are the inner and the outer radii of the system, respectively, and $\xi = R_1/R_2 \leq 1$ is the ratio of the two radii.

The spherical-shell model defined by (A1) and (A2) is applicable for any spherically symmetric system with an arbitrary value of the ratio ξ . The limiting case of $\xi \rightarrow 0$ describes a solid nanoparticle with the electron density distribution over the full sphere of a radius R :

$$\rho_0(r) = \frac{N}{V} \Theta(R - r) . \quad (\text{A3})$$

In this limit, $R_1 \rightarrow 0$ and $R \equiv R_2$ so the cluster volume is $V = 4\pi R^3/3$.

The total electron density of the system in the point r and time t is introduced as $\rho(\mathbf{r}, t) = \rho_0(\mathbf{r}) + \delta\rho(\mathbf{r}, t)$, where $\rho_0(\mathbf{r})$ denotes the stationary distribution of the negative

charge in the point r , and $\delta\rho(\mathbf{r}, t)$ is the density variation caused by the interaction with an external electric field. The collective motion of the electron density is described using the Euler equation and the equation of continuity [19].

The Euler equation couples the acceleration, $d\mathbf{v}(\mathbf{r}, t)/dt$, of the electron density with the total electric field \mathbf{E} acting on the system at the point (\mathbf{r}, t) :

$$\frac{d\mathbf{v}(\mathbf{r}, t)}{dt} = \mathbf{E}(\mathbf{r}, t) . \quad (\text{A4})$$

The electric field \mathbf{E} includes both the external field acting on the system and the polarization contribution due to the variation of electron density $\delta\rho(\mathbf{r}, t)$:

$$\mathbf{E}(\mathbf{r}, t) = -\vec{\nabla}\phi(\mathbf{r}, t) - \vec{\nabla} \int \frac{\delta\rho(\mathbf{r}', t)}{|\mathbf{r} - \mathbf{r}'|} d\mathbf{r}' , \quad (\text{A5})$$

where $\phi(\mathbf{r}, t)$ is the scalar potential of the external field. Introducing (A5) in (A4) and evaluating the full time derivative of the vector \mathbf{v} , one obtains

$$\frac{\partial\mathbf{v}(\mathbf{r}, t)}{\partial t} + \left(\mathbf{v}(\mathbf{r}, t) \cdot \vec{\nabla}\right) \mathbf{v}(\mathbf{r}, t) = -\left(\vec{\nabla}\phi(\mathbf{r}, t)\right) - \vec{\nabla} \int \frac{\delta\rho(\mathbf{r}', t)}{|\mathbf{r} - \mathbf{r}'|} d\mathbf{r}' . \quad (\text{A6})$$

The potential of the external field is assumed to satisfy the wave equation and has the monochromatic dependence on t :

$$\phi(\mathbf{r}, t) = e^{i\omega t} \phi(\mathbf{r}) , \quad (\text{A7})$$

where $\phi(\mathbf{r})$ satisfies the equation

$$\Delta\phi(\mathbf{r}) + q^2 \phi(\mathbf{r}) = 0 \quad (\text{A8})$$

with q being the wave vector.

The motion of electron density in the system obeys the equation of continuity, which reads

$$\frac{\partial\rho(\mathbf{r}, t)}{\partial t} + \vec{\nabla} \cdot \left(\rho(\mathbf{r}, t) \mathbf{v}(\mathbf{r}, t)\right) = 0 . \quad (\text{A9})$$

Equations (A6) and (A9), being solved simultaneously, determine the variation of electron density $\delta\rho(\mathbf{r}, t)$ as well as its velocity $\mathbf{v}(\mathbf{r}, t)$. The second term on the left-hand side of equation (A6) can be neglected, which means physically that the external field causes only a small spatial inhomogeneity in the electron density distribution within the system.

The solutions of equations (A6) and (A9) are sought in the following form:

$$\begin{cases} \delta\rho(\mathbf{r}, t) = \delta\rho(\mathbf{r}) e^{i\omega t} \\ \mathbf{v}(\mathbf{r}, t) = \mathbf{v}(\mathbf{r}) e^{i\omega t} \end{cases} . \quad (\text{A10})$$

Substituting these expressions into (A6) and (A9) and performing some transformations with the simultaneous use of equation (A8) and $\Delta|\mathbf{r} - \mathbf{r}'|^{-1} = -4\pi\delta(\mathbf{r} - \mathbf{r}')$, one derives a set of the following linear equations:

$$\mathbf{v}(\mathbf{r}) = \frac{i}{\omega} \left[\vec{\nabla}\phi(\mathbf{r}) + \vec{\nabla} \int \frac{\delta\rho(\mathbf{r}')}{|\mathbf{r} - \mathbf{r}'|} d\mathbf{r}' \right] , \quad (\text{A11})$$

$$\begin{aligned} & \left(\omega^2 - 4\pi\rho_0(\mathbf{r}) \right) \delta\rho(\mathbf{r}) + \vec{\nabla}\rho_0(\mathbf{r}) \cdot \vec{\nabla} \int \frac{\delta\rho(\mathbf{r}')}{|\mathbf{r} - \mathbf{r}'|} d\mathbf{r}' \\ & = q^2 \rho_0(\mathbf{r}) \phi(\mathbf{r}) - \vec{\nabla}\rho_0(\mathbf{r}) \cdot \vec{\nabla}\phi(\mathbf{r}) . \end{aligned} \quad (\text{A12})$$

In the case of the spherically symmetric density distribution, $\rho_0(\mathbf{r}) = \rho_0(r)$, one can exclude angular variables from equations (A11) and (A12) by expanding functions $\phi(\mathbf{r})$, $\delta\rho(\mathbf{r})$, and $|\mathbf{r} - \mathbf{r}'|^{-1}$ into spherical harmonics and then integrating over spherical angles of the vector \mathbf{r} .

Performing some algebraic transformations [159], one obtains a general equation for the variation of electron density in an arbitrary spherically symmetric system:

$$\left(\omega^2 - 4\pi\rho_0(r) \right) \delta\rho_l(r) + 4\pi \frac{\rho_0'(r)}{\Pi_l^2} \int_0^\infty g_l(r, r') \delta\rho_l(r') dr' = q^2 \rho_0(r) \phi_l(r) - \rho_0'(r) \phi_l'(r) , \quad (\text{A13})$$

where $\phi_l(r)$ is the scalar potential, ω is the frequency of the external field, and the notation $\Pi_l = \sqrt{2l+1}$ is introduced. The function $g_l(r, r')$ is defined as:

$$g_l(r, r') = l \left(\frac{r}{r'} \right)^{l-1} \Theta(r' - r) - (l+1) \left(\frac{r'}{r} \right)^{l+2} \Theta(r - r') ,$$

where $\Theta(x)$ is the Heaviside step function

$$\Theta(x) = \begin{cases} 0 , & x < 0 \\ 1 , & x \geq 0 \end{cases} .$$

Consider a system with a homogeneous charge distribution over a spherical shell of a finite width $\Delta R = R_2 - R_1$. This means that the equilibrium electron density distribution, $\rho_0(r)$, is constant within the interval $R_1 \leq r \leq R_2$ and equals to zero if

otherwise:

$$\rho_0(r) = \rho_0 \Theta(r - R_1)\Theta(R_2 - r) , \quad (\text{A14})$$

where ρ_0 is defined by (A1). The derivative of the function $\rho_0(r)$ is given by

$$\rho'_0(r) = \rho_0 \left(\delta(r - R_1) - \delta(r - R_2) \right) , \quad (\text{A15})$$

where $\delta(x)$ is the delta-function. The solution of equation (A13) for such a system is sought in the following form:

$$\delta\rho_l(r) = \delta\rho_l(r)\Theta(r - R_1)\Theta(R_2 - r) + \sigma_l^{(1)}\delta(r - R_1) + \sigma_l^{(2)}\delta(r - R_2) , \quad (\text{A16})$$

where $\delta\rho_l(r)$ describes the volume density variation arising inside the finite-width spherical shell, and $\sigma_l^{(1,2)}$ are variations of the surface charge densities at the inner and the outer surfaces of the shell, respectively (see Figure 4.9). The volume density variation causes the formation of the volume plasmon, while the variations of the surface densities correspond to two surface plasmon modes.

Interaction with a uniform external field

The case of a uniform external field describes the interaction of a system with an electromagnetic field. It is assumed that the wavelength of electromagnetic radiation is much larger than the typical size of the system, i.e. the condition $\omega R \ll 1$ is fulfilled. This condition implies the validity of the dipole approximation. In this limit, the wave vector $q = 0$ and equation (A13) for the multipole variation of the electron density in a spherically symmetric system turns into the following one:

$$\left(\omega^2 - 4\pi\rho_0(r) \right) \delta\rho_l(r) + 4\pi \frac{\rho'_0(r)}{\Pi_l^2} \int_0^\infty g_l(r, r') \delta\rho_l(r') dr' = -\rho'_0(r) \phi'_l(r) . \quad (\text{A17})$$

Substituting (A14)-(A16) into equation (A17) and taking into account that in the dipole approximation the field intensity ϕ'_l does not depend on the spatial coordinate, $\phi'_l(R_1) = \phi'_l(R_2) \equiv \phi'_l$, one derives the following equation:

$$\begin{aligned} & (w - 1) \delta\rho_l(r) \Theta(r - R_1) \Theta(R_2 - r) \\ & + \left(w\sigma_l^{(1)} + I_l^{(1)} - \frac{l+1}{\Pi_l^2} \sigma_l^{(1)} + \frac{l}{\Pi_l^2} \sigma_l^{(2)} \xi^{l-1} \right) \delta(r - R_1) \\ & + \left(w\sigma_l^{(2)} + I_l^{(2)} + \frac{l+1}{\Pi_l^2} \sigma_l^{(1)} \xi^{l+2} - \frac{l}{\Pi_l^2} \sigma_l^{(2)} \right) \delta(r - R_2) \\ & = -\frac{\phi'_l}{4\pi} \delta(r - R_1) + \frac{\phi'_l}{4\pi} \delta(r - R_2) , \end{aligned} \quad (\text{A18})$$

where

$$w = \omega^2/\omega_p^2 \quad (\text{A19})$$

with ω_p being the volume plasmon frequency associated with the density ρ_0 (4.28), and

$$I_l^{(1)} = \frac{l}{\Pi_l^2} R_1^{l-1} \int_{R_1}^{R_2} \frac{\delta \varrho_l(x)}{x^{l-1}} dx, \quad I_l^{(2)} = \frac{l+1}{\Pi_l^2} \frac{1}{R_2^{l+2}} \int_{R_1}^{R_2} x^{l+2} \delta \varrho_l(x) dx. \quad (\text{A20})$$

Matching the terms of different types on the right- and the left-hand side of equation (A18), one obtains expressions which define the variations of the volume and the surface charge densities. The solution corresponding to the volume density variation reads as:

$$(w-1)\delta \varrho_l(r)\Theta(r-R_1)\Theta(R_2-r) = 0. \quad (\text{A21})$$

This means that no volume plasmon can arise in the system due to interaction with a uniform external field. The volume plasmon manifests itself only when the system interacts with a non-uniform external field, for instance, in collisions with charged particles. Thus, the total variation of electron density is described only by the surface density contributions:

$$\delta \rho_l(r) = \sigma_l^{(1)}\delta(r-R_1) + \sigma_l^{(2)}\delta(r-R_2), \quad (\text{A22})$$

which can be defined from the following system of coupled equations:

$$\begin{cases} \left(w - \frac{l+1}{\Pi_l^2}\right)\sigma_l^{(1)} + \frac{l}{\Pi_l^2}\xi^{l-1}\sigma_l^{(2)} = -\frac{\phi_l'}{4\pi} \\ \frac{l}{\Pi_l^2}\xi^{l+2}\sigma_l^{(1)} + \left(w - \frac{l}{\Pi_l^2}\right)\sigma_l^{(2)} = \frac{\phi_l'}{4\pi} \end{cases}. \quad (\text{A23})$$

The determinant of the system (A23) is $\Delta = (w-w_{1l})(w-w_{2l})$, where w_{1l} and w_{2l} are the roots of the secular equation $\Delta = 0$:

$$\begin{aligned} w_{1l} &= \frac{1}{2} \left(1 - \frac{1}{2l+1} \sqrt{1 + 4l(l+1)\xi^{2l+1}} \right) \\ w_{2l} &= \frac{1}{2} \left(1 + \frac{1}{2l+1} \sqrt{1 + 4l(l+1)\xi^{2l+1}} \right) \end{aligned}. \quad (\text{A24})$$

Variation of the surface charge densities, $\sigma_l^{(1,2)}$, results in the formation of two coupled modes of surface plasmon oscillations [159,177–179]. Frequencies of the symmetric, $\omega_l^{(s)}$, and the antisymmetric, $\omega_l^{(a)}$, surface plasmons of multipolarity l are given by expression (4.27). In the symmetric mode, the charge densities of the two surfaces oscillate in phase, while in the antisymmetric mode they are out of phase (see Figure 4.9). Since

only dipole excitations may arise in the system due to interaction with the external electromagnetic field, the case of interest is $l = 1$. The expression for the resonant frequencies of the surface plasmons is then reduced to Eq. (4.6).

The cross section of photoionization by a single photon is given by the general expression:

$$\sigma_\gamma(\omega) = \frac{4\pi\omega}{c} \text{Im} \alpha(\omega) , \quad (\text{A25})$$

where $\alpha(\omega)$ is the dynamic polarizability. This quantity is related to the external electric field $E(\omega)$ and the induced dipole moment, which is defined as:

$$d(\omega) = \frac{\sqrt{4\pi}}{3} \int_0^\infty r^3 \delta\rho_1(r) dr . \quad (\text{A26})$$

The quantity $\delta\rho_1(r)$ defines the electron density variation (A22) created by the dipole mode of surface plasmon oscillations.

One can demonstrate that the dipole polarizability $\alpha(\omega)$ can be expressed in the following form [159]:

$$\alpha(\omega) \propto N \left(\frac{1}{\omega^2 - \omega^{(s)2}} + \frac{1}{\omega^2 - \omega^{(a)2}} \right) , \quad (\text{A27})$$

where N is the number of delocalized electrons in the system. This expression clearly shows that the photoionization cross section is defined by the two surface plasmons with the frequencies $\omega^{(s)}$ and $\omega^{(a)}$.

The final expression for the photoionization cross section within the PRA is obtained by accounting for damping of the plasmon oscillations due to the decay of the collective mode to the incoherent sum of single-electron excitations. This is done by introducing the finite widths, $\Gamma^{(s)}$ and $\Gamma^{(a)}$, of the plasmon resonances and making the following substitutions in the right-hand side of (A27):

$$\frac{1}{\omega^2 - \omega^{(s,a)2}} \longrightarrow \frac{1}{\omega^2 - \omega^{(s,a)2} + i\omega\Gamma^{(s,a)}} . \quad (\text{A28})$$

Taking the imaginary parts of the polarizability produces:

$$\text{Im} \frac{1}{\omega^2 - \omega^{(s,a)2} + i\omega\Gamma^{(s,a)}} \longrightarrow \frac{\omega\Gamma^{(s,a)}}{(\omega^2 - \omega^{(s,a)2})^2 + \omega^2\Gamma^{(s,a)2}} . \quad (\text{A29})$$

Thereby, the final formula for the photoionization cross section within the PRA is

written in the following form [159, 180]:

$$\sigma(\omega) = \frac{4\pi\omega^2}{c} \left(\frac{N_s \Gamma^{(s)}}{(\omega^2 - \omega^{(s)^2})^2 + \omega^2 \Gamma^{(s)^2}} + \frac{N_a \Gamma^{(a)}}{(\omega^2 - \omega^{(a)^2})^2 + \omega^2 \Gamma^{(a)^2}} \right), \quad (\text{A30})$$

where N_s, N_a are the number of delocalized electrons which are involved in each plasmon mode.

Interaction with a non-uniform external field

In the case of the interaction with a non-uniform electric field, e.g., in collisions with charged particles, the multipole variation of the electron density (A16) is defined as the solution of a general equation (A13).

Carrying out the transformations, similar to those described above for the case of a uniform external field, one derives the following equation:

$$\begin{aligned} & (w-1)\delta\varrho_l(r)\Theta(r-R_1)\Theta(R_2-r) \\ & + \left(w\sigma_l^{(1)} + I_l^{(1)} - \frac{l+1}{\Pi_l^2}\sigma_l^{(1)} + \frac{l}{\Pi_l^2}\sigma_l^{(2)}\xi^{l-1} \right) \delta(r-R_1) \\ & + \left(w\sigma_l^{(2)} + I_l^{(2)} + \frac{l+1}{\Pi_l^2}\sigma_l^{(1)}\xi^{l+2} - \frac{l}{\Pi_l^2}\sigma_l^{(2)} \right) \delta(r-R_2) \\ & = q^2 \frac{\phi_l(r)}{4\pi} \Theta(r-R_1)\Theta(R_2-r) - \frac{1}{4\pi} \left(\phi_l'(R_1)\delta(r-R_1) - \phi_l'(R_2)\delta(r-R_2) \right). \end{aligned} \quad (\text{A31})$$

Matching the terms of different types on the left- and the right-hand side of equation (A31), one obtains three equations: one for the volume density variation and the other two for the variation of the surface charge densities. The solution of equation (A31) corresponding to the volume density variation reads as:

$$\delta\varrho_l(r) = \frac{q^2}{w-1} \frac{\phi_l(r)}{4\pi}, \quad (\text{A32})$$

and the density variation due to the surface plasmon modes is

$$\sigma_l(r) = \sigma_l^{(1)}\delta(r-R_1) + \sigma_l^{(2)}\delta(r-R_2). \quad (\text{A33})$$

The quantities $\sigma_l^{(1)}$ and $\sigma_l^{(2)}$ satisfy the following system of coupled equations:

$$\begin{cases} \left(w - \frac{l+1}{\Pi_l^2} \right) \sigma_l^{(1)} + \frac{l}{\Pi_l^2} \xi^{l-1} \sigma_l^{(2)} = F_1 \\ \frac{l}{\Pi_l^2} \xi^{l+2} \sigma_l^{(1)} + \left(w - \frac{l}{\Pi_l^2} \right) \sigma_l^{(2)} = F_2 \end{cases}, \quad (\text{A34})$$

where

$$F_{1,2} = \mp \frac{\phi'_l(R_{1,2})}{4\pi} - I_l^{(1,2)} \quad (\text{A35})$$

and the functions $I_l^{(1,2)}$ were defined above in (A20).

Solutions of the system (A34) are given by the following expression:

$$\begin{aligned} \sigma_l^{(1)} &= \frac{1}{\Delta} \left[F_1 w - \frac{l}{\Pi_l^2} (F_1 + \xi^{l-1} F_2) \right] \equiv \frac{\mathcal{F}_1}{\Delta} \\ \sigma_l^{(2)} &= \frac{1}{\Delta} \left[F_2 w - \frac{l+1}{\Pi_l^2} (F_2 + \xi^{l+2} F_1) \right] \equiv \frac{\mathcal{F}_2}{\Delta} \end{aligned} \quad , \quad (\text{A36})$$

where Δ is the determinant of the system.

Finally, using (A32) and (A36) in (A16), one obtains the expression which defines the multipole variation of electron density in a spherically symmetric hollow system under the action of the multipole component $\phi_l(r)$ of the external field:

$$\begin{aligned} \delta\rho_l(r) &= \frac{q^2}{w-1} \frac{\phi_l(r)}{4\pi} \Theta(r-R_1)\Theta(R_2-r) \\ &+ \frac{\mathcal{F}_1}{\Delta} \delta(r-R_1) + \frac{\mathcal{F}_2}{\Delta} \delta(r-R_2) . \end{aligned} \quad (\text{A37})$$

The first term leads to the formation of the volume plasmon, while the two other terms are responsible for the formation of two coupled modes of the surface plasmon.

Appendix B: Basis sets in quantum-chemical calculations

This Appendix provides an overview of some basis principles which the performed quantum-chemical calculation are based on. A more detailed description of *ab initio* methods is presented, for instance, in Refs. [217–219].

In quantum-chemical calculations, the many-electron wave function of a system, Ψ_e , is expressed via a set of single-electron wave functions (which are also sometimes called molecular orbitals), ϕ_i . In order to define the orbitals, one needs to solve a system of single-particle equations using the Hartree-Fock method or within the framework of density-functional theory (see Section 2.3). The major part of *ab initio* calculations described in this work have been based on DFT methods, where a system of Kohn-Sham equations [53] is solved to find the molecular orbitals ϕ_i :

$$\left[-\frac{1}{2}\nabla^2 + v_n(\mathbf{r}) + \int \frac{\rho(\mathbf{r}')}{|\mathbf{r} - \mathbf{r}'|} d\mathbf{r}' + v_{xc}(\mathbf{r}) \right] \phi_i(\mathbf{r}) = \varepsilon_i \phi_i(\mathbf{r}) . \quad (\text{B1})$$

The first term on the left-hand side of the above equation represents the kinetic energy of the electron i , $v_n(\mathbf{r})$ described its interaction with the nuclei, the third term defines the potential of electron-electron Coulomb interaction, and $v_{xc}(\mathbf{r})$ is the exchange-correlation potential.

When carrying out quantum-chemical calculations with the use of Gaussian 09 package [107] or with some other modern quantum chemistry codes, the molecular orbitals ϕ_i are approximated by a linear combination of predefined single-electron functions χ_μ , also known as basis functions:

$$\phi_i = \sum_{\mu=1}^N c_{\mu i} \chi_\mu , \quad (\text{B2})$$

where $c_{\mu i}$ are the molecular orbital expansion coefficients, and the parameter N defines the number of basis functions used in the calculation [115]. The constructed basis set consists of a limited number of functions centered on each atomic nucleus of a molecular system.

At an early stage of development of computational quantum chemistry, so-called

Slater-type orbitals (STOs) were used as basis functions. The radial component of such orbitals decays exponentially when moving away from the nucleus the given orbital is centered on:

$$\chi(\zeta, n, l, m; r, \vartheta, \varphi) = Nr^{n-1} e^{-\zeta r} Y_{lm}(\vartheta, \varphi) . \quad (\text{B3})$$

Here N is a normalization prefactor, n, l and m are the principal, orbital, and magnetic quantum numbers, respectively, and r is the distance from the nucleus. The parameter ζ denotes a so-called orbital exponent that defines an effective nucleus charge appearing due to partial screening of the nucleus by electrons. It was shown later that STOs can be expressed as a linear combination of so-called Gaussian-type orbitals (or Gaussians, GTOs); the radial component of a GTO is defined by a Gaussian distribution, $\chi(r) \sim e^{-\alpha r^2}$. Since a basis set composed of GTOs is more convenient for calculating complex many-center integrals, the STO-based basis sets are not widely used nowadays in quantum-chemical calculations.

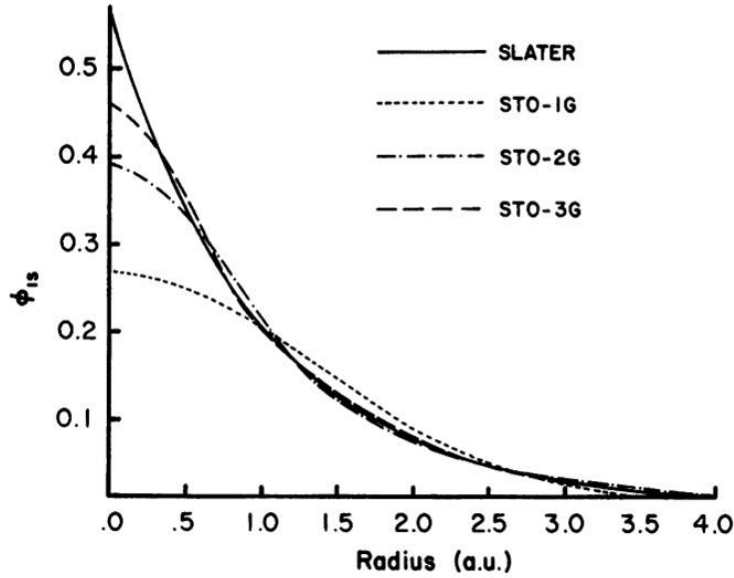


Figure B1: Comparison of the quality of the least-squares fit of a $1s$ Slater orbital ($\zeta = 1.0$) by means of a single (STO-1G), as well as a combination of two (STO-2G) and three (STO-3G) Gaussian-type orbitals. The illustration is adapted from Ref. [218].

In spite of convenience in calculating many-center integrals, a single GTO or even a combination of several GTOs cannot describe properly the electronic wave function near the nucleus (see Figure B1). Thus, one has to utilize the so-called contracted Gaussian-type orbitals (CGTOs), where each basis function χ_μ is a linear combination of several primitive Gaussian functions:

$$\chi_\mu = \sum_p d_{\mu p} g_p , \quad (\text{B4})$$

and the contraction coefficients $d_{\mu p}$ are predefined for a given basis set. A primitive Gaussian function $g_p \equiv g(\alpha; x, y, z)$ centered on atom a is defined as follows:

$$g(\alpha; x, y, z) = N x^i y^j z^k e^{-\alpha r^2}, \quad (\text{B5})$$

where i , j and k are non-negative integers, α is a positive orbital exponent, (x, y, z) are Cartesian coordinates with the origin at a , and N is the normalization factor. The choice of the parameters i , j and k defines the type of primitive Gaussian functions, namely, the sum of the powers, $i + j + k$, should be equal to the orbital quantum number l of an atomic orbital. Hence, different combinations of i , j and k are used to denote s , p , d , and f -orbitals (see Table 6.1).

Table 6.1: Presentation of different atomic orbitals via the corresponding Gaussian primitives.

	$i + j + k$	$g(\alpha; x, y, z)$
s -orbital	0	$e^{-\alpha r^2}$
p -orbital	1	$\{x, y, z\} e^{-\alpha r^2}$
d -orbital	2	$\{x^2, y^2, z^2\} e^{-\alpha r^2},$ $\{xy, yz, xz\} e^{-\alpha r^2}$

When describing chemical bonds in complex molecular systems, a standard basis set, that is, a combination of primitive Gaussian orbitals, is usually augmented with other functions. The most common addition to basis sets is the addition of polarization functions. The radial part of such functions has one additional node, i.e. these functions are one unit higher in angular momentum than what are present in the ground state of the atom. For instance, the only basis function located on a hydrogen atom in a minimal basis set is a function approximating the $1s$ atomic orbital. Including polarization means that a p -function is also added to the basis set. This allows molecular orbitals involving the hydrogen atoms to be more asymmetric with respect to the nucleus (see Figure B2). Similarly, d -type functions can be added to a basis set with valence p orbitals, f -functions to a basis set with d -type orbitals, etc.

In general, polarization functions significantly improve the description of molecular geometries, i.e., they produce more accurate values of bond lengths and angles [219]. However, one should note that adding d -functions to, for instance, a carbon atom, does not imply that d -orbitals become occupied or that d -orbitals provide a significant contribution to the bonding of the carbon atom. In this case, the presence of the d -orbital functions improves the description of the electron density around the carbon atom and its bonding characteristics. Indeed, adding polarization functions allows one to achieve a more accurate representation of bonding between atoms, because the presence of the bonded atom makes the energetic environment of the electrons spherically asymmetric.

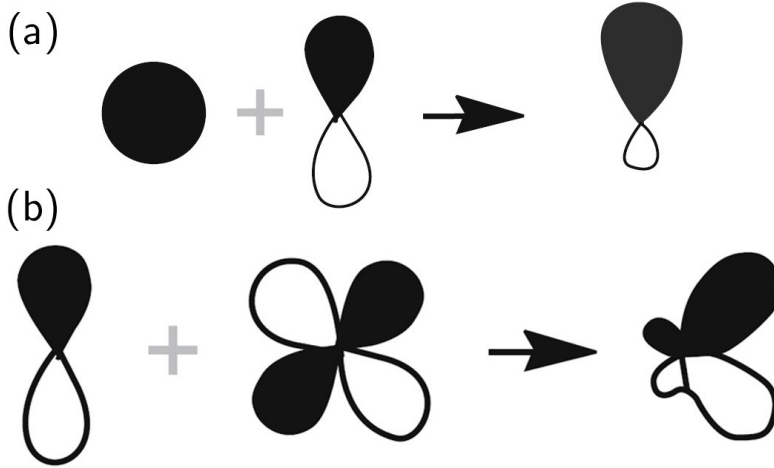


Figure B2: Distortion of an s -orbital due to the inclusion of a p -type polarization function (a) and of a p -orbital due to the inclusion of d -orbitals (b). The figure is adapted from Ref. [219].

Sometimes the standard basis sets are also augmented by so-called diffuse functions which are characterized by a very small value of the orbital exponent α and are used to better describe the long-range "tail" of the atomic orbitals. These functions represent Gaussian primitives which decay slowly with increasing the distance from the nucleus. They do not influence significantly geometries of covalently bonded species but improve the description of energetics associated with weak interactions (e.g., van der Waals interactions, H-bonding, or electron affinities).

A number of quantum chemistry computer packages, e.g., QuantumEspresso [171], rely on another representation of molecular orbitals ϕ_i . Contrary to the above-described localized basis sets, in this approach single-electron wave functions are represented by a linear combination of plane waves,

$$\phi_i(\mathbf{r}) = \frac{1}{\sqrt{\Omega}} \sum_{\mathbf{G}} \tilde{\psi}_i(\mathbf{G}) e^{i\mathbf{G}\cdot\mathbf{r}}, \quad (\text{B6})$$

where Ω is the volume of a unit cell, defined by the unit vectors $\{\mathbf{a}_1, \mathbf{a}_2, \mathbf{a}_3\}$ as $\Omega = \mathbf{a}_1 \cdot (\mathbf{a}_2 \times \mathbf{a}_3)$, \mathbf{G} is the reciprocal lattice vector, and the wave planes $e^{i\mathbf{G}\cdot\mathbf{r}}$ are determined from the periodicity constraint:

$$e^{i\mathbf{G}\cdot(\mathbf{r}+\mathbf{R})} = e^{i\mathbf{G}\cdot\mathbf{r}}. \quad (\text{B7})$$

with $\mathbf{R} = n_1\mathbf{a}_1 + n_2\mathbf{a}_2 + n_3\mathbf{a}_3$ being the translation vector. Expansion into plane waves allows one to calculate accurately electronic structure of periodic crystals. However, such an expansion can also be utilized successfully for the calculation of amorphous structures and finite systems, such as atomic clusters and nanoparticles. From a math-

emathical viewpoint, plane waves form a complete basis set, i.e. the accuracy of the calculation increases with increasing the number of basis functions. Thus, the convergence of a numerical solution and the accuracy of calculations are governed by a kinetic energy cutoff value for plane waves used in the expansion. Only the reciprocal lattice vectors whose kinetic energy lower than a predefined maximum cutoff energy, $\frac{1}{2}|\mathbf{G}|^2 < E_{\text{cut}}$, are kept in the expansion, while the rest of the coefficients are set to zero. One should note that plane waves are not centered on the atomic nuclei, and the accuracy of the wave function description within the plane-wave approach will be the same at every point of the system.

Plane-wave basis sets are often used in combination with an "effective core potential" or pseudopotential, so that the plane waves are only used to describe the valence charge density. This is because core electrons are localized very close to the atomic nuclei, resulting in large wave function and density gradients near the nuclei which are not easily described by a plane-wave basis set. For an accurate description of atomic core electrons, one has to consider a significant number of plane waves in the expansion, that means, to use a very high energy cutoff. Hence, pseudopotentials are commonly used to describe core electrons. Such pseudopotentials are usually constructed based on the solution of the Schrödinger equation or the relativistic Dirac equation for isolated atoms.

Appendix C: Electron production from individual atomic excitations

This Appendix presents the derivation of Eq. (4.33) that is utilized to evaluate the contribution of individual atomic excitations in electron production from metal nanoparticles under ion impact. This analytical expression relates the cross section of photoionization, σ_γ , with that of inelastic scattering in the dipole approximation, $d\sigma/d\Delta\varepsilon$.

Photoionization

The operator describing the interaction of a photon with an electron can be written in the following form (the atomic system of units, $m_e = |e| = \hbar = 1$, is utilized):

$$V_\gamma = \sum_{i=1}^N e^{i\mathbf{k}\cdot\mathbf{r}} (\mathbf{e} \cdot \nabla_i) , \quad (\text{C1})$$

where \mathbf{e} is the polarization vector of the photon, \mathbf{r}_i is the position vector of the electron, $\nabla_i \equiv -i\partial/\partial\mathbf{r}_i$, and N is the number of electrons in the system. In the dipole approximation, the photon momentum k can be neglected, so that $e^{i\mathbf{k}\cdot\mathbf{r}} \approx 1$ and the interaction of a many-electron system with a photon reduces to:

$$V_\gamma \equiv d_\gamma^V = (\mathbf{e} \cdot \nabla_i) . \quad (\text{C2})$$

In this representation, the interaction operator is written in the so-called velocity form because $-i\partial/\partial\mathbf{r}_i$ corresponds to the velocity of the electron in the target. Along with this form, the dipole operator can also be written in the so-called length form:

$$d_\gamma^L = \omega (\mathbf{e} \cdot \mathbf{r}_i) . \quad (\text{C3})$$

The matrix element $M_{n0}^{L,V}$, which is determined by the following integral, describes the interaction of a many-electron system with a photon:

$$M_{n0}^{L,V}(\omega) = \int \Psi_0^*(\mathbf{r}_1, \dots, \mathbf{r}_N) d_\gamma^{L,V}(\omega) \Psi_n(\mathbf{r}_1, \dots, \mathbf{r}_N) d\mathbf{r}_1 \dots d\mathbf{r}_N , \quad (\text{C4})$$

where $\Psi_0(\mathbf{r}_1, \dots, \mathbf{r}_N)$ and $\Psi_n(\mathbf{r}_1, \dots, \mathbf{r}_N)$ are the wave functions of the initial and the final states, respectively.

The total photoionization cross section $\sigma_\gamma^{L,V}(\omega)$ is given by

$$\sigma_\gamma^{L,V}(\omega) = \frac{4\pi^2}{\omega c} \int |M_{n0}^{L,V}(\omega)|^2 \delta(\varepsilon_0 + \omega - \varepsilon_n) d\rho(\varepsilon_n), \quad (\text{C5})$$

and in the length form, it is expressed as (the superscript "L" is omitted for brevity)

$$\sigma_\gamma(\omega) = \frac{4\pi^2\omega}{c} \int |(\mathbf{e} \cdot \mathbf{r})_{n0}|^2 \delta(\varepsilon_0 + \omega - \varepsilon_n) d\rho(\varepsilon_n). \quad (\text{C6})$$

The differential cross section with respect to the emission angle is derived as follows (linear polarization is assumed):

$$\begin{aligned} d\sigma_\gamma(\omega) &= \frac{4\pi^2\omega}{c} |(\mathbf{e} \cdot \mathbf{r})_{n0}|^2 \delta(\varepsilon_0 + \omega - \varepsilon_n) \frac{d\mathbf{p}_n}{(2\pi)^3} \\ &= \frac{4\pi^2\omega}{c} |(\mathbf{e} \cdot \mathbf{r})_{n0}|^2 \delta(\varepsilon_0 + \omega - \varepsilon_n) \frac{p_n^2 dp_n d\Omega_{\mathbf{p}_n}}{(2\pi)^3} \\ &= \frac{\omega p_n}{2\pi c} |(\mathbf{e} \cdot \mathbf{r})_{n0}|^2 \delta(\varepsilon_0 + \omega - \varepsilon_n) d\varepsilon_n d\Omega_{\mathbf{p}_n} \\ &= \frac{\omega p_n}{2\pi c} \Big|_{p_n=\sqrt{2(\varepsilon_0+\omega)}} |(\mathbf{e} \cdot \mathbf{r})_{n0}|^2 d\Omega_{\mathbf{p}_n}. \end{aligned} \quad (\text{C7})$$

Directing the z -axis along \mathbf{e} , one can write:

$$\frac{d\sigma_\gamma(\omega)}{d\Omega_{\mathbf{p}_n}} = \frac{\omega p_n}{2\pi c} |z_{n0}|^2 \quad (\text{C8})$$

with $p_n = \sqrt{2(\varepsilon_0 + \omega)}$.

Inelastic scattering

The atomic transition $0 \rightarrow n$ is due to the operator

$$V = \frac{1}{|\mathbf{r} - \mathbf{r}_a|} = \int \frac{4\pi}{Q^2} e^{i(\mathbf{r}-\mathbf{r}_a)\cdot\mathbf{Q}} \frac{d\mathbf{Q}}{(2\pi)^3}. \quad (\text{C9})$$

Hence, the transition matrix element, calculated with the plane-wave Born approximation, reads:

$$\begin{aligned}
M_{n0} &= \langle \mathbf{p}_2, n | V | 0, \mathbf{p}_1 \rangle = \int \frac{4\pi}{Q^2} \frac{d\mathbf{Q}}{(2\pi)^3} \langle \mathbf{p}_2 | e^{i\mathbf{Q}\cdot\mathbf{r}} | \mathbf{p}_1 \rangle \langle n | e^{-i\mathbf{r}_a\cdot\mathbf{Q}} | 0 \rangle \\
&= \frac{4\pi}{Q^2} \frac{d\mathbf{Q}}{(2\pi)^3} \int d\mathbf{r} e^{i(\mathbf{p}_1 - \mathbf{p}_2 + \mathbf{Q})\cdot\mathbf{r}} (e^{-i\mathbf{r}_a\cdot\mathbf{Q}})_{n0} \\
&= \frac{4\pi}{Q^2} \frac{d\mathbf{Q}}{(2\pi)^3} (2\pi)^3 \delta(\mathbf{q} + \mathbf{Q}) (e^{-i\mathbf{r}_a\cdot\mathbf{Q}})_{n0} = \frac{4\pi}{q^2} (e^{-i\mathbf{r}_a\cdot\mathbf{q}})_{n0} , \tag{C10}
\end{aligned}$$

where $\mathbf{q} = \mathbf{p}_1 - \mathbf{p}_2$.

The differential cross section reads:

$$d\sigma = \frac{2\pi}{v_1} \delta(\varepsilon_0 + \varepsilon_1 - \varepsilon_n - \varepsilon_2) |M_{n0}|^2 \frac{d\mathbf{p}_n}{(2\pi)^3} \frac{d\mathbf{p}_2}{(2\pi)^3} \rightarrow \frac{2\pi}{v_1} |M_{n0}|^2 \frac{d\Omega_{\mathbf{p}_n} p_n}{(2\pi)^3} \frac{d\Omega_{\mathbf{p}_2} v_2 d\varepsilon_2}{(2\pi)^3}. \tag{C11}$$

Recalling that $d\Omega_{\mathbf{p}_2} = q dq d\phi_2 / v_1 v_2$ and assuming the validity of the dipole approximation for the Coulomb interaction, i.e., $e^{-i\mathbf{q}\cdot\mathbf{r}_a} \approx 1 - i\mathbf{q}\cdot\mathbf{r}_a$ (this also leads to a substitution $q_{\max} \rightarrow R^{-1}$), one proceeds

$$\begin{aligned}
\frac{d^2\sigma}{d\varepsilon_2 d\Omega_{\mathbf{p}_n}} &= \frac{p_n}{v_1^2 (2\pi)^5} \int_{q_{\min}}^{q_{\max}} q dq \int_0^{2\pi} d\phi_2 |M_{n0}|^2 \\
&\approx \frac{p_n}{v_1^2 (2\pi)^5} \int_{q_{\min}}^{R^{-1}} q dq \frac{(4\pi)^2}{q^4} \int_0^{2\pi} d\phi_2 \left| \underbrace{(\mathbf{q}\cdot\mathbf{r})}_{=qz} \right|_{n0}^2 \\
&= \frac{4p_n}{v_1^2 (2\pi)^2} |z_{n0}|^2 \int_{q_{\min}}^{R^{-1}} \frac{dq}{q} = \frac{4p_n}{v_1^2 (2\pi)^2} |z_{n0}|^2 \ln\left(\frac{1}{q_{\min} R}\right). \tag{C12}
\end{aligned}$$

Introducing $\omega \equiv \varepsilon_1 - \varepsilon_2$ and approximating

$$\frac{d^2\sigma}{d\varepsilon_2 d\Omega_{\mathbf{p}_n}} = \frac{4p_n}{v_1^2 (2\pi)^2} |z_{n0}|^2 \ln\left(\frac{v_1}{\omega R}\right) = \frac{2c}{\pi\omega v_1^2} \frac{d\sigma_\gamma}{d\Omega_{\mathbf{p}_n}} \ln\left(\frac{v_1}{\omega R}\right). \tag{C13}$$

This equation establishes the relation with the photoionization cross section. Integration over the emission angles produces:

$$\frac{d\sigma}{d\varepsilon_2} = \frac{2c}{\pi\omega v_1^2} \sigma_\gamma \ln\left(\frac{v_1}{\omega R}\right). \tag{C14}$$

Bibliography

- [1] *Nanomaterials and Nanochemistry*, edited by C. Bréchnignac, P. Houdy, and M. Lahmani (Springer-Verlag, Berlin, Heidelberg, 2007)
- [2] *Handbook of Nanoscience, Engineering, and Technology* (3rd ed.), edited by W. A. Goddard III, D. Brenner, S. E. Lyshevski, and G. J. Iafrate (CRC Press, Boca Raton, FL, 2012)
- [3] H. Rafii-Tabar and G. A. Mansoori, Interatomic potential models for nanostructures, in *Encyclopedia of Nanoscience and Nanotechnology*, vol. 4, edited by H. S. Nalwa (American Scientific Publishers, Valencia, CA, 2004), p. 231
- [4] http://ec.europa.eu/environment/chemicals/nanotech/faq/definition_en.htm
- [5] J. E. Gagner, S. Shrivastava, X. Qian, J. S. Dordick, and R. W. Siegel, Engineering nanomaterials for biomedical applications requires understanding the nano-bio interface: a perspective, *J. Phys. Chem. Lett.* **3**, 3149–3158 (2012)
- [6] E. C. Dreaden, A. M. Alkilany, X. Huang, C. J. Murphy, and M. A. El-Sayed, The golden age: gold nanoparticles for biomedicine, *Chem. Soc. Rev.* **41**, 2740–2779 (2012)
- [7] D. A. Giljohann, D. S. Seferos, W. L. Daniel, M. D. Massich, P. C. Patel, and C. A. Mirkin, Gold nanoparticles for biology and medicine, *Angew. Chem. Int. Ed.* **49**, 3280–3294 (2010)
- [8] E. Porcel, S. Liehn, H. Remita, N. Usami, K. Kobayashi, Y. Furusawa, C. Le Sech, and S. Lacombe, Platimun nanoparticles: a promising material for future cancer therapy? *Nanotechnology* **21**, 085103 (2010)
- [9] P. Liu, Z. Huang, Z. Chen, *et al.*, Silver nanoparticles: a novel radiation sensitizer for glioma?, *Nanoscale* **5**, 11829–11836 (2013)
- [10] E. Porcel, O. Tillement, F. Lux, *et al.*, Gadolinium-based nanoparticles to improve the hadrontherapy performances, *Nanomed. Nanotech. Biol. Med.* **10**, 1601–1608 (2014)

- [11] S. J. McMahon, W. B. Hyland, M. F. Muir, *et al.*, Biological consequences of nanoscale energy deposition near irradiated heavy atom nanoparticles, *Sci. Rep.* **1**, 18 (2011); Corrigendum: *ibid.* **3**, 1725 (2013)
- [12] K. T. Butterworth, J. A. Coulter, S. Jain, *et al.*, Evaluation of cytotoxicity and radiation enhancement using 1.9 nm gold particles: potential application for cancer therapy, *Nanotechnology* **21**, 295101 (2010)
- [13] E. Surdutovich and A. V. Solov'yov, Multiscale approach to the physics of radiation damage with ions, *Eur. Phys. J. D* **68**, 353 (2014)
- [14] B. Boudaiffa, P. Cloutier, D. Hunting, M. A. Huels, and L. Sanche, Resonant formation of DNA strand breaks by low-energy (3 to 20 eV) electrons, *Science* **287**, 1658–1660 (2000)
- [15] M. A. Huels, B. Boudaiffa, P. Cloutier, D. Hunting, and L. Sanche, Single, double, and multiple double strand breaks induced in DNA by 3–100 eV electrons, *J. Am. Chem. Soc.* **125**, 4467–4477 (2003)
- [16] F. Xiao, Y. Zheng, P. Cloutier, Y. He, D. Hunting, and L. Sanche, On the role of low-energy electrons in the radiosensitization of DNA by gold nanoparticles, *Nanotechnology* **22**, 465101 (2011)
- [17] Y. Zheng, D. J. Hunting, P. Ayotte, and L. Sanche, Radiosensitization of DNA by gold nanoparticles irradiated with high-energy electrons, *Radiat. Res.* **169**, 19–27 (2008); Erratum: *ibid.* **169**, 481–482 (2008)
- [18] L. G. Gerchikov, A. N. Ipatov, A. V. Solov'yov, and W. Greiner, Excitation of multipole plasmon resonances in clusters by fast electron impact, *J. Phys. B: At. Mol. Opt. Phys.* **31**, 3065–3077 (1998)
- [19] J.-P. Connerade, and A. V. Solov'yov, Formalism for multiphoton plasmon excitation in jellium clusters, *Phys. Rev. A* **66**, 013207 (2002)
- [20] A. V. Solov'yov, Plasmon excitations in metal clusters and fullerenes, *Int. J. Mod. Phys. B* **19**, 4143–4184 (2005)
- [21] G. Sushko, A. Verkhovtsev, Ch. Kexel, A. V. Korol, S. Schramm, and A. V. Solov'yov, Reconciling simulated melting and ground-state properties of metals with a modified embedded-atom method potential, *J. Phys.: Condens. Matter* **28**, 145201 (2016)

-
- [22] A. V. Verkhovtsev, M. Hanauske, A. V. Yakubovich, and A. V. Solov'yov, Characterization of small pure and Ni-doped titanium clusters: ab initio versus classical approaches, *Comput. Mater. Sci.* **76**, 80–88 (2013)
- [23] G. B. Sushko, A. V. Verkhovtsev, and A. V. Solov'yov, Validation of classical force fields for the description of thermo-mechanical properties of transition metal materials, *J. Phys. Chem. A* **118**, 8426–8436 (2014)
- [24] A. V. Verkhovtsev, A. V. Korol, and A. V. Solov'yov, Electron production by sensitizing gold nanoparticles irradiated by fast ions, *J. Phys. Chem. C* **119**, 11000–11013 (2015)
- [25] A. V. Verkhovtsev, A. V. Korol, and A. V. Solov'yov, Revealing the mechanism of the low-energy electron yield enhancement from sensitizing nanoparticles, *Phys. Rev. Lett.* **114**, 063401 (2015)
- [26] A. V. Verkhovtsev, S. McKinnon, P. de Vera, E. Surdutovich, S. Guatelli, A. V. Korol, A. Rosenfeld, and A. V. Solov'yov, Comparative analysis of the secondary electron yield from carbon nanoparticles and pure water medium, *Eur. Phys. J. D* **69**, 116 (2015)
- [27] A. V. Verkhovtsev, A. V. Korol, A. V. Solov'yov, P. Bolognesi, A. Ruocco, and L. Avaldi, Interplay of the volume and surface plasmons in the electron energy loss spectra of C_{60} , *J. Phys. B: At. Mol. Opt. Phys.* **45**, 141002 (2012)
- [28] P. Bolognesi, A. Ruocco, L. Avaldi, A. V. Verkhovtsev, A. V. Korol, and A. V. Solov'yov, Collective excitations in the electron energy loss spectra of C_{60} , *Eur. Phys. J. D* **66**, 254 (2012)
- [29] A. V. Verkhovtsev, A. V. Korol, and A. V. Solov'yov, Quantum and classical features of the photoionization spectrum of C_{60} , *Phys. Rev. A* **88**, 043201 (2013)
- [30] C. Bartels, C. Hock, J. Huwer, R. Kuhnen, J. Schwöbel, and B. von Issendorff, Probing the angular momentum character of the valence orbitals of free sodium nanoclusters, *Science* **323**, 1323–1327 (2009)
- [31] H. W. Kroto, J. R. Heath, S. C. O'Brien, R. F. Curl, and R. E. Smalley, C_{60} : buckminsterfullerene, *Nature* **318**, 162–163 (1985)
- [32] W. D. Knight, K. Clemenger, W. A. de Heer, W. A. Saunders, M. Y. Chou, and M. L. Cohen, Electronic shell structure and abundances of sodium clusters, *Phys. Rev. Lett.* **52**, 2141–2143 (1983)

- [33] W. A. de Heer, The physics of simple metal clusters: experimental aspects and simple models, *Rev. Mod. Phys.* **65**, 611–676 (1993)
- [34] M. Brack, The physics of simple metal clusters: self-consistent jellium model and semiclassical approaches, *Rev. Mod. Phys.* **65**, 677–732 (1993)
- [35] A. V. Korol and A. V. Solov'yov, Atomic cluster collisions. Editorial, *Eur. Phys. J. D* **67**, 1 (2013)
- [36] P. M. Dinh, P.-G. Reinhard, and E. Suraud, *An Introduction to Cluster Science* (Wiley-VCH Verlag, Weinheim, Germany, 2013)
- [37] *Latest Advances in Atomic Clusters Collision: Fission, Fusion, Electron, Ion and Photon Impact*, edited by J.-P. Connerade and A. V. Solov'yov (Imperial College Press, Coven Garten, London, UK, 2004)
- [38] *Proceedings of the Fourth International Symposium "Atomic Cluster Collisions: Structure and Dynamics from the Nuclear to the MesoBioNano Scale" (ISACC 2009)*, edited by A. V. Solov'yov and E. Surdutovich, *AIP Conf. Proc.* **1197** (2009)
- [39] O. V. Salata, Applications of nanoparticles in biology and medicine, *J. Nanobiotechnology* **2**, 3 (2004)
- [40] S. K. Murthy, Nanoparticles in modern medicine: state of the art and future challenges, *Int. J. Nanomed.* **2**, 129–141 (2007)
- [41] D. M. Herold, I. J. Das, C. C. Stobbe, R. V. Iyer, and J. D. Chapman, Gold microspheres: a selective technique for producing biologically effective dose enhancement, *Int. J. Radiat. Biol.* **76**, 1357–1364 (2000)
- [42] J. J. Hainfeld, D. N. Slatkin, and H. M. Smilowitz, The use of gold nanoparticles to enhance radiotherapy in mice, *Phys. Med. Biol.* **49**, N309–N315 (2004)
- [43] X.-D. Zhang, Z. Luo, J. Chen, *et al.*, Ultrasmall glutathione-protected gold nanoclusters as next generation radiotherapy sensitizers with high tumor uptake and high renal clearance, *Sci. Rep.* **5**, 8669 (2015)
- [44] FP7 Initial Training Network Project "Advanced Radiotherapy, Generated by Exploiting Nanoprocesses and Technologies" (ARGENT), <http://www.itn-argent.eu>
- [45] L. Mishnaevsky Jr., E. Levashov, R. Z. Valiev, *et al.*, Nanostructured titanium-based materials for medical implants: modeling and development, *Mater. Sci. Eng. R* **81**, 1–19 (2014)

-
- [46] J. R. Davis, *Handbook of Materials for Medical Devices* (ASM International, Russell Township, OH, 2003)
- [47] H. Stallforth and P. Revell, *Materials for Medical Engineering*, vol. 2 (Wiley-VCH Verlag, Weinheim, Germany, 2005)
- [48] X. Huang, G. J. Ackland, and K. M. Rabe, Crystal structures and shape-memory behaviour of NiTi, *Nature Mater.* **2**, 307–311 (2003)
- [49] O. Prymak, D. Bogdanski, M. Koller, *et al.*, Morphological characterization and *in vitro* biocompatibility of a porous nickel-titanium alloy, *Biomaterials* **26**, 5801–5807 (2005)
- [50] Y. Mishin, M. Asta, and J. Li, Atomistic modeling of interfaces and their impact on microstructure and properties, *Acta Mater.* **58**, 1117–1151 (2010)
- [51] C. Froese Fischer, General Hartree-Fock program, *Comput. Phys. Commun.* **43**, 355–365 (1987)
- [52] P. Hohenberg and W. Kohn, Inhomogeneous electron gas, *Phys. Rev.* **136**, B864–B871 (1964)
- [53] W. Kohn and L. J. Sham, Self-consistent equations including exchange and correlation effects, *Phys. Rev.* **140**, A1133–A1138 (1965)
- [54] E. Runge and E. K. U. Gross, Density-functional theory for time-dependent systems, *Phys. Rev. Lett.* **52**, 997–1000 (1984)
- [55] M. Born and J. R. Oppenheimer, Zur Quantentheorie der Molekeln, *Ann. Phys.* **389**, 457–484 (1927)
- [56] R. Car and M. Parrinello, Unified approach for molecular dynamics and density-functional theory, *Phys. Rev. Lett.* **55**, 2471–2474 (1985)
- [57] D. Marx and J. Hutter, Ab initio molecular dynamics: theory and implementation, in *Modern Methods and Algorithms of Quantum Chemistry*, edited by J. Grotendorst (John von Neumann Institute for Computing, Jülich, Germany, 2000), pp. 301–449
- [58] G. Zhao, J. R. Perilla, E. L. Yufenyuy, *et al.*, Mature HIV-1 capsid structure by cryo-electron microscopy and all-atom molecular dynamics, *Nature* **497**, 643–646 (2013)

- [59] P. Vashishta, R. K. Kalia, and A. Nakano, Multimillion atom simulations of dynamics of oxidation of an aluminum nanoparticle and nanoindentation on ceramics, *J. Phys. Chem. B* **110**, 3727–3733 (2006)
- [60] R. Salomon-Ferrer, A. W. Götz, D. Poole, S. Le Grand, and R. C. Walker, Routine microsecond molecular dynamics simulations with AMBER on GPUs. 2. Explicit solvent particle mesh Ewald, *J. Chem. Theory Comput.* **9**, 3878–3888 (2013)
- [61] I. A. Solov'yov, A. V. Yakubovich, P. V. Nikolaev, I. Volkovets, and A. V. Solov'yov, MBN Explorer – a universal program for multiscale computer simulations of complex molecular structure and dynamics, *J. Comput. Chem.* **33**, 2412–2439 (2012)
- [62] A. V. Verkhovtsev, A. V. Yakubovich, G. B. Sushko, M. Hanauske, and A. V. Solov'yov, Molecular dynamics simulations of the nanoindentation process of titanium crystal, *Comput. Mater. Sci.* **76**, 20–26 (2013)
- [63] A. V. Yakubovich, G. Sushko, S. Schramm, and A. V. Solov'yov, Kinetics of liquid-solid phase transition in large nickel clusters, *Phys. Rev. B* **88**, 035438 (2013)
- [64] E. Surdutovich, A. V. Yakubovich, and A. V. Solov'yov, Biodamage via shock waves initiated by irradiation with ions, *Sci. Rep.* **3**, 1289 (2013)
- [65] L. D. Landau and E. M. Lifshitz, *Quantum Mechanics: Non-Relativistic Theory* (3rd ed.), Course of Theoretical Physics, Vol. 3 (Butterworth-Heinemann, 1976)
- [66] I. Mayer, *Simple Theorems, Proofs, and Derivations in Quantum Chemistry* (Springer Science+Business Media, New York, 2003)
- [67] A. S. Davydov, *Quantum Mechanics* (2nd ed.) (Pergamon Press, 1976)
- [68] B. J. Alder and T. E. Wainwright, Studies in molecular dynamics. I. General method, *J. Chem. Phys.* **31**, 459–466 (1959)
- [69] A. Rahman, Correlations in the motion of atoms in liquid argon, *Phys. Rev.* **136**, A405–A411 (1964)
- [70] T. D. Kühne, Second generation Car-Parrinello molecular dynamics, *WIREs Comput. Mol. Sci.* **4**, 391–406 (2014)
- [71] A. D. MacKerell, D. Bashford, R. L. Bellott, *et al.*, All-atom empirical potential for molecular modeling and dynamics studies of proteins, *J. Phys. Chem. B* **102**, 3586–3616 (1998)

-
- [72] J. C. Phillips, R. Braun, W. Wang, *et al.*, Scalable molecular dynamics with NAMD, *J. Comput. Chem.* **26**, 1781–1802 (2005)
- [73] G. B. Sushko, I. A. Solov'yov, A. V. Verkhovtsev, S. N. Volkov, and A. V. Solov'yov, Studying chemical reactions in biological systems with MBN Explorer: implementation of molecular mechanics with dynamical topology, *Eur. Phys. J. D* **70**, 12 (2016)
- [74] M. S. Daw and M. I. Baskes, Embedded-atom method: derivation and application to impurities, surfaces, and other defects in metals, *Phys. Rev. B* **29**, 6443–6453 (1984)
- [75] M. S. Daw, S. M. Foiles, and M. I. Baskes, The embedded-atom method: a review of theory and applications, *Mater. Sci. Rep.* **9**, 251–310 (1993)
- [76] M. W. Finnis and J. E. Sinclair, A simple empirical N -body potential for transition metals, *Philos. Mag. A* **50**, 45–55 (1984)
- [77] R. P. Gupta, Lattice relaxation at a metal surface, *Phys. Rev. B* **23**, 6265–6270 (1981)
- [78] M. Born and J. E. Mayer, Zur Gittertheorie der Ionenkristalle, *Z. Physik* **75**, 1–18 (1932)
- [79] D. Tomanek, A. A. Aligia, and C. A. Balseiro, Calculation of elastic strain and electronic effects on surface segregation, *Phys. Rev. B* **32**, 5051–5056 (1985)
- [80] S. Lundqvist and N. H. March, *Theory of the Inhomogeneous Electron Gas* (Plenum Press, New York, 1983)
- [81] S. H. Vosko, L. Wilk, and M. Nusair, Accurate spin-dependent electron liquid correlation energies for local spin density calculations: a critical analysis, *Can. J. Phys.* **58**, 1200–1211 (1980)
- [82] J. P. Perdew and A. Zunger, Self-interaction correction to density-functional approximations for many-electron systems, *Phys. Rev. B* **23**, 5048–5079 (1981)
- [83] J. P. Perdew and Y. Wang, Accurate and simple analytic representation of the electron-gas correlation energy, *Phys. Rev. B* **45**, 13244–13249 (1992)
- [84] J. P. Perdew, J. A. Chevary, S. H. Vosko, *et al.*, Atoms, molecules, solids, and surfaces: applications of the generalized gradient approximation for exchange and correlation, *Phys. Rev. B* **46**, 6671–6687 (1992); Erratum: *ibid.* **48**, 4978 (1993)

- [85] J. P. Perdew, K. Burke, and M. Ernzerhof, Generalized gradient approximation made simple, *Phys. Rev. Lett.* **77**, 3865–3868 (1996)
- [86] A. D. Becke, Density-functional thermochemistry. III. The role of exact exchange, *J. Chem. Phys.* **98**, 5648–5652 (1993)
- [87] J. Tao, J. P. Perdew, V. N. Staroverov, and G. E. Scuseria, Climbing the density functional ladder: nonempirical metageneralized gradient approximation designed for molecules and solids, *Phys. Rev. Lett.* **91**, 146401 (2003)
- [88] R. G. Parr and W. Yang, *Density-Functional Theory of Atoms and Molecules* (Oxford University Press, Oxford, 1994)
- [89] D. M. Ceperley and B. J. Alder, Ground state of the electron gas by a stochastic method, *Phys. Rev. Lett.* **45**, 566–569 (1980)
- [90] X. Xu and W. A. Goddard III, The extended Perdew-Burke-Ernzerhof functional with improved accuracy for thermodynamic and electronic properties of molecular systems, *J. Chem. Phys.* **121**, 4068–4082 (2004)
- [91] G. K. H. Madsen, Functional form of the generalized gradient approximation for exchange: The PBE α functional, *Phys. Rev. B* **75**, 195108 (2007)
- [92] J. P. Perdew and W. Yue, Accurate and simple density functional for the electronic exchange energy: generalized gradient approximation, *Phys. Rev. B* **33**, 8800–8802 (1986); Erratum: *ibid.* **40**, 3399 (1989)
- [93] W. Ekardt, Work function of small metal particles: self-consistent spherical jellium-background model, *Phys. Rev. B* **29**, 1558–1564 (1984)
- [94] B. Walker and R. Gebauer, Ultrasoft pseudopotentials in time-dependent density-functional theory, *J. Chem. Phys.* **127**, 164106 (2007)
- [95] R. Kubo, Electronic properties of metallic fine particles. I., *J. Phys. Soc. Jpn.* **17**, 975–986 (1962)
- [96] M. Thiele and S. Kümmel, Reconstructing the adiabatic exchange-correlation kernel of time-dependent density-functional theory, *Phys. Rev. A* **80**, 012514 (2009)
- [97] B. Walker, A. M. Saitta, R. Gebauer, and S. Baroni, Efficient approach to time-dependent density-functional perturbation theory for optical spectroscopy, *Phys. Rev. Lett.* **96**, 113001 (2006)

-
- [98] D. Rocca, R. Gebauer, Y. Saad, and S. Baroni, Turbo charging time-dependent density-functional theory with Lanczos chains, *J. Chem. Phys.* **128**, 154105 (2008)
- [99] M. E. Casida, in *Recent Advances in Density Functional Methods, Part I*, edited by D. P. Chong (World Scientific, Singapore, 1995), Vol. 1, p. 155
- [100] D. Rocca, *Time-dependent density functional perturbation theory: New algorithms with applications to molecular spectra*, Ph.D. thesis, Scuola Internazionale Superiore di Studi Avanzati (2007)
- [101] *Advances in Chemical Physics*, vol. 137, edited by S. A. Rice (John Wiley & Sons, 2008)
- [102] J. A. Alonso, Electronic and atomic structure, and magnetic properties of transition-metal clusters, *Chem. Rev.* **100**, 637–677 (2000)
- [103] M. D. Morse, Clusters of transition-metal atoms, *Chem. Rev.* **86**, 1049–1109 (1986)
- [104] S. Y. Wang, W. H. Duan, D. L. Zhao, and C. Y. Wang, First-principles study of the stability of the icosahedral Ti_{13} , Ti_{13}^{-1} , and Ti_{13}^{+1} clusters, *Phys. Rev. B* **65**, 165424 (2002)
- [105] M. Pereiro, D. Baldomir, M. Iglesias, C. Rosales, and M. Castro, Model potential density functional study of small cobalt clusters, Co_n , $n = 3$, *Int. J. Quant. Chem.* **81**, 422–430 (2001)
- [106] C. Sosa, J. Andzelm, B. C. Elkin, E. Wimmer, K. D. Dobbs, and D. A. Dixon, A local density functional study of the structure and vibrational frequencies of molecular transition-metal compounds, *J. Phys. Chem.* **96**, 6630–6636 (1992)
- [107] M. J. Frisch, G. W. Trucks, H. B. Schlegel, *et al.*, *Gaussian 09*, Revision A.01 (Gaussian, Wallingford, CT, 2009)
- [108] W. S. Lai and B. X. Liu, Lattice stability of some Ni–Ti alloy phases versus their chemical composition and disordering, *J. Phys.: Condens. Matter* **12**, L53–L60 (2000)
- [109] J.-O. Joswig and M. Springborg, Size-dependent structural and electronic properties of Ti_n clusters ($n \leq 100$), *J. Phys.: Condens. Matter* **19**, 106207 (2007)
- [110] T. J. Dhilip Kumar, P. F. Weck, and N. Balakrishnan, Evolution of small Ti clusters and the dissociative chemisorption of H_2 on Ti, *J. Phys. Chem. C* **111**, 7494–7500 (2007)

- [111] J. Du, X. Sun, J. Chen, and G. Jiang, The changes in the geometrical, electronic and magnetic properties of titanium clusters as one titanium atom is substituted by boron, *J. Phys. B: At. Mol. Opt. Phys.* **43**, 205103 (2010)
- [112] S.-Y. Wang, J.-Z. Yu, H. Mizuseki, J.-A. Yan, Y. Kawazoe, and C.-Y. Wang, First-principles study of the electronic structures of icosahedral Ti_N ($N = 13, 19, 43, 55$) clusters, *J. Chem. Phys.* **120**, 8463–8468 (2004)
- [113] N. S. Venkataramanan, R. Sahara, H. Mizuseki, and Y. Kawazoe, Titanium-doped nickel clusters TiNi_n ($n = 1 - 12$): geometry, electronic, magnetic, and hydrogen adsorption properties, *J. Phys. Chem. A* **114**, 5049–5057 (2010)
- [114] M. Sakurai, K. Watanabe, K. Sumiyama, and K. Suzuki, Magic numbers in transition metal (Fe, Ti, Zr, Nb, and Ta) clusters observed by time-of-flight mass spectrometry, *J. Chem. Phys.* **111**, 235–238 (1999)
- [115] I. A. Solov'yov, A. V. Solov'yov, and W. Greiner, Structure and properties of small sodium clusters, *Phys. Rev. A* **65**, 053203 (2002)
- [116] A. Lyalin, I. A. Solov'yov, A. V. Solov'yov, and W. Greiner, Evolution of the electronic and ionic structure of Mg clusters with increase in cluster size, *Phys. Rev. A* **67**, 063203 (2003)
- [117] C. Kittel, *Introduction to Solid State Physics*, 7th edition (Wiley, New York, 1995)
- [118] M. Fuchs, M. Bockstedte, E. Pehlke, and M. Scheffler, Pseudopotential study of binding properties of solids within generalized gradient approximations: the role of core-valence exchange correlation, *Phys. Rev. B* **57**, 2134–2145 (1998)
- [119] M. Fuchs, J. L. F. Da Silva, C. Stampfl, J. Neugbauer, and M. Scheffler, Cohesive properties of group-III nitrides: a comparative study of all-electron and pseudopotential calculations using the generalized gradient approximation, *Phys. Rev. B* **65**, 245212 (2002)
- [120] S. L. Dudarev, G. A. Botton, S. Y. Savrasov, C. J. Humphreys, and A. P. Sutton, Electron-energy-loss spectra and the structural stability of nickel oxide: an LSDA+U study, *Phys. Rev. B* **57**, 1505–1509 (1998)
- [121] J. L. F. Da Silva, C. Stampfl, and M. Scheffler, Converged properties of clean metal surfaces by all-electron first-principles calculations, *Surf. Sci.* **600**, 703–715 (2006)

-
- [122] V. Rosato, M. Guillope, and B. Legrand, Thermodynamical and structural properties of f.c.c. transition metals using a simple tight-binding model, *Philos. Mag. A* **59**, 321–326 (1989)
- [123] F. Cleri and V. Rosato, Tight-binding potentials for transition metals and alloys, *Phys. Rev. B* **48**, 22–33 (1993)
- [124] A. P. Sutton and J. Chen, Long-range Finnis-Sinclair potentials, *Philos. Mag. Lett.* **61**, 139–146 (1990)
- [125] L. J. Lewis, P. Jensen, and J.-L. Barrat, Melting, freezing, and coalescence of gold nanoclusters, *Phys. Rev. B* **56**, 2248–2257 (1997)
- [126] S. Ryu, C. R. Weinberger, M. I. Baskes, and W. Cai, Improved modified embedded-atom method potentials for gold and silicon, *Modelling Simul. Mater. Sci. Eng.* **17**, 075008 (2009)
- [127] Y.-M. Kim, B.-J. Lee, and M. I. Baskes, Modified embedded-atom method interatomic potentials for Ti and Zr, *Phys. Rev. B* **74**, 014101 (2006)
- [128] G. B. Sushko, A. V. Verkhovtsev, A. V. Yakubovich, S. Schramm, and A. V. Solov'yov, Molecular dynamics simulation of self-diffusion processes in titanium in bulk material, on grain junctions and on surface, *J. Phys. Chem. A* **118**, 6685–6691 (2014)
- [129] M. Dzugutov, Glass formation in a simple monatomic liquid with icosahedral inherent local order, *Phys. Rev. A* **46**, 2984–2987 (1992)
- [130] D. Frenkel and B. Smit, *Understanding Molecular Simulation: From Algorithms to Applications*, 2nd ed. (Academic Press, San Diego, CA, 2001)
- [131] V. O. Shestopal, Specific heat and vacancy formation in titanium at high temperatures, *Fiz. Tverd. Tela* **7**, 3461 (1966) (Engl. Transl. *Sov. Phys. Solid State* **7**, 2798–2799 (1966))
- [132] E. Hashimoto, E. A. Smirnov, and T. Kino, Temperature dependence of the Doppler-broadened lineshape of positron annihilation in α -Ti, *J. Phys. F: Met. Phys.* **14**, L215–L217 (1984)
- [133] O. Le Bacq, F. Willaime, and A. Pasturel, Unrelaxed vacancy formation energies in group-IV elements calculated by the full-potential linear muffin-tin orbital method: Invariance with crystal structure, *Phys. Rev. B* **59**, 8508–8515 (1999)

- [134] A. T. Raji, S. Scandolo, R. Mazzarello, S. Nsengiyumva, M. Härting, and D. T. Britton, Ab initio pseudopotential study of vacancies and self-interstitials in HCP titanium, *Philos. Mag.* **89**, 1629–1645 (2009)
- [135] C. Janot, D. Molléjac, and B. George, Vacancy-formation energy and entropy in magnesium single crystals, *Phys. Rev. B* **2**, 3088–3098 (1970)
- [136] C. G. Johansen, H. Huang, and T.-M. Lu, Diffusion and formation energies of adatoms and vacancies on magnesium surfaces, *Comput. Mater. Sci.* **47**, 121–127 (2009)
- [137] P. Tzanetakis, J. Hillairet, and G. Revel, The formation energy of vacancies in aluminium and magnesium, *Phys. Status Solidi B* **75**, 433–439 (1976)
- [138] Ph. Jund, R. Viennois, C. Colinet, G. Hug, M. Fèvre, and J.-C. Tédénac, Lattice stability and formation energies of intrinsic defects in Mg₂Si and Mg₂Ge via first principles simulations, *J. Phys.: Condens. Matter* **25**, 035403 (2013)
- [139] P. Jongenburger, Energy of formation of vacancies in copper and gold, *Phys. Rev.* **106**, 66 (1957)
- [140] H.-E. Schaefer, Investigation of thermal equilibrium vacancies in metals by positron annihilation, *Phys. Status Solidi A* **102**, 47–65 (1987)
- [141] T. R. Mattsson and A. E. Mattsson, Calculating the vacancy formation energy in metals: Pt, Pd, and Mo, *Phys. Rev. B* **66**, 214110 (2002)
- [142] P. Pawlow, Über die Abhängigkeit des Schmelzpunktes von der Oberflächenenergie eines festen Körpers, *Z. Phys. Chem.* **65**, 1–35 (1909)
- [143] Y. Qi, T. Çağın, W. L. Johnson, and W. A. Goddard III, Melting and crystallization in Ni nanoclusters: the mesoscale regime, *J. Chem. Phys.* **115**, 385–394 (2001)
- [144] F. A. Lindemann, Über die Berechnung molekularer Eigenfrequenzen, *Z. Physik* **11**, 609–615 (1910)
- [145] W. Chen and J. Zhang, Using nanoparticles to enable simultaneous radiation and photodynamic therapies for cancer treatment, *J. Nanosci. Nanotechnol.* **6**, 1159–1166 (2006)
- [146] J.-K. Kim, S.-J. Seo, K.-H. Kim, *et al.*, Therapeutic application of metallic nanoparticles combined with particle-induced X-ray emission effect, *Nanotechnology* **21**, 425102 (2010)

-
- [147] L. Štefančíková, E. Porcel, P. Eustache, *et al.*, Cell localisation of gadolinium-based nanoparticles and related radiosensitising efficacy in glioblastoma cells, *Cancer Nanotech.* **5**, 6 (2014)
- [148] S. Jain, J. A. Coulter, A. R. Hounsell, *et al.*, Cell-specific radiosensitization by gold nanoparticles at megavoltage radiation energies, *Int. J. Radiat. Oncol. Biol. Phys.* **79**, 531–539 (2011)
- [149] J. C. Polf, L. F. Bronk, W. H. P. Driessen, W. Arap, R. Pasqualini, and M. Gillin, Enhanced relative biological effectiveness of proton radiotherapy in tumor cells with internalized gold nanoparticles, *Appl. Phys. Lett.* **98**, 193702 (2011)
- [150] D. Schardt, T. Elsässer, and D. Schulz-Ertner, Heavy-ion tumor therapy: physical and radiobiological benefits, *Rev. Mod. Phys.* **82**, 383–425 (2010)
- [151] J. S. Loeffler and M. Durante, Charged particle therapy – optimization, challenges and future directions, *Nat. Rev. Clin. Oncol.* **10**, 411–424 (2013)
- [152] U. Kreibig and M. Vollmer, *Optical Properties of Metal Clusters* (Springer-Verlag, Berlin-Heidelberg, 1995)
- [153] C. Bréchnac, Ph. Cahuzac, F. Carlier, and J. Leygnier, Collective excitation in closed-shell potassium cluster ions, *Chem. Phys. Lett.* **164**, 433–437 (1989)
- [154] K. Selby, M. Vollmer, J. Masui, V. Kresin, W. A. de Heer, and W. D. Knight, Surface plasma resonances in free metal clusters, *Phys. Rev. B* **40**, 5417–5427 (1989)
- [155] J.-P. Connerade, J. M. Esteva, and R. C. Karnatak, *Giant Resonances in Atoms, Molecules, and Solids* (Plenum Press, New York, 1987)
- [156] C. Bréchnac and J.-P. Connerade, Giant resonances in free atoms and in clusters, *J. Phys. B: At. Mol. Opt. Phys.* **27**, 3795–3828 (1994)
- [157] I. V. Hertel, H. Steger, J. de Vries, B. Weisser, C. Menzel, B. Kamke, and W. Kamke, Giant plasmon excitation in free C₆₀ and C₇₀ molecules studied by photoionization, *Phys. Rev. Lett.* **68**, 784–787 (1992)
- [158] D. L. Ederer, Photoionization of the 4d electrons in xenon, *Phys. Rev. Lett.* **13**, 760–761 (1964)
- [159] A. V. Verkhovtsev, A. V. Korol, and A. V. Solov'yov, Formalism of collective excitations in fullerenes, *Eur. Phys. J. D* **66**, 253 (2012)

- [160] L. G. Gerchikov, A. N. Ipatov, and A. V. Solov'yov, Many-body treatment of electron inelastic scattering on metal clusters, *J. Phys. B: At. Mol. Opt. Phys.* **30**, 5939–5959 (1997)
- [161] L. G. Gerchikov, A. N. Ipatov, R. G. Polozkov, and A. V. Solov'yov, Surface- and volume-plasmon excitations in electron inelastic scattering on metal clusters, *Phys. Rev. A* **62**, 043201 (2000)
- [162] L. G. Gerchikov, A. V. Solov'yov, J.-P. Connerade, and W. Greiner, Scattering of electrons on metal clusters and fullerenes, *J. Phys. B: At. Mol. Opt. Phys.* **30**, 4133–4161 (1997)
- [163] L. G. Gerchikov, P. V. Efimov, V. M. Mikoushkin, and A. V. Solov'yov, Diffraction of fast electrons on the fullerene C₆₀ molecule, *Phys. Rev. Lett.* **81**, 2707–2710 (1998)
- [164] S. Bulusu, X. Li, L. S. Wang, and X. C. Zeng, Evidence of hollow golden cages, *Proc. Natl. Acad. Sci. U.S.A.* **103**, 8326–8330 (2006)
- [165] J. Li, X. Li, H.-J. Zhai, and L.-S. Wang, Au₂₀: a tetrahedral cluster, *Science* **299**, 864–867 (2003)
- [166] M. P. Johansson, D. Sundholm, and J. Vaara, Au₃₂: a 24-carat golden fullerene, *Angew. Chem. Int. Ed.* **43**, 2678–2681 (2004)
- [167] X. Gu, M. Ji, S. H. Wei, and X. G. Gong, Au_N clusters ($N = 32, 33, 34, 35$): cagelike structures of pure metal atoms, *Phys. Rev. B* **70**, 205401 (2004)
- [168] Y. Gao and X. C. Zeng, Au₄₂: an alternative icosahedral golden fullerene cage, *J. Am. Chem. Soc.* **127**, 3698–3699 (2005)
- [169] W. J. Stevens, M. Krauss, H. Basch, and P. G. Jasien, Relativistic compact effective potentials and efficient, shared-exponent basis-sets for the 3rd-row, 4th-row, and 5th-row atoms, *Can. J. Chem.* **70**, 612–630 (1992)
- [170] O. B. Malcioğlu, R. Gebauer, D. Rocca, and S. Baroni, TurboTDDFT – a code for the simulation of molecular spectra using the Liouville-Lanczos approach to time-dependent density-functional perturbation theory, *Comput. Phys. Commun.* **182**, 1744–1754 (2011)
- [171] P. Giannozzi, S. Baroni, N. Bonini, *et al.*, QUANTUM ESPRESSO: a modular and open-source software project for quantum simulations of materials, *J. Phys.: Condens. Matter* **21**, 395502 (2009)

-
- [172] D. Vanderbilt, Soft self-consistent pseudopotentials in a generalized eigenvalue formalism, *Phys. Rev. B* **41**, 7892–7895 (1990)
- [173] J. C. Idrobo, W. Walkosz, S. F. Yip, S. Ögüt, J. Wang, and J. Jellinek, Static polarizabilities and optical absorption spectra of gold clusters (Au_n , $n = 2 - 14$ and 20) from first principles, *Phys. Rev. B* **76**, 205422 (2007)
- [174] C. M. Aikens and G. C. Schatz, TDDFT studies of absorption and SERS spectra of pyridine interacting with Au_{20} , *J. Phys. Chem. A* **110**, 13317–13324 (2006)
- [175] B. L. Henke, E. M. Gullikson, and J. C. Davis, X-ray interactions: photoabsorption, scattering, transmission, and reflection at $E = 50 - 30,000$ eV, $Z = 1 - 92$, *At. Data Nucl. Data Tables* **54**, 181–342 (1993)
- [176] U. Fano, Effects of configuration interaction on intensities and phase shifts, *Phys. Rev.* **124**, 1866–1878 (1961)
- [177] Ph. Lambin, A. A. Lucas, and J.-P. Vigneron, Polarization waves and van der Waals cohesion of C_{60} fullerite, *Phys. Rev. B* **46**, 1794–1803 (1992)
- [178] D. Östling, P. Apell, and A. Rosen, Theory for collective resonances of the C_{60} molecule, *Europhys. Lett.* **21**, 539–544 (1993)
- [179] S. Lo, A. V. Korol, and A. V. Solov'yov, Dynamical screening of an atom confined within a finite-width fullerene, *J. Phys. B: At. Mol. Opt. Phys.* **40**, 3973–3981 (2007)
- [180] A. V. Korol, and A. V. Solov'yov, Comment on 'Photoexcitation of a volume plasmon in C_{60} ions', *Phys. Rev. Lett.* **98**, 179601 (2007)
- [181] A. V. Verkhovtsev, A. V. Korol, and A.V. Solov'yov, Plasmon excitations in photo- and electron impact ionization of fullerenes, *J. Phys.: Conf. Ser.* **438**, 012011 (2013)
- [182] O. Baseggio, G. Fronzoni, and M. Stener, A new time dependent density functional algorithm for large systems and plasmons in metal clusters, *J. Chem. Phys.* **143**, 024106 (2015)
- [183] U. Fano, A common mechanism of collective phenomena, *Rev. Mod. Phys.* **64**, 313–319 (1992)
- [184] S. Malola, L. Lehtovaara, J. Enkovaara, and H. Häkkinen, Birth of the localized surface plasmon resonance in monolayer-protected gold nanoclusters, *ACS Nano* **7**, 10263–10270 (2013)

- [185] N. Durante, A. Fortunelli, M. Broyer, and M. Stener, Optical properties of Au nanoclusters from TD-DFT calculations, *J. Phys. Chem. C* **115**, 6277–6282 (2011)
- [186] R. Philip, P. Chantharasupawong, H. Qian, R. Jin, and J. Thomas, Evolution of nonlinear optical properties: from gold atomic clusters to plasmonic nanocrystals, *Nano Lett.* **12**, 4661–4667 (2012)
- [187] M. Stener, A. Nardelli, R. De Francesco, and G. Fronzoni, Optical excitations of gold nanoparticles: a quantum chemical scalar relativistic time dependent density functional study, *J. Phys. Chem. C* **111**, 11862–11871 (2007)
- [188] M. S. Dresselhaus, G. Dresselhaus, and A. Jorio, *Group Theory: Application to the Physics of Condensed Matter* (Springer, Berlin, 2010)
- [189] C. M. Aikens, S. Li, and G. C. Schatz, From discrete electronic states to plasmons: TDDFT optical absorption properties of Ag_n ($n = 10, 20, 35, 56, 84, 120$) tetrahedral clusters, *J. Phys. Chem. C* **112**, 11272–11279 (2008)
- [190] G. Mie, Beiträge zur Optik trüber Medien, speziell kolloidaler Metallösungen, *Ann. Phys.* **330**, 377–445 (1908)
- [191] E. M. Fernández, J. M. Soler, and L. C. Balbás, Planar and cage-like structures of gold clusters: density-functional pseudopotential calculations, *Phys. Rev. B* **73**, 235433 (2006)
- [192] C. Wälzlein, E. Scifoni, M. Krämer, and M. Durante, Simulations of dose enhancement for heavy atom nanoparticles irradiated by protons, *Phys. Med. Biol.* **59**, 1441–1458 (2014)
- [193] D. A. Varshalovich, A. N. Moskalev, and V. K. Khersonskii, *Quantum Theory of Angular Momentum* (World Scientific Publishing, Singapore, 1988)
- [194] L. G. Gerchikov, A. N. Ipatov, A. V. Solov'yov, and W. Greiner, Non-adiabatic electron-ion coupling in dynamical jellium model for metal clusters, *J. Phys. B: At. Mol. Opt. Phys.* **33**, 4905–4926 (2000)
- [195] E. Scifoni, E. Surdutovich, and A. V. Solov'yov, Spectra of secondary electrons generated in water by energetic ions, *Phys. Rev. E* **81**, 021903 (2010)
- [196] P. de Vera, R. Garcia-Molina, I. Abril, and A. V. Solov'yov, Semiempirical model for the ion impact ionization of complex biological media, *Phys. Rev. Lett.* **110**, 184104 (2013)

-
- [197] A. V. Korol and A. V. Solov'yov, *Polarization Bremsstrahlung*, Springer Series on Atomic, Optical, and Plasma Physics, Vol. 80 (Springer, Berlin Heidelberg, 2014)
- [198] H. K. Yuan, H. Chen, C. L. Tian, A. L. Kuang, and J. Z. Wang, Density functional calculations for structural, electronic, and magnetic properties of gadolinium-oxide clusters, *J. Chem. Phys.* **140**, 154308 (2014)
- [199] S. W. J. Scully, E. D. Emmons, M. F. Gharaibeh, *et al.*, Photoexcitation of a volume plasmon in C₆₀ ions, *Phys. Rev. Lett.* **94**, 065503 (2005)
- [200] M. Schüler, J. Berakdar, and Y. Pavlyukh, Disentangling multipole contributions to collective excitations in fullerenes, *Phys. Rev. A* **92**, 021403(R) (2015)
- [201] Y. Ling and C. Lifshitz, Plasmon excitation in polycyclic aromatic hydrocarbons studied by photoionization, *Chem. Phys. Lett.* **257**, 587–591 (1996)
- [202] A. V. Verkhovtsev, A. V. Korol, and A.V. Solov'yov, Quantum and classical phenomena in photoionization of carbon nanostructures, *J. Phys.: Conf. Ser.* **490**, 012159 (2014)
- [203] S. Biswas and L. C. Tribedi, Plasmon-mediated electron emission from the coronene molecule under fast ion impact, *Phys. Rev. A* **92**, 060701(R) (2015)
- [204] A. V. Verkhovtsev, R. G. Polozkov, V. K. Ivanov, A. V. Korol, and A. V. Solov'yov, Hybridization-related correction to the jellium model for fullerenes, *J. Phys. B: At. Mol. Opt. Phys.* **45**, 215101 (2012)
- [205] B.P. Kaffle, H. Katayanagi, M. Prodhan, H. Yagi, C. Huang, K. Mitsuke, Absolute total photoionization cross section of C₆₀ in the range of 25 – 120 eV: Revisited, *J. Phys. Soc. Jpn.* **77**, 014302 (2008)
- [206] E. E. Koch and A. Otto, Optical absorption of benzene vapour for photon energies from 6 eV to 35 eV, *Chem. Phys. Lett.* **12**, 476–480 (1972)
- [207] M. E. Rudd, Y.-K. Kim, D. H. Madison, and T. J. Gay, Electron production in proton collisions with atoms and molecules: energy distributions, *Rev. Mod. Phys.* **64**, 441–490 (1992)
- [208] E. Surdutovich, O. I. Obolensky, E. Scifoni, I. Pshenichnov, I. Mishustin, A. V. Solov'yov, and W. Greiner, Ion-induced electron production in tissue-like media and DNA damage mechanisms, *Eur. Phys. J. D* **51**, 63–71 (2007)

- [209] *Physics, Chemistry and Applications of Nanostructures*, edited by V. E. Borisenko, S. V. Gaponenko, V. S. Gurin, and C. H. Kam (World Scientific Publishing, Singapore, 2011)
- [210] C. Wälzlein, *Nanometer Scale Description of Electron Transport and Damage in Condensed Media Using the TRAX Monte Carlo Code*, Ph.D. thesis, Fachbereich Physik, Technische Universität Darmstadt, Germany (2014)
- [211] K. T. Butterworth, S. J. McMahon, F. J. Currell, and K. M. Prise, Physical basis and biological mechanisms of gold nanoparticle radiosensitization, *Nanoscale* **4**, 4830–4838 (2012)
- [212] C. Sicard-Roselli, E. Brun, M. Gilles, G. Baldacchino, C. Kelsey, H. McQuaid, C. Polin, N. Wardlow, and F. Currell, A new mechanism for hydroxyl radical production in irradiated nanoparticle solutions, *Small* **10**, 3338–3346 (2014)
- [213] B. D. Michael and P. O’Neill, A sting in the tail of electron tracks, *Science* **287**, 1603–1604 (2000)
- [214] *Radiation Damage in Biomolecular Systems*, edited by G. Garcia Gomez-Tejedor and M. C. Fuss (Springer Science+Business Media B.V., 2012)
- [215] I. Baccarelli, F. A. Gianturco, E. Scifoni, A. V. Solov’yov, and E. Surdutovich, Molecular level assessments of radiation biodamage, *Eur. Phys. J. D* **60**, 1–10 (2010)
- [216] X. Pan, P. Cloutier, D. Hunting, and L. Sanche, Dissociative electron attachment to DNA, *Phys. Rev. Lett.* **90**, 208102 (2003)
- [217] J. B. Foresman and Æ. Frisch, *Exploring Chemistry With Electronic Structure Methods: A Guide to Using Gaussian*, (Gaussian, Inc., Pittsburgh, 1996)
- [218] A. Szabo and N. S. Ostlund, *Modern Quantum Chemistry: Introduction to Advanced Electronic Structure Theory* (Dover Publications, Inc., Mineola, New York, 1996)
- [219] K. I. Ramachandran, G. Deepa, and K. Namboori, *Computational Chemistry and Molecular Modeling: Principles and Applications* (Springer-Verlag, Berlin-Heidelberg, 2008)

Biography (Lebenslauf)

Name	Alexey V. Verkhovtsev
Address	Frankfurt Institute for Advanced Studies Goethe-Universität Ruth-Moufang-Str. 1 60438 Frankfurt am Main, Germany
Tel. Nr.	+49 (069) 798 47524
E-mail	verkhovtsev@fias.uni-frankfurt.de
Date of Birth	22 October 1987
Place of Birth	St. Petersburg, Russia (formerly: Leningrad, USSR)

Education

2012–2016	PhD at the Department of Physics, Goethe-University, Frankfurt am Main, Germany
2008–2010	M. Sc. at Physical-Mechanical Department of St. Petersburg State Polytechnic University, St. Petersburg, Russia
2004–2008	B. Sc. at Physical-Mechanical Department of St. Petersburg State Polytechnic University, St. Petersburg, Russia

Degrees and Academic Qualifications

2010	Master of Science in Physics with honors, GPA: 4.86/5.0 St. Petersburg State Polytechnic University, St. Petersburg, Russia Thesis title: "Theoretical investigation of electronic structure of endohedral fullerenes", supervisor: Dr. Roman G. Polozkov
2008	Bachelor of Science in Physics with honors, St. Petersburg State Polytechnic University, St. Petersburg, Russia Project title: "Investigation of stability of hollow cluster systems within the jellium model", supervisor: Dr. Roman G. Polozkov
2004	School-leaving certificate with honors, St. Petersburg, Russia

Professional Career

- 2015–now Marie Curie early stage researcher, Instituto de Fisica Fundamental, Consejo Superior de Investigaciones Cientificas, Madrid, Spain
- 2013–now Junior research fellow, A.F. Ioffe Physical-Technical Institute of Russian Academy of Sciences, St. Petersburg, Russia

Awards and Scholarships

- Oct. 2011 DAAD Research Grant for Young Scientists, Frankfurt Institute for
– July 2012 Advanced Studies, Goethe-Universität, Frankfurt am Main, Germany
(Project supervisor: Prof. Dr. Andrey V. Solov'yov)

List of publications

Peer-reviewed journal articles

1. A. Verkhovtsev, E. Surdutovich, A. V. Solov'yov, *Multiscale approach predictions for biological outcomes in ion-beam cancer therapy*, Scientific Reports **6**, 27654-(1-10) (2016)
2. G. Sushko, A. Verkhovtsev, Ch. Kexel, A. V. Korol, S. Schramm, A. V. Solov'yov, *Reconciling simulated melting and ground-state properties of metals with a modified embedded-atom method potential*, Journal of Physics: Condensed Matter **28**, 145201-(1-6) (2016)
3. G. B. Sushko, I. A. Solov'yov, A. V. Verkhovtsev, S. N. Volkov, A. V. Solov'yov, *Studying chemical reactions in biological systems with MBN Explorer: implementation of molecular mechanics with dynamical topology*, The European Physical Journal D **70**, 12-(1-10) (2016)
4. A. V. Verkhovtsev, S. McKinnon, P. de Vera, E. Surdutovich, S. Guatelli, A. V. Korol, A. Rosenfeld, A. V. Solov'yov, *Comparative analysis of the secondary electron yield from carbon nanoparticles and pure water medium*, The European Physical Journal D **69**, 116-(1-9) (2015)
5. A. V. Verkhovtsev, A. V. Korol, A. V. Solov'yov, *Electron production by sensitizing gold nanoparticles irradiated by fast ions*, The Journal of Physical Chemistry C **119**, 11000–11013 (2015)
6. A. V. Verkhovtsev, A. V. Korol, A. V. Solov'yov, *Revealing the mechanism of the low-energy electron yield enhancement from sensitizing nanoparticles*, Physical Review Letters **114**, 063401-(1-6) (2015)
7. G. B. Sushko, A. V. Verkhovtsev, A. V. Solov'yov, *Validation of classical force fields for the description of thermo-mechanical properties of transition metal materials*, The Journal of Physical Chemistry A **118**, 8426–8436 (2014)

8. A. V. Verkhovtsev, S. Schramm, A. V. Solov'yov, *Molecular dynamics study of the stability of a carbon nanotube atop a catalytic nanoparticle*, The European Physical Journal D **68**, 246-(1-11) (2014)
9. G. B. Sushko, A. V. Verkhovtsev, A. V. Yakubovich, S. Schramm, A. V. Solov'yov, *Molecular dynamics simulation of self-diffusion processes in titanium in bulk material, on grain junctions and on surface*, The Journal of Physical Chemistry A **118**, 6685–6691 (2014)
10. A. V. Verkhovtsev, A. V. Korol, A. V. Solov'yov, *Quantum and classical features of the photoionization spectrum of C_{60}* , Physical Review A **88**, 043201-(1-8) (2013)
11. A. V. Verkhovtsev, A. V. Korol, A. V. Solov'yov, *Theoretical investigation of electron excitations in photoionization of nanoscale carbon-based systems*, St. Petersburg State Polytechnical University Journal: Physics and Mathematics **3(177)**, 80–91 (2013) (in Russian)
12. A. V. Verkhovtsev, G. B. Sushko, A. V. Yakubovich, A. V. Solov'yov, *Benchmarking of classical force fields by ab initio calculations of atomic clusters: Ti and Ni-Ti case*, Computational and Theoretical Chemistry **1021**, 101–108 (2013)
13. A. V. Verkhovtsev, M. Hanauske, A. V. Yakubovich, A. V. Solov'yov, *Characterization of small pure and Ni-doped titanium clusters: ab initio versus classical approaches*, Computational Materials Science **76**, 80–88 (2013)
14. A. V. Yakubovich, A. V. Verkhovtsev, M. Hanauske, A. V. Solov'yov, *Computer simulation of diffusion process at interfaces of nickel and titanium crystals*, Computational Materials Science **76**, 60–64 (2013)
15. A. V. Verkhovtsev, A. V. Yakubovich, G. B. Sushko, M. Hanauske, A. V. Solov'yov, *Molecular dynamics simulations of the nanoindentation process of titanium crystal*, Computational Materials Science **76**, 20–26 (2013)
16. P. Bolognesi, L. Avaldi, A. Ruocco, A. Verkhovtsev, A. V. Korol, A. V. Solov'yov, *Collective excitations in the electron energy loss spectra of C_{60}* , The European Physical Journal D **66**, 254-(1-9) (2012)
17. A. Verkhovtsev, A. V. Korol, A. V. Solov'yov, *Formalism of collective electron excitations in fullerenes*, The European Physical Journal D **66**, 253-(1-11) (2012)
18. A. V. Verkhovtsev, R. G. Polozkov, V. K. Ivanov, A. V. Korol, A. V. Solov'yov, *Hybridization-related correction to the jellium model for fullerenes*, Journal of Physics B: Atomic, Molecular and Optical Physics **45**, 215101-(1-8) (2012)

19. A. V. Verkhovtsev, A. V. Korol, A. V. Solov'yov, P. Bolognesi, A. Ruocco, L. Avaldi, *Interplay of the volume and surface plasmons in the electron energy loss spectra of C₆₀*, Journal of Physics B: Atomic, Molecular and Optical Physics **45**, 141002-(1-6) (2012) (Fast Track Communication)
20. A. V. Verkhovtsev, R. G. Polozkov, V. K. Ivanov, A. V. Korol, A. V. Solov'yov, *Investigation of electronic structure of noble gas endohedral fullerenes*, St. Petersburg State Polytechnical University Journal: Physics and Mathematics **1(116)**, 61–70 (2011) (in Russian)
21. A. V. Verkhovtsev, R. G. Polozkov, V. K. Ivanov, A. V. Solov'yov, *Stability of metallic hollow cluster systems*, Physica Scripta **80**, 048104-(1-4) (2009)
22. R. G. Polozkov, V. K. Ivanov, A. V. Verkhovtsev, A. V. Solov'yov, *Stability of metallic hollow cluster systems: Jellium model approach*, Physical Review A **79**, 063203-(1-7) (2009)
23. A. V. Verkhovtsev, V. K. Ivanov, V. S. Komarov, R. G. Polozkov, A. V. Solov'yov, *On stability of quantum cluster systems*, St. Petersburg State Polytechnical University Journal: Physics and Mathematics **6(67)**, 33–41 (2008) (in Russian)

Conference Proceedings

1. A. V. Verkhovtsev, A. V. Korol, A. V. Solov'yov, *Quantum and classical phenomena in photoionization of carbon nanostructures*, Journal of Physics: Conference Series **490**, 012159-(1-4) (2014) (Proceedings of the International Conference on Mathematical Modeling in Physical Sciences (IC-MSQUARE 2013), 01-05 September 2013, Prague, Czech Republic)
2. G. B. Sushko, A. V. Verkhovtsev, A. V. Yakubovich, A. V. Solov'yov, *Molecular dynamics simulation of nanoindentation of nickel-titanium crystal*, Journal of Physics: Conference Series **438**, 012021-(1-11) (2013) (Proceedings of the International Conference on Dynamics of Systems on the Nanoscale (DySoN 2012), 30 September - 04 October 2012, St. Petersburg, Russia)
3. A. V. Verkhovtsev, A. V. Korol, A. V. Solov'yov, *Plasmon excitations in photo- and electron impact ionization of fullerenes*, Journal of Physics: Conference Series **438**, 012011-(1-9) (2013) (Proceedings of the International Conference on Dynamics of Systems on the Nanoscale (DySoN 2012), 30 September - 04 October 2012, St. Petersburg, Russia)

4. R. G. Polozkov, V. K. Ivanov, A. V. Verkhovtsev, A. V. Korol, A. V. Solov'yov, *New applications of the jellium model for the study of atomic clusters*, Journal of Physics: Conference Series **438**, 012009-(1-11) (2013) (Proceedings of the International Conference on Dynamics of Systems on the Nanoscale (DySoN 2012), 30 September - 04 October 2012, St. Petersburg, Russia)
5. A. V. Verkhovtsev, R. G. Polozkov, V. K. Ivanov, A. V. Korol, A. V. Solov'yov, *Self-consistent Hartree-Fock approach to electronic structure of endohedral fullerene Ar@C₆₀*, Fullerenes, Nanotubes, Carbon Nanostructures **20**, 382–385 (2012) (Proceedings of the Joint International Conference "Advanced Carbon Nanostructures" (ACN 2011), 04-08 July 2011, St. Petersburg, Russia)
6. A. V. Verkhovtsev, R. G. Polozkov, V. K. Ivanov, A. V. Korol, A. V. Solov'yov, *Role of exchange interaction in self-consistent calculations of endohedral fullerenes*, Nuclear Instruments and Methods in Physics Research B **279**, 202–204 (2012) (Proceedings of the Fifth International Conference on Elementary Processes in Atomic Systems (CEPAS 2011), 21-25 June 2011, Belgrade, Serbia)